Geophysical Journal International

Data-oriented constraint on the interpretation of S receiver function and its application to observations of seismic discontinuities in the lithosphere-asthenosphere system

Journal:	*Geophysical Journal International*
Manuscript ID	GJI-19-0258.R1
Manuscript Type:	Research Paper
Date Submitted by the Author:	n/a
Complete List of Authors:	Shen, Xuzhang; Sun Yat-Sen University, School of Earth Sciences and Engineering Kim, YoungHee; Seoul National University, School of Earth and Environmental Sciences Song, Teh-Ru; University College London, Department of Earth Sciences Lim, Hobin; Seoul National University, School of Earth and Environmental Sciences
Keywords:	Body waves < SEISMOLOGY, Coda waves < SEISMOLOGY, Wave propagation < SEISMOLOGY, Wave scattering and diffraction < SEISMOLOGY, Structure of the Earth < GENERAL SUBJECTS

Geophysical International Journal

Data-oriented constraint on the interpretation of *S* receiver function and its application to observations of seismic discontinuities in the lithosphere-asthenosphere system

Xuzhang Shen[1], YoungHee Kim[2*], Teh-Ru Alex Song[3], and Hobin Lim[2]

1 Guangdong Provincial Key Laboratory of Geodynamics and Geohazards, School of Earth Sciences and Engineering, Sun Yat-Sen University, Guangzhou, 510275, China

2 School of Earth and Environmental Sciences, Seoul National University Seoul, 08826, Republic of Korea (younghkim@snu.ac.kr)

3 Seismological Laboratory, Department of Earth Sciences, University College London, WC1E 6BT, London, United Kingdom

Summary

This paper aims to improve the robustness of interpretation in the *S* receiver function (SRF), a technique commonly used to retrieve forward scattering of *S*-to-*P* converted waves (*Sdp*) originated from the lithosphere-asthenosphere system (LAS) beneath the stations. Although the SRF does not suffer interferences from backward scattering waves such as the first multiples from the Moho, one major drawback in the method is that *Sdp* phases can interfere with *P* coda waves and it is conceivable that these signal-generated noise may be misinterpreted as *Sdp* phase from the LAS beneath seismic stations. Through systematic analysis of full-waveform synthetics and SRFs from catalogued source parameters, we find that the strong *P* coda waves before the *S* wave in the longitudinal-component waveforms result in unwanted signal-generated noise before the *S* wave in the synthetic SRFs. If the mean amplitude of SRFs after the *S* wave is large, dubious signal-generated noise before the *S* arrival are strong as well. In this study, we honor the level of these unwanted signal-generated noise and devise data-oriented screening criteria to minimize the interference between *P* coda waves and genuine *S*-to-*P* converted waves. The first criterion is LQR, a direct measure of the amplitude ratio between longitudinal *P* coda waves and radial *S* wave in the waveform data. The second criterion is AMP, the amplitude of SRFs after the *S* arrival. We illustrate that these criteria effectively measure the energy level of mantle waves such as the *SP* wave. With synthetics and real data, we demonstrate the effectiveness of LQR and AMP criteria in minimizing these unwanted signal-generated noise in the stacked SRFs down to 1–2%, improving detection threshold and interpretation of *Sdp* phases from seismic discontinuities in the LAS.

Key words: Body waves; Structure of the Earth; Wave propagation, Wave scattering and diffraction; Coda waves

1 Introduction

Oceanic lithosphere is typically thought to be the outcome of melting of undepleted mantle and subsequent cooling, whereas continental lithosphere, especially beneath the cratons, is often considered as the result of large-scale plume melting, stacking oceanic lithospheres or/and arc collision (e.g. Lee *et al*. 2010). Small-scale convective instability, episodes of metasomatism and hydration, among other mechanisms, potentially facilitate the modification and disruption of oceanic and continental lithosphere. Unraveling robust seismic signature with the lithosphere-asthenosphere system (LAS) is crucial to understanding of the formation, modification and destruction of the plates and the formation of continents. For instance, the lithosphere-asthenosphere boundary (LAB), a mechanical boundary separating the rigid lithosphere and underlying viscous asthenosphere is thought to be the result of a simple thermal boundary due to long-term cooling. Seismic LAB from such a thermal boundary is considered smooth and gradual, where the velocity reduction with depth takes place over a transition thickness on the order of 50 km (Fischer *et al*. 2010). However, recent efforts have demonstrated that seismic LAB can be much sharper (e.g. Rychert *et al*. 2007; Kawakatsu *et al*. 2009; Tharimena *et al*. 2017). Beneath the continents and many localities in the oceans, seismic discontinuities have also been observed at depth ranges much shallower than expected, and the nature of such mid-lithospheric discontinuities (MLDs) remains elusive (e.g. Karato 2012; Schmerr 2012; Selway *et al*. 2015).

Therefore, it is clear that a robust and high-resolution seismic detection and characterization of LAB or/and MLDs can revolutionize our understandings of plate tectonics (e.g. Eaton *et al*. 2009; Fischer *et al*. 2010; Kawakatsu & Utada 2017). In the last decade, the depth and spatial resolution of the seismic discontinuities are greatly improved, thanks to the explosion of seismic data and progression of varieties of seismic techniques, including teleseismic *P*-to-*S* receiver function (PRF) (e.g. Langston 1977; Rondenay 2009) and *S*-to-*P*

receiver function (SRF) (e.g. Farra & Vinnik 2000), *ScS* reverberations (e.g. Bagley & Revenaugh 2008), and multiple *S*-wave triplications (e.g. Tan & Helmberger 2007) and underside *SS* precursors (e.g. Rychert & Shearer 2011; Schmerr 2012). Among these methods, PRF and SRF provide the highest resolution of seismic discontinuities in the LAS because of the use of relatively high-frequency waves (e.g. 0.1–1.0 Hz) in the analysis.

While the PRF and SRF methods can effectively detect converted phases (*Pds* or *Sdp,* where '*d*' marks the depth or location of the conversion) through source normalization (or deconvolution) and stacking, they are not without issues. For example, the PRF suffers interferences from backward scattering waves such as the first multiples from the Moho, making it difficult to identify converted-phase arrivals within the LAS. On the other hand, the SRF, by construction, separates the converted phases from the multiples (e.g. Ferra & Vinnik 2000), and it is preferable to identify robust signal from the LAS. However, one major drawback is that *Sdp* converted waves can be interfered by *P* coda waves, which consist of multiple mantle *P* waves (e.g. Wilson *et al*. 2006), multiples of reflections between the surface and the transition zone (e.g. Bock 1994) or/and *S*-to-*P* scattering waves within the crust and lithosphere between the source and the receiver (e.g. Vinnik & Romanowicz 1991). Depending on the strength of scatters as well as epicentral distance, azimuth, earthquake source depth, and source mechanisms, the amplitudes and timings of these *P* coda waves may vary and a significant level of wave energy preceding the *S*-wave arrival can be erroneously taken as *S*-to-*P* phases converted beneath the stations. Therefore, a robust identification and interpretation of *S*-to-*P* converted waves in the SRF are not necessarily trivial, and data selection criteria can become the key to provide a more robust determination of sharp features in the LAS.

The purpose of this paper is thus to introduce simple but effective screening criteria for the data selection and therefore removal of data or SRFs with strong unwanted signal-

generated noise. We will first briefly review data selection criteria established in the literatures (e.g. Kumar *et al*. 2005; Yuan *et al*. 2006; Wilson *et al*. 2006; Abt *et al*. 2010; Kind *et al*. 2015; Shen *et al*. 2017). To devise an objective criterion to minimize the interference from *P* coda waves, as a proof of concept, we first examine scenario of SRFs recorded in South Korea seismic network, sitting on a geologically stable continental platform (Fig. 1). Through systematic analysis of full-waveform synthetics and SRFs from catalogued teleseismic earthquakes in 2005–2015 (Takeuchi *et al*. 1996; Kawai *et al*. 2006), we demonstrate the usage and effectiveness of the new data screening and selection criteria against previous efforts (e.g. Wilson *et al*. 2006) with synthetics as well as observed SRFs in South Korea.

2 Construction of SRF and previous efforts in the data selection criteria

The calculation of SRF involves two important steps, that are (1) coordinate rotation, which isolates *Sdp* phase from the incident *S* wave, and (2) deconvolution, which removes source and propagation path effects (e.g. Farra & Vinnik 2000). Three-component north-east-vertical (N–E–Z) data are rotated to L–Q–T (or *P–SV–SH*) ray coordinate system (see also Rondenay 2009). While both of these coordinate systems are frequently implemented in past SRF studies (see review by Rondenay 2009; Kind *et al*. 2012), as demonstrated by Svenningsen *&* Jacobsen (2004) and discussed by Rondenay (2009), the difference of SRFs constructed in these two coordinate systems is minimum and much less than 1% (see Fig. 3 in Svenningsen *&* Jacobsen (2004)). Since the aim of this paper is to design the metrics to indicate the level of unwanted signal-generated noise prior to the *S* wave, we choose to discuss and illustrate the usage of our designed metrics in the L–Q–T system throughout this paper.

As the L component is dominated by the *P* wave, Q and T components mostly contain energies from *SV* and *SH* waves, respectively. SRFs are then computed by deconvolving the *S* waveform in the Q component from the corresponding L component, in either time domain or frequency domain. To improve the signal-to-noise ratio (SNR), SRFs are binned and stacked. Throughout the paper, we will illustrate the usage and performance of our data-oriented screening criteria with the time-domain Wiener deconvolution method (Robinson & Treitel 1967), whereas examples with the frequency-domain deconvolution of various water levels can be referred to the Supplementary Information.

Earlier works put emphasis on the selection of earthquakes in restricted epicentral distances or/and source depths (e.g. Wilson *et al*. 2006; Yuan *et al*. 2006). In an attempt to evaluate the robustness of the observed *Sdp* phases, Yuan *et al*. (2006) performed full waveform synthetics (Wang 1999) and suggested optimal epicentral distances of 55°−85° for the construction of SRF, which avoid post-critical incoming *S* wave. However, the synthetic waveforms only include downgoing waves and upgoing waves were excluded. Consequently, the influence of surface-reflected *P* waves on the *Sdp* detection cannot be evaluated. On the other hand, Wilson *et al*. (2006) conducted full waveform synthetics (Fuchs & Müeller 1971) and quantitatively measured the energy level before the *S* wave in the SRFs. They suggested a data selection criterion for the SRF at restricted epicentral distances of 60°–75° and source depths of 300 km or less.

The criterion by Wilson *et al*. (2006) was however based on synthetics from a single thrust-fault source mechanism and an one-dimensional (1-D) velocity model with a relatively thick crust of 70 km. Therefore, the established criterion needs not necessarily be the most general choice. As *P* coda waves can consist of multiple mantle *P* waves or/and *S*-to-*P* scattering waves within the crust and lithosphere between the source and the receiver, the amplitude and timing of these *P* coda waves not only depend on source depth (Wilson *et al*.

2006), but it may also depend on the strength of scatters and source-receiver geometry and source mechanisms, or effectively the radiation pattern. Nevertheless, these data selection criteria have been commonly used in the SRF analysis, sometimes with a minor adjustment on either the range of epicentral distance or/and source depth (e.g. Hansen *et al*. 2009; Abt *et al*. 2010; Ford *et al*. 2010; Lekic & Fischer 2014; Hopper & Fischer 2015).

To improve the robustness and interpretation of the SRF and establish a more general data selection scheme, our focus is to expand the work by Wilson *et al*. (2006) and establish data-oriented selection criteria. In particular, by either contrasting the energy level between the *S*-wave arrival in the Q-component waveform and *P* coda waves in the L-component waveform, or measuring the amplitude of the SRF after the *S* wave, we introduce more direct and general selection and screening criteria that do not necessarily rely on a specific choice of the epicentral distance or source parameters, but honor the level of unwanted signal-generated noise before the *S* wave.

3 Design and construction of new data selection criteria for the SRF

As discussed in previous sections, multiple mantle *P* waves or *S*-to-*P* scattering within the crust and mantle between the source and receiver (Vinnik & Romonowicz 1991; Bock 1994; Wilson *et al*. 2006) can form the *P* coda waves. Depending on the amplitude of these *P* coda waves preceding the *S*-wave arrival, they can interfere with converted waves, *Sdp*, from the LAS beneath seismic stations, or even being erroneously identified as *Sdp*. Depending upon the epicentral distance, source depth and mechanism, the level of interference can vary. In other words, the energy level of *P* coda waves can be large even for a shallow event. Since the effect of diverse source mechanism or radiation pattern on the excitation of these *P* coda waves was not explored by Wilson *et al*. (2006), we conduct a systematic investigation

through full waveform synthetics and examine the impact of realistic source mechanisms, or more importantly, the radiation pattern on the excitation and amplitude of *P* coda waves.

As a proof of concept, we consider observations of one station from the South Korea seismic network (Lim *et al.* 2018) and examine full waveform synthetics from earthquakes with magnitude larger than 5.5 between 2004 and 2013 from the global CMT catalogue (Dziewonski *et al.* 1981; Ekström *et al.* 2012), located at the distances of 60°–85° from the seismic network (Fig. 1). The event magnitude threshold of 5.5 allows detection of clear *S*-wave arrivals and identification of *SMp* arrivals from the Moho beneath the continental platform in South Korea. Since most stations generally contain quality waveform data from 200–400 earthquakes after data quality control and screening, we randomly select 300 earthquakes in our synthetic test. As expected in most realistic scenarios, synthetics data are predominantly from shallow events. Synthetic waveforms are computed with the Direct Solution Method (Takeuchi *et al*. 1996; Kawai *et al*. 2006) using the 1-D IASP91 model (Kennett & Engdahl 1991) as well as a modified IASP91 model (denoted as 'L70'), which includes a 35 km thick high-velocity mantle lid with a 7.5% shear velocity increase below Moho, a low velocity zone with a 9% shear velocity reduction beneath 70 km depth, and a small 1.5% shear velocity increase beneath 120 km depth (Fig. S1; Table S1).

To calculate synthetic SRFs, we first rotate synthetic waveforms with a time window of 100 s prior to and 100 s after the *S* wave to the radial-tangential-vertical (R–T–Z) system using the theoretical event back-azimuth. Theoretical incidence angle of the *S* wave computed from the IASP91 model is used to rotate waveforms into the ray coordinate system in the L–Q–T components (e.g. Rondenay 2009) before deconvolution (e.g. Kind *et al.* 2012; Shen *et al*. 2017). The waveforms in the Q component (e.g. the parent waveform) are windowed 10 s before and 35 s after the *S*-wave arrival and tapered with a 15% Hanning

taper at both ends of the signal window. The L- and Q-component waveforms are then deconvolved by the parent waveform through the time-domain Wiener deconvolution method, which involves spiking of the output time series with the parent waveform and construction of Wiener-filter time series (Robinson & Treitel 1967). Minimum regularization with a white noise of 0.01% is applied in the calculation. Such a time series is then convolved with L- and Q-component waveforms to obtain L- and Q-component SRFs, respectively. The resulting SRFs are bandpass filtered at 3–50 s and normalized by the spike in the Q-component at zero time. Hereafter, we will refer our discussion in the L-component SRFs.

3.1 Inspections of synthetic SRFs

Figs 2a and b display stacked synthetic SRF record sections, which consist of 300 individual SRFs, stacked with a 1°-distance bin and aligned along the *S* arrival at zero time. Synthetics are computed with the IASP91 model (Fig. 2a) and the L70 model (Fig. 2b). The converted waves from the Conrad (*SCp*) and the Moho (*SMp*) have a negative polarity and they arrive at about 4–5 s before the *S* wave (Fig. 2). Crustal multiples (e.g. *SCpPCP* and *SMpPMP*) and other mantle waves such as *SP*, *sSP, pSPPP, sSPPPP* and *pSPPPPP* arrive at about 5–60 s after the *S* wave (Fig. 2). Converted waves at the upper mantle seismic discontinuities from incident *ScS* and *SKS* waves (e.g. *ScS410p*, *ScS660p*, *SKS410p* and *SKS660p*) have a very different moveout from the *SMp* and they are less visible than those shown in Yuan *et al*. (2006). On the other hand, as pointed out by Wilson *et al*. (2006), we can observe spurious but consistent energies before the *SMp* arrival that are not associated with converted waves from local structure beneath the receivers. Therefore, it is important to set up a general data selection scheme to minimize these spurious arrivals.

After systematically inspecting synthetic waveforms and the resulting SRFs, we use Fig. 3 to illustrate the motivation of our designated data selection criteria. We consider two

earthquakes (events 1 and 2) such that their epicentral distances are comparable at ~67° and the SNR of the *S* waves in the Q component are also similar (Fig. 1a, red beachballs). However, regardless of the choice of IASP91 model or L70 model (Fig. S1), the *P* coda waves in the L-component waveforms are comparably stronger in event 2 than those in event 1, arguing the effect of radiation pattern on the amplitude of these *P* coda waves. When examining their SRFs, those from event 1 display clear *SMp* or/and *SLp* with otherwise weak energy prior to the *S* wave (Figs 3a and b). On the other hand, SRFs from event 2 display strong and spurious energy before and after the *S* wave (e.g. Figs 3c and d). It is noteworthy to emphasize that, as the deconvolution scheme, data windowing and tapering procedures are exactly the same between event 1 and event 2, strong spurious energy before the *S* wave in the SRF directly corroborates with strong *P* coda waves in the L-component waveform of event 2 (see also Figs S2 and S3 for the results with different windowing schemes). As noted earlier, it is conceivable that these dubious signals may be mistakenly interpreted as *Sdp* waves beneath seismic stations.

3.2 Measurement of LQR and AMP and construction of stacked SRFs

Motivated by observation, we devise measures of LQR, the amplitude ratio between L-component *P* coda waves and Q-component *S* waves, and AMP, the amplitude of SRFs after the *S*-wave arrival. We then systematically test how the LQR and AMP thresholds may be used to detect and retain robust *Sdp* waves while minimizing dubious energies in the SRFs (Fig. 3). Here, we define LQR as

$$\mathrm{LQR} = \mathrm{RMS}(\mathrm{L}[t_3\ t_4]) \,/\, \mathrm{Max}(\mathrm{Q}[t_1\ t_2]), \qquad (1)$$

where Max(Q[t_1 t_2]) measures the peak amplitude of the *S* wave in the Q-component data window defined by t_1 and t_2, and RMS(L[t_3 t_4]) measures the RMS amplitude of the *P* coda in the L-component time window defined by t_3 and t_4. On the other hand, the AMP is defined as

$$\mathrm{AMP} = \mathrm{RMS}(\mathrm{SRF}[t_5\ t_6]), \qquad (2)$$

where RMS(SRF[t_5 t_6]) measures the RMS amplitude of the SRF in the time window defined by t_5 and t_6 with respect to the *S* arrival. In the subsequent analysis and demonstration, we set t_1 = -5 s, t_2 = 10 s, t_3 = -60 s, t_4 = -20 s, t_5 = 20 s, and t_6 = 100 s. Note that the choice of t_3 and t_4 is such that they do not include potential *Sdp* arrivals in the LAS.

After measuring the LQR and AMP against all synthetic SRFs, we observe that SRFs with the lowest LQR typically fall in the distance range of 60°–66° and those with the lowest AMP are typically in the distance range of 70°–77°. However, to fully take advantage of the slant stack technique, it is important to ensure effective noise removal and to minimise data selection bias in epicentral distance. Therefore, it is more desirable that selected SRFs are evenly distributed within the entire distance range of 60°–85° and are not falling in a narrow distance range. Consequently, synthetic SRFs in each 1°-distance bin are first selected according to a designated data selection threshold and subsequently stacked. The error is then estimated by the bootstrap method (Efron & Tibshiran 1998).

In the following tests, we systematically examine how different LQR and AMP thresholds determine the quality of the stacked SRFs. To determine the effectiveness of each data selection criteria in mitigating signal-generated noise, we sum stacked SRFs of each 1°-distance bin and measure the RMS amplitude of the summed SRF before the *SMp* arrival (denoted as AMP1). The AMP1 is defined as

$$\mathrm{AMP1} = \mathrm{RMS}(\mathrm{SRF}[t_7\ t_8]), \qquad (3)$$

where RMS(SRF[t_7 t_8]) measures the RMS amplitude of the SRF in the time window defined by t_7 and t_8 with respect to the *S* arrival. Here, we set t_7 = -60 s and t_8 = -20 s.

3.3 Evaluating the efficacy of the LQR and AMP criteria

In order to investigate the efficacy of LQR and AMP criteria for the SRFs, we consider two principles to judge the quality of stacked SRFs. First, if the data selection criterion is effective, we expect that the signal-generated noise before the *S* arrival shall be minimized. This can be visually inspected and quantitatively examined through the measurement of AMP1. Second, if the data selection criterion is effective, the amplitude of stacked SRFs against epicentral distance should follow closely the theoretical *S*-to-*P* transmission coefficient (Aki & Richards 2002) with minimum perturbation.

3.3.1 Presence/absence of signal-generated noise before *S*-wave arrival

To highlight how the data selection criteria influence signal-generated noise, synthetic SRFs with 25% lowest and 25% highest LQR (or AMP) in each distance bin are selected and subsequently stacked. For comparison, we also present stacked SRFs with the criterion by Wilson *et al*. (2006) and those with 25% randomly selected SRFs. Stacked SRF images at 60°–85° from the IASP91 model (Kennett & Engdahl 1991) and L70 model (Fig. S1) are shown in Fig. 4, whereas the sum of stacked SRFs and their 95% confidence interval are displayed in Figs 5a and 5b, respectively. For comparisons, stacked SRF waveforms (Figs 5c–f) and stacked SRF images (Figs S4–7) with different parent window length (case 1; -10 s before and 15 s after the *S* wave), tapering (case 2; 5% Hanning taper), deconvolution scheme and regularization (cases 3 and 4; frequency-domain deconvolution with water level of 0.05% and 0.2%, respectively) are also presented for comparisons.

For the IASP91 model, the first signal before the *S* arrival is a negative *SMp* phase arriving at about 4 s before the *S* arrival (Figs 4a–f and 5a). While the *SMp* signal can be consistently detected with different data selection criteria (Figs 4a–f and 5a), the amplitudes of *SMp* with the highest LQR and AMP criteria are much stronger and more variable than those with the lowest LQR or AMP criteria (Fig. 5a). In particular, signals up to 6–8% with positive amplitude can be detected before the *SMp* at the 95% confidence level (Fig. 5a). However, these signals are dubious as they do not corroborate with the absence of any sharp velocity gradient below the Moho (Fig. S1). While the criterion by Wilson *et al*. (2006) does a better job in reducing the amplitude of these dubious signals down to 3–4% (Fig. 5a), the lowest LQR and AMP criteria appear to be the most effective, minimizing dubious arrivals at the amplitude level of 1–2%, typically insignificant at the 95% confidence level (Fig. 5a).

For the L70 model, we can observe a consistent, but positive signal arriving at about 9 s before the *S* arrival (Figs 4g–l and 5b). As expected, it is the *S*-to-*P* converted arrival (*SLp*) from the negative velocity discontinuity at the depth of 70 km (Fig. S1), Such a *SLp* signal has the same polarity and comparable strength as those used in previous studies to infer LAB or MLDs in the LAS (e.g., Eaton et al., 2009; Abt et al., 2010; Kumar et al., 2012; Shen et al., 2015; Shen et al., 2017). However, except the lowest LQR or AMP criteria, all other data selection criteria produce strong oscillations throughout the entire SRF stacks (Figs 4g–l), following slowness very similar to the *SP* wave. Even the *SLp* appears to be detected in this circumstance, the quality of the detection is low with incorrect amplitude and very large uncertainties (Fig. 5b). With the lowest LQR or AMP criteria, the *SLp* signal appears more robust with the smallest bootstrap uncertainties (Fig. 5b). It is evident that the signal-generated noise before the *S* arrival are much weaker in the stacked SRFs produced with the criteria of the lowest LQR (Figs 4g and 5b) or AMP (Figs 4i and 5b) than those produced

with the highest LQR (Figs 4h and 5b), the highest AMP (Figs 4j and 5b), the criterion by Wilson *et al.* (2006) (Figs 4k and 5b) or with random data selection (Figs 4l and 5b).

These observations can be concluded with alternative window length of the parent waveform (case 1; Figs 5c and S4), tapering (case 2; Figs 5d and S5) or deconvolution scheme (e.g. frequency-domain water-level deconvolution) with different regularization (cases 3 and 4; Figs. 5e, 5f, S6, and S7). Stacked SRFs produced with the criteria of the lowest LQR or AMP are stable, regardless specific choices of these data processing procedures. Evidently, stacked SRFs with other criteria vary more substantially with the choice of data processing routines. More critically, while a stronger regularization does minimize amplitude oscillation (e.g. case 4; Fig. 5f), strong signal-generated noise arriving before the *SLp* arrival remains.

To quantitatively assess the quality of stacked SRF and the effectiveness of data selection criteria in mitigating the signal-generated noise, we compute AMP1 to measure the RMS amplitude in the designated time window before the *S* arrival. We systematically select a subset of all synthetic SRFs by varying the percentage threshold (10–50%) of the lowest and highest LQR or AMP, generate the summed SRF and calculate AMP1. As shown in Fig. 6, the value of AMP1 generally decreases with increasing percentage threshold of six different criteria. At 25% threshold, AMP1 of the lowest LQR or AMP is lower than that of the highest LQR or AMP by more than a factor of 4 (Fig. 6). Also, at 25% threshold and higher, AMP1 of the lowest LQR or AMP is less than AMP1 of all SRFs (Fig. 6a). In particular, we find that the SRFs constructed with the lowest AMP generally display a lower level of AMP1, and the improvement is even more substantial for the synthetic SRFs from the L70 model (Fig. 6b). AMP1 of the lowest AMP for the L70 model is lower by a factor of 2 or less than that measured against the summed SRF of the entire SRF dataset (Fig. 6b).

In the case of random data selection, the value of AMP1 does not show appreciable difference with respect to the percentage threshold (Fig. 6), whereas the criterion of Wilson *et al*. (2006) does not seem to improve AMP1 upon those from random data selection (Fig. 6), which is not unexpected as synthetic data are predominantly from shallow events. In a way, even with a smaller volume of the entire synthetic SRFs (e.g., 25% or less), the lowest LQR or AMP criterion achieves a much lower AMP1 than that of Wilson *et al*. (2006)'s using 50% of the entire synthetic SRFs. Notably, depending on the exact data selection threshold, AMP1 with lowest LQR or lowest AMP criteria can be 20–50% lower than AMP1 of all events (Fig. 6).

3.3.2 Validating the amplitude of the *S*-to-*P* converted waves

To further verify the robustness of the converted phases beneath the receiver and assess the stability of the signal, we measure the amplitudes of *Sdp* (e.g. *SMp* and *SLp*) and compare them against the theoretical *S*-to-*P* transmission coefficient (Aki & Richards 2002). If the amplitudes of *Sdp* from the stacked SRFs follow closely to the theoretical transmission coefficients, we consider that the data selection criteria are effective in removing signal-generated noise and recovering a truthful detection. Fig. 7a shows distance-dependent amplitudes of *SMp* measured against stacked SRFs of six different criteria for the IASP91 model. On the other hand, Figs 7c and 7d show distance-dependent amplitudes of *SMp* and *SLp* measured against stacked SRFs of different criteria for the L70 model, respectively. Fig. 7b shows the amplitudes of the SRFs measured in the same time window as that used in Fig. 7d for comparison. Since we do not expect a truthful detection of *SLp* for the IASP91 model, the measurements are indicative of the level of signal-generated noise.

Typically, the highest LQR or AMP criterion results in unstable estimate of *SMp* amplitudes (e.g. Figs 4 and 5), and their amplitudes strongly deviate from the theoretical

predictions (Figs 7a and c). Stacked SRFs from the random data selection or from the criterion of Wilson *et al*. (2006) also suffer similar distortion, but to a less degree (Fig. 7). On the other hand, given the selection criteria of 25% lowest LQR or AMP, the amplitude of *SMp* follows closely to theoretical calculation against distance (Figs 7a and c). Similarly, the amplitude of *SLp* against distance generally follows theoretical prediction when the data selection criteria of 25% lowest LQR or AMP are implemented (Fig. 7d). Our results indicate that the lowest LQR or AMP is useful for detecting *SLp* phases and retaining their amplitudes by reducing the dubious signals before the *S* wave. We note that the average amplitude within the time window for expected *SLp* arrivals is typically on the order of 2% for the lowest LQR, and of ~1% for the lowest AMP (Fig. 7b). Therefore, we suggest 2% as the minimum amplitude threshold above which the robust identification of local *Sdp* converted waves within the LAS can be made and interpreted.

In summary, we find that the SRFs constructed with the lowest LQR or AMP generally display a lower level of spurious energy before the *S* wave while the SRFs with the highest LQR or AMP, as expected, displays a higher level of signal generated noise (Figs 4–7). The improvement appears more substantial in the case where synthetic SRFs are computed from the L70 model (Fig. 6b). While the calculation of SRF can be influenced by the choice of time window and tapering in the parent waveform as well as the deconvolution scheme (e.g. Lekic & Fischer 2017), the performance of LQR and AMP data selection criteria does not depend on such specific choices. This characteristic makes the LQR and AMP very desirable since stacked SRFs with low LQR and low AMP are always very stable.

3.3.3 The sources of *P* coda waves?

To investigate the source of these *P* coda waves, we first examine if the attributes such as LQR or AMP depend on epicentral distance, event back azimuth or source

parameters. However, we do not observe any obvious selection bias in event epicentral distance or back azimuth against the criteria such as LQR and AMP (Fig. S8), nor do we find dependence of LQR or AMP on earthquake source mechanism (Fig. S9), suggesting that LQR and AMP, or the level of *P* coda waves, are predominantly dictated by the radiation pattern. In this regard, while we do not specifically include *SV/SH* amplitude ratio in the data selection criteria, high LQR or AMP criterion more often corresponds to data with a low *SV/SH* ratio (< 1) and low LQR or AMP typically corresponds to data with a high *SV/SH* ratio (> 1) (Fig. 8).

It has been argued by Wilson *et al*. (2006) that *P*-coda waves can come from multiples such as *pPPP*, *pPPPP* or/and *sPPPP* from deep events (> 300 km) and they may interfere with *Sdp* phases. However, for most practical analysis on the LAS, only those from really deep events of 450 km or deeper may directly interfere with *Sdp* from the LAS since these multiples, in most instances, arrive at least 1–2 minutes before the *S* arrival. Similar lines of arguments have been also pointed out by Vinnik & Romanowicz (1991). This assertion can be supported by the fact that *P* radiation patterns computed with the slowness such as *pPPPP* wave do not distinguish against LQR or AMP (Fig. 9). This is also consistent with our observation that, when shallow events dominate the synthetic dataset, Wilson *et al*. (2006)'s criterion does not necessarily outperform data selection scheme of random choice (Figs 5b–f; see also Figs S4–7).

As shown in Figs 4g–l, signal-generated noise before the *S* arrival appear to follow very similar slowness as those mantle waves such as *SP*, *sSP*, *sSPPP,* and *sSPPPP*, apparently forming precursors of these mantle waves and interfering with *Sdp* phases in the LAS. It is conceivable that energies prior to the *S* wave in the stacked SRF are likely to be scattering waves such as *S•P* and *SP•P*, where *S•P* denotes *S*-to-*P* scattering wave from the free surface

and *SP•P* denotes *SP*-to-*P* scattering wave from the scatter in the crust (Vinnik 1981; Vinnik & Romanowicz 1991). Depending on the lead time of scattering waves with respect to the *S* wave, the area of scattering is expected to be at least 25° from the receiver, and typically in the range of 30°–40° from the receiver (see Fig. 8a of Vinnik & Romanowicz (1991)), with the raypaths of *S* and *P* waves in the *S•P* (or *SP•P*) arriving in different vertical planes. As our wave propagation simulation is done with a laterally homogeneous and spherically symmetric earth model (Kawai *et al*. 2006) with a finite duration *S* wave, spherical waves propagating off the vertical plane defined by the source and receiver likely result in scattering waves such as *S•P*.

If *S•P* or/and *SP•P* scattering waves are indeed the cause of these signal-generated noise observed in SRFs, the *SV* radiation pattern in the area of scattering will directly control the amplitude of *S•P* and *SP•P* scattering waves (Vinnik & Romanowicz 1991). To validate this, we assume that the scattering area is near the surface reflection point of *SP* wave and compute *SV* radiation pattern with the slowness of *SP* wave in our synthetic dataset. As shown in Fig. 10, the *SV* radiation patterns against the lowest LQR and AMP criteria are generally much weaker than those against the highest LQR and AMP criteria. Effectively, LQR and AMP criteria help select data with weakest *SV* radiation pattern in the scattering area. Following the same line of reasoning, it is conceivable that *S•P* scattering waves can come from internal boundaries such as the Moho. While a more elaborated investigation should be done in the future, this is consistent with our simulation that signal-generated noise in SRF are much stronger in the L70 model, which includes a larger velocity contrast across the Moho than the IASP91 model as well as an additional velocity reduction at 70 km depth (Fig. S1).

Evidently, there is no lateral variation in surface topography, internal boundary or velocity in our simulation, and it is difficult to precisely estimate the scattering potential without invoking 2-D or 3-D full waveform modelling. It is also possible that signal-generated noise in 2-D or 3-D models are less coherent and do not add constructively. However, our data-oriented screening criteria such as LQR or AMP are designed to honor the data and provide direct and straightforward attributes to measure the level of these spurious energies. With lowest LQR or/and AMP, SRFs with strong signal-generated noise are effectively removed, improving the quality of stacked SRF and the detection of true *Sdp* arrivals in the LAS beneath seismic stations.

4 Application to South Korea seismic data: detection and characterization of seismic discontinuities in the LAS

Our synthetic tests have demonstrated that the effectiveness of LQR and AMP could serve as general data selection criteria for the construction of SRF. Here we apply these new data selection criteria to the dataset recorded by South Korea seismic network (Fig. 1) (Lim *et al*. 2018) and illustrate its effectiveness in real datasets. We select earthquake magnitudes greater than 5.5 within the epicentral distance range of 60°–85° from the seismic network. To construct the SRF, we follow exactly the same scheme detailed in the synthetic test in Section 3, but highlight a few key additional steps here to screen noisy data. First, when rotating three-component waveforms into L-Q-T coordinate system, the incidence angle of the incoming *S* wave is determined by maximizing the *SV*-wave energy on the Q component within the time window spanning ±2 s on either side of the theoretical *S*-wave onset. If the difference between the observed incidence angle and the predicted one (from IASP91) exceeds 25°, the waveforms are rejected. Secondly, data are also removed if the SNR of the *S*

wave in the Q component is less than 5. Thirdly, if the peak SRF amplitude in the L component is larger than 0.5 or if the mean amplitude of the SRF in the L component is larger than 50% of its peak amplitude, such SRFs are apparently oscillatory throughout the entire time window and they are also rejected.

As an example, we examine stacked SRFs at station TJN in South Korea seismic network (Fig. 1b) in detail. We process waveform data from 917 events in January 2005–January 2015 (Lim *et al*. 2018) and, after preliminary data quality control detailed earlier, 316 SRFs are retained and they are filtered at 3–50 s before subsequent data selection analysis. Here we measure LQR and AMP against the observed SRFs exactly the same way as discussed in Section 3. In general, the lowest LQR and AMP against the observed SRFs are typically higher than that against synthetics SRFs because of noise. With the nominal percentage threshold of 25%, we finally retain about 80 SRFs.

To illustrate how the stability of the SRF and detection of *SMp* and *SLp* depend on the data selection criteria, Fig. 11 (and Fig. S10) displays stacked SRF images constructed with the same six different data-selection criteria as discussed in the synthetic test in Section 3 (e.g. Fig. 4), With the lowest LQR or AMP criterion (Figs 11a and c), we can reasonably track a consistent signal with negative amplitude with respect to epicentral distance, arriving about 4 s before the *S* arrival, presumably *Sdp* from the Moho (*SMp*). However, it is less trivial to track *SMp* in stacked SRF image with the Wilson *et al*. (2006)'s criterion (Fig. 11e) or random selection criterion (Fig. 11f), and very difficult to do so against those constructed with the highest LQR or AMP criterion (Figs 11b and d). These observations can also be made against stacked SRF images using a stronger regularization of 1% white noise (Figs S13 and S14).

Stacking the SRFs shown in Fig. 11, Figs 12a and b displays summed SRF waveforms and their bootstrapped uncertainties against the six different data-selection criteria and data selection threshold of 25% and 50%, respectively. Again, using the lowest LQR, AMP or Wilson *et al*. (2006)'s criterion, detection of *SMp* can be made at the 95% confidence level (Fig. 12). With the highest LQR or AMP criterion, the *SMp* can be barely detected at the 95% confidence level with large uncertainties (Fig. 12a and b). Even with a stronger regularisation (1% white noise), *SMp* still possesses large uncertainties (Fig. 12c). It is important to note that the uncertainties of SRF with low LQR and AMP are much smaller than those with high LQR or AMP or random selection (Fig. 12). In principle, a consistent detection of *SMp* with small amplitude uncertainties serves as a very good indication on the quality of stacked SRF. Furthermore, with the lowest LQR or AMP criterion, a positive signal arriving at about 8 s before the *S* arrival, possibly *SLp* from the LAS, can be detected at 95% confidence level (Fig. 12), whereas such a *SLp* arrival cannot be detected otherwise with statistical significance (Fig. 12). We note that the amplitude of detected *SLp* is about 5–7%, considerably exceeding the 1–2% amplitude threshold for robust *SLp* detection with the lowest LQR or AMP criterion (e.g. Figs 4 and 5b).

Considering three data-selection criteria such as the lowest LQR, AMP and Wilson *et al*. (2006), Fig. 13 further examines distance-dependent amplitudes of detected *SMp* and *SLp* and they are compared against theoretical *S*-to-*P* transmission coefficient (Aki & Richards 2002) from the L70 model (Fig. S1). Here we do not seek an optimal fit to the data, but simply show if the amplitude measurements in general follow the theoretical trend against epicentral distance. While there are still substantial amplitude fluctuations with respect to theoretical prediction against epicentral distance, in this particular example at station TJN, measurements from the lowest AMP criterion follows closest to the theoretical trend,

regardless the degree of regularization (Figs 13a and b vs. Figs 13c and d). As expected, the amplitude of *SMp* and *SLp* is notably modulated by the degree of regularization.

At least locally beneath the station TJN, a relatively sharp boundary with a negative velocity gradient is robustly identified in the LAS beneath the old Korea craton (Lee *et al*. 1998). While the exact nature and spatial extent of such a boundary deserves further analysis and discussion, it is beyond the scope of this paper and we will detail the findings beneath the entire Korea network in a subsequent paper. Also, another key potential source of contamination on SRFs is scattering from laterally-varying structure (Lekic & Fischer 2017).

Lastly, Fig. 14 displays AMP1 against data-selection percentage threshold for six different criteria. Similar to what we observe in the synthetics (Fig. 6), the results from real data analysis at station TJN also show that not only AMP1 decreases with increasing percentage threshold, but the lowest LQR or AMP criterion gives the lowest AMP1 than Wilson *et al*. (2006) or the random data selection does (Fig. 14), compatible with synthetic test in Section 3 (Fig. 6). Despite the criterion of Wilson *et al*. (2006) restrains SRFs within 60°–75° from shallow events, the lowest LQR or AMP criterion does concern SRFs across the entire distance range of 60°–85°, including a few SRFs from deep earthquakes as well. Furthermore, since the level of random noise reduction is proportional to the square-root of SRF number in the stacks, there is a trade-off between eliminating random noise and signal-generated noise. While random noise can be reduced by stacking, it is not the case for signal-generated noise. In comparison to the cases shown in Figs 11 and 12, while we can still detect *SMp* and *SLp* at 95% confidence level with a higher percentage threshold of 50%, the uncertainty of SRF amplitude does not decrease as expected for random noise (Figs S11 and S12). By inspection, if N is the data selection percentage threshold, multiplying AMP1 in Fig. 6 (noise free) with the square root of 100/N generally reproduces the pattern of AMP1 shown

in Fig. 14. This can be useful in the discussion on how to properly select N against random noise with respect to data quality and noise level.

In the case of our test, permanent station TJN provides about 300 quality data over 10 years after data prescreening. As we present the result with 25% selection threshold (or ~75 traces) for the detection of the *SLp* phase (Figs 11–13), we find a 15% selection threshold (or ~45 traces) with the low AMP criteria can still provide consistent SRF and *SLp* detection. Concerning typical PASSCAL experiments or temporal arrays over a 2-year period, depending on the aperture of the array, the number of stations, background noise level and the scale of lateral heterogeneity in the LAS, it is conceivable that a network of 5 stations can record 45 traces with low LQR and produce reasonably robust SRF stacks.

As evident in the synthetic test and real data analysis, high SNR of the *S* wave in the Q-component seismogram by itself does not necessarily warrant the quality of stacked SRFs. The data selection criterion proposed by Wilson *et al*. (2006) is favorable for a specific focal mechanism, but it is not necessarily a general scheme that takes into account the effect of radiation pattern on the excitation of mantle *P* coda waves or/and scattering waves between the source and receiver in the L-component seismogram. In this study, the LQR criterion, by design, makes a direct amplitude measurement of the scattering wave in the L component and contrasts it against the amplitude of the *S* wave in the Q component. Obviously, the application of LQR criteria in real data analysis slightly depends on the choice of measurement time window, which may be adapted. Alternatively, the AMP data selection criterion makes a direct assessment on the amplitude of *SP*, *sSP* and other related multiples in the SRF, making it an ideal proxy to indicate the strength of scattering waves away from the receiver side (e.g., Vinnik & Romonowicz 1991). Finally, these data selection criteria can be easily adapted to a different coordinate system (e.g., *P-SV-SH*) when desired.

5 Conclusions

Teleseismic scattered waves such as *S*-to-*P* converted phases (*Sdp*) provide enhanced sensitivity to localized velocity gradients across the lithospheric discontinuities. In this study, through systematic analysis of full-waveform synthetic waveforms and SRFs from catalogued earthquake focal mechanism and depth, we find that the strong *P* coda waves before the *S* wave recorded in the L component could result in the dubious *Sdp* phases in the synthetic SRFs before the *S* arrival. Furthermore, if the mean amplitude of SRFs after the *S* wave is large, dubious signals of SRFs before the *S* arrival become strong as well. Such signal-generated noise before the *S* arrival can be mistakenly interpreted as *Sdp* phase derived from lithosphere-asthenosphere system (LAS) beneath seismic stations.

To minimize the interference of *P* coda waves on *Sdp* phases in the LAS, we devise data-oriented criteria such as LQR, the amplitude ratio between *P* coda waves of the L-component waveform and the *S* wave of the Q-component waveform, and AMP, the amplitude of SRFs after the *S* arrival. These screening criteria provide a direct and straightforward attribute to measure and indicate the level of spurious energies before the *S* arrival in the SRF. With low LQR or AMP, regardless of the choice of deconvolution scheme, tapering or/and data windowing, unwanted signal-generated noise are largely removed, which improves the detection and quality of locally converted *Sdp* in the LAS. With the criteria such as the lowest LQR or AMP, the minimum amplitude threshold above which robust *SLp* can be detected is reduced down to about 1–2%, smaller than the amplitude threshold of 3–4% by the criterion of Wilson *et al*. (2006). The effectiveness of these criteria largely manifests the amplitude of *SP* wave as well as the control of *SV* radiation pattern in the scattering area on the amplitude of signal-generated noise due to *S*-to-*P* scattering (Vinnik & Romanowicz 1991). Applying the newly designed selection criteria to real data in the South Korea seismic

network, we demonstrate that the lowest LQR or AMP criterion provides robust detection of *SLp* beneath the test station TJN, offering a great potential to better characterize seismic discontinuities in the LAS.

Acknowledgements

Authors thank R. Kind (GFZ, Potsdam) for discussions. X. Shen acknowledges the National Natural Science Foundation of China (Grant 41874052 and 41574077), and National Key Research and Development Program of China (2017YFC1500100). Y. Kim and H. Lim acknowledge National Research Foundation of Korea Grant funded by the Korean Government (NRF-2014S1A2A2027609), and Korea Meteorological Administration Research and Development Program under Grant KMI 2018-02910. T.-R. A. Song acknowledges the support by the Natural Environment Research Council, UK (NE/P001378/1). Synthetic waveforms are computed using the high-performance computation facility, GRACE, at University College London. Receiver functions are computed with the codes provided by L. Zhu (Saint Louis University) (http://www.eas.slu.edu/People/LZhu/home.html). Some figures were plotted with Generic Mapping Tools (Wessel & Smith 1995). Lastly, authors thank the Editor A. Morelli, W. Geissler and an anonymous reviewer who helped improve this paper.

References

Abt, D. L., Fischer, K. M., French, S. W., Ford, H., Yuan, A. H. & Romanowicz, B., 2010. North American lithospheric discontinuity structure imaged by Ps and Sp receiver functions, *Journal of Geophysical Research: Solid Earth*, ***115***(B9), https://doi.org/10.1029/2009JB006914.

Aki, K. & Richards, P.G., 2002. Quantitative Seismology, 2nd Ed. *University Science Books*, ISBN 0-935702-96-2.

Bagley, B. & Revenaugh, J., 2008. Upper mantle seismic shear discontinuities of the Pacific, *Journal of Geophysical Research: Solid Earth*, ***113***(B12), https://doi.org/10.1029/2008JB005692.

Bock, B., 1994. Multiples as precursors to S, SKS and ScS, *Geophysical Journal International*, ***119***, 421–427.

Dziewonski, A., Chou, T. A. & Woodhouse, J., 1981. Determination of earthquake source parameters from waveform data for studies of global and regional seismicity, *Journal of Geophysical Research: Solid Earth*, ***86***(B4), 2825–2852, https://doi.org/10.1029/JB086iB04p02825.

Eaton, D. W., Darbyshire, F., Evans, R. L., Grütter, H., Jones, A. G. & Yuan, X., 2009. The elusive lithosphere–asthenosphere boundary (LAB) beneath cratons, *Lithos*, ***109***(1–2), 1–22, https://doi.org/10.1016/j.lithos.2008.05.009.

Efron, B. & Tibshirani, R., 1998. The problem of regions, *Annals of Statistics*, 1687–1718.

Ekström, G., Nettles, M. & Dziewoński, A., 2012. The global CMT project 2004–2010: Centroid-moment tensors for 13,017 earthquakes, *Physics of the Earth and Planetary Interiors*, ***200***, 1–9, https://doi.org/10.1016/j.pepi.2012.04.002.

Farra, V. & Vinnik, L., 2000. Upper mantle stratification by P and S receiver functions, *Geophysical Journal International*, ***141***(3), 699–712, https://doi.org/10.1046/j.1365-246x.2000.00118.x.

Fischer, K. M., Ford, H. A., Abt, D. L. & Rychert, C. A., 2010. The lithosphere-asthenosphere boundary, *Annual Review of Earth and Planetary Sciences*, ***38***, 551–575, https://doi.org/10.1146/annurev-earth-040809-152438.

Ford, H. A., Fischer, K. M., Abt, D. L., Rychert, C. A. & Elkins-Tanton, L. T., 2010. The lithosphere–asthenosphere boundary and cratonic lithospheric layering beneath Australia from Sp wave imaging. *Earth and Planetary Science Letters*, ***300***(3–4), 299–310. doi:10.1016/j.epsl.2010.10.007.

Fuchs, K. & Müller, G., 1971. Computation of synthetic seismograms with the reflectivity method and comparison with observations, *Geophysical Journal International*, ***23***(4), 417–433, https://doi.org/10.1111/j.1365-246X.1971.tb01834.x.

Hansen, S. E., Nyblade, A. N., Julia, J., Dirks, P. H. G. M. & Durrheim, R. J., 2009. Upper-mantle low-velocity zone structure beneath the Kaapvaal craton from S-wave receiver functions, *Geophysical Journal International*, ***178***(2), 1021–1027, https://doi.org/10.1111/j.1365-246X.2009.04178.x.

Hopper, E. & Fischer, K. M., 2015. The meaning of midlithospheric discontinuities: A case study in the northern US craton, *Geochemistry, Geophysics, Geosystems*, ***16***(12), 4057–4083, https://doi.org/10.1002/2015GC006030.

Karato, S.-i., 2012. On the origin of the asthenosphere, *Earth and Planetary Science Letters*, ***321***, 95–103, https://doi.org/10.1016/j.epsl.2012.01.001.

Kawai, K., Takeuchi, N. & Geller, R. J., 2006. Complete synthetic seismograms up to 2 Hz for transversely isotropic spherically symmetric media, *Geophysical Journal International*, ***164***(2), 411–424, https://doi.org/10.1111/j.1365-246X.2005.02829.x.

Kawakatsu, H. & Utada, H., 2017. Seismic and electrical signatures of the lithosphere–asthenosphere system of the normal oceanic mantle, *Annual Review of Earth and Planetary Sciences*, ***45***, 139–167, https://doi.org/10.1146/annurev-earth-063016-020319.

Kawakatsu, H., Kumar, P., Takei, Y., Shinohara, M., Kanazawa, T., Araki, E. & Suyehiro, K., 2009. Seismic evidence for sharp lithosphere-asthenosphere boundaries of oceanic plates, *Science*, ***324***(5926), 499–502, https://doi.org/10.1126/science.1169499.

Kennett, B. & Engdahl, E., 1991. Traveltimes for global earthquake location and phase identification, *Geophysical Journal International*, ***105***(2), 429–465, https://doi.org/10.1111/j.1365-246X.1991.tb06724.x.

Kind, R., Yuan, X., & Kumar, P., 2012. Seismic receiver functions and the lithosphere-asthenosphere boundary, Tectonophysics, **536–537**, 25–43, doi:10.1016/j.tecto.2012.03.005, 2012.

Kind, R., Yuan, X., Mechie, J. & Sodoudi, F., 2015. Structure of the upper mantle in the north-western and central United States from USArray S-receiver functions, *Solid Earth*, ***6***(3), 957.

Kumar, P., Yuan, X., Kind, R. & Mechie, J., 2012. The lithosphere-asthenosphere boundary observed with USArray receiver functions, *Solid Earth*, ***3***(1), 149.

Kumar, P., Kind, R., Hanka, W., Wylegalla, K., Reigber, C., Yuan, X., Woelbern, I., Schwintzer, P., Fleming, K. & Dahl-Jensen, T., 2005. The lithosphere–asthenosphere boundary in the North-West Atlantic region, *Earth and Planetary Science Letters*, ***236***(1–2), 249–257, https://doi.org/doi.org/10.1016/j.epsl.2005.05.029.

Langston, C. A., 1977. Corvallis, Oregon, crustal and upper mantle receiver structure from teleseismic P and S waves, *Bulletin of the Seismological Society of America*, ***67***(3), 713–724.

Lee, C.-T. A., Luffi, P. & Chin, E. J., 2011. Building and destroying continental mantle, *Annual Review of Earth and Planetary Sciences*, ***39***, 59–90, https://doi.org/10.1146/annurev-earth-040610-133505.

Lee, K.-S., Chang, H.-W. & Park, K.-H., 1998. Neoproterozoic bimodal volcanism in the central Ogcheon belt, Korea: age and tectonic implication. *Precambrian Research*, ***89***, 47–57.

Lekic, V. & Fischer, K. M., 2014. Contrasting lithospheric signatures across the western United States revealed by Sp receiver functions, *Earth and Planetary Science Letters*, ***402***, 90–98, https://doi.org/10.1146/j.epsl.2013.11.026.

Lekic, V. & Fischer, K. M., 2017. Interpreting spatially stacked Sp receiver functions, *Geophysical Journal International*, ***210***(2), 874–886, https://doi.org/10.1093/gji/ggx206.

Lim, H., Kim, Y., Song, T.-R. A. & Shen, X., 2018. Measurement of seismometer orientation using the tangential P-wave receiver function based on harmonic decomposition, *Geophysical Journal International*, ***212***(3), 1747–1765, https://doi.org/10.1093/gji/ggx515.

Nettles, M. & Dziewoński, A. M., 2008. Radially anisotropic shear velocity structure of the upper mantle globally and beneath North America, *Journal of Geophysical Research: Solid Earth*, ***113***(B2), https://doi.org/10.1029/2006JB004819.

Robinson, E. A. & Treitel, S., 1967. Principles of digital wiener filtering, *Geophysical Prospecting*, ***15***(3), 311–332, https://doi.org/10.1111/j.1365-2478.1967.tb01793.x.

Rondenay, S., 2009. Upper mantle imaging with array recordings of converted and scattered teleseismic waves, *Surveys in Geophysics*, ***30***(4–5), 377–405, https://doi.org/10.1007/s10712-009-9071-5.

Rychert, C. A. & Shearer, P. M., 2011. Imaging the lithosphere-asthenosphere boundary beneath the Pacific using SS waveform modeling, *Journal of Geophysical Research: Solid Earth*, ***116***(B7), https://doi.org/10.1029/2010JB008070.

Rychert, C. A., Rondenay, S. & Fischer, K. M., 2007. P-to-S and S-to-P imaging of a sharp lithosphere-asthenosphere boundary beneath eastern North America, *Journal of Geophysical Research: Solid Earth*, ***112***(B8), https://doi.org/10.1029/2006JB004619.

Schmerr, N., 2012. The Gutenberg discontinuity: Melt at the lithosphere-asthenosphere boundary, *Science*, ***335***(6075), 1480–1483, https://doi.org/10.1126/science.1215433.

Selway, K., Ford, H. & Kelemen, P., 2015. The seismic mid-lithosphere discontinuity, *Earth and Planetary Science Letters*, ***414***, 45–57, https://doi.org/10.1016/j.epsl.2014.12.029.

Shen, X., Yuan, X. & Ren, J., 2015. Anisotropic low-velocity lower crust beneath the northeastern margin of Tibetan Plateau: Evidence for crustal channel flow, *Geochemistry, Geophysics, Geosystems*, ***16***(12), 4223–4236, https://doi.org/10.1002/2015GC005952.

Shen, X., Liu, M., Gao, Y., Wang, W., Shi, Y., An, M., Zhang, Y. & Liu, X., 2017. Lithospheric structure across the northeastern margin of the Tibetan Plateau: Implications for the plateau's lateral growth, *Earth and Planetary Science Letters*, ***459***, 80–92, https://doi.org/10.1016/j.epsl.2016.11.027

Svenningsen, L. & Jacobsen, B. H., 2004. Comment on "Improved inversion for seismic structure using transformed, S-wavevector receiver functions: Removing the effect of the free surface" by Anya Reading, Brian Kennett, and Malcolm Sambridge, *Geophysical Research Letters*, **31**(L24609), doi:10.1029/2004GL021413.

Takeuchi, N., Geller, R. J. & Cummins, P. R., 1996. Highly accurate P-SV complete synthetic seismograms using modified DSM operators, *Geophysical Research Letters*, ***23***(10), 1175–1178, https://doi.org/10.1029/96GL00973.

Tan, Y. & Helmberger, D. V., 2007. Trans-Pacific upper mantle shear velocity structure, *Journal of Geophysical Research: Solid Earth*, ***112***(B8), https://doi.org/10.1029/2006JB004853.

Tharimena, S., Rychert, C., Harmon, N. & White, P., 2017. Imaging Pacific lithosphere seismic discontinuities – Insights from SS Precursor modeling. *Journal of Geophysical Research: Solid Earth*, ***122***(3), 2131–2152. doi:10.1002/2016JB013526.

Vinnik, L. P., 1981. Evaluation of the effective cross-section of scattering in the lithosphere, *Physics of the Earth Planetary Interiors*, ***26***, 268-284.

Vinnik, L. P. & Romanowicz, B. A., 1991. Origin of precursors to teleseismic S waves, *Bulletin of the Seismological Society of America*, ***81***(4), 1216–1230.

Wang, R., 1999. A simple orthonormalization method for stable and efficient computation of Green's functions, *Bulletin of the Seismological Society of America*, ***89***(3), 733–741.

Wessel, P., & Smith, W. H., 1995. New version of the generic mapping tools: Eos, Transactions, *American Geophysical Union*, ***76***, 326–329, https://doi.org/10.1029/95EO00198.

Wilson, D. C., Angus, D., Ni, J. F. & Grand, S. P., 2006. Constraints on the interpretation of S-to-P receiver functions, *Geophysical Journal International*, ***165***(3), 969–980, https://doi.org/10.1111/j.1365-246X.2006.02981.x.

Yuan, X., Kind, R., Li, X. & Wang, R., 2006. The S receiver functions: synthetics and data example, *Geophysical Journal International*, ***165***(2), 555–564, https://doi.org/10.1111/j.1365-246X.2006.02885.x.

Figures

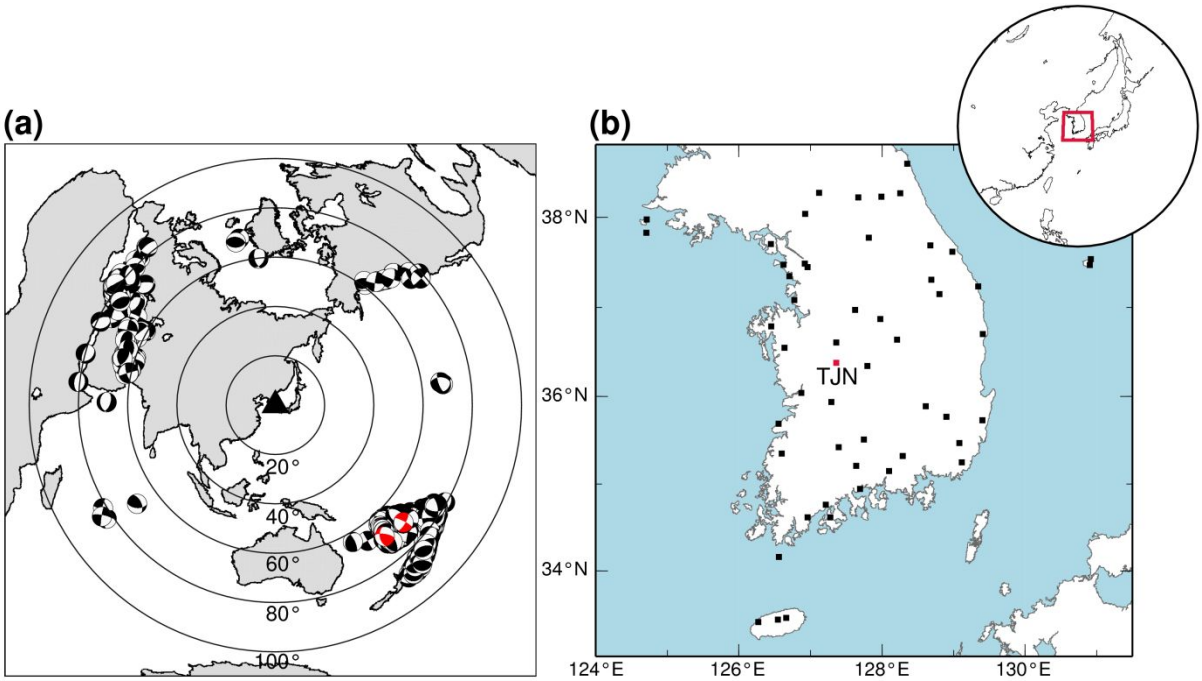

Figure 1. Distribution of earthquakes with magnitude greater than 5.5 and South Korea seismic network. (a) Distribution of earthquakes within the epicentral distances of 60°–85° from the center of the Korean seismic network (black triangle). The Centroid Moment Tensor (CMT) solutions of the events are from Dziewonski *et al*. (1981) and Ekstrom *et al*. (2012). Two earthquakes for synthetics in Fig. 3 are highlighted in red. (b) South Korea seismic network. Broadband seismic stations are shown in black squares, and the only station is labelled with the station ID (TJN).

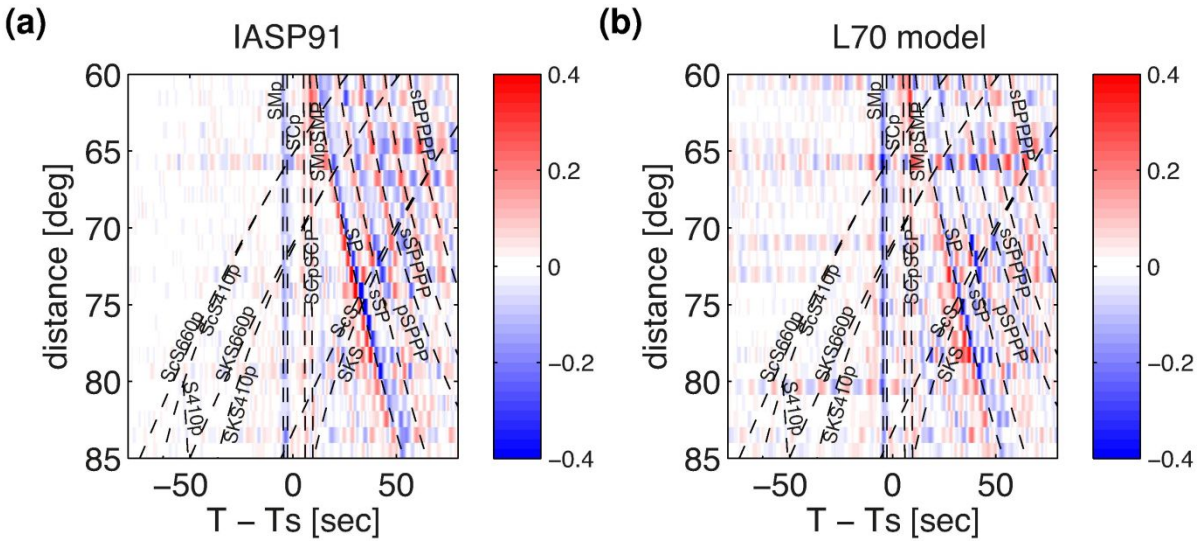

Figure 2. Stacks of 300 synthetic SRFs as a function of the epicentral distance of 60°–85°. The SRFs are binned with a distance of a 1° window and stacked, and their amplitudes are displayed in blue-to-red color. Theoretical phase arrival times from the IASP91 model (Kennett & Engdahl 1991) are marked as dashed lines with phase names labeled. (a) Synthetic SRFs calculated from the IASP91 model (Kennett & Engdahl 1991). (b) Synthetic SRFs from L70 model (Fig. S1).

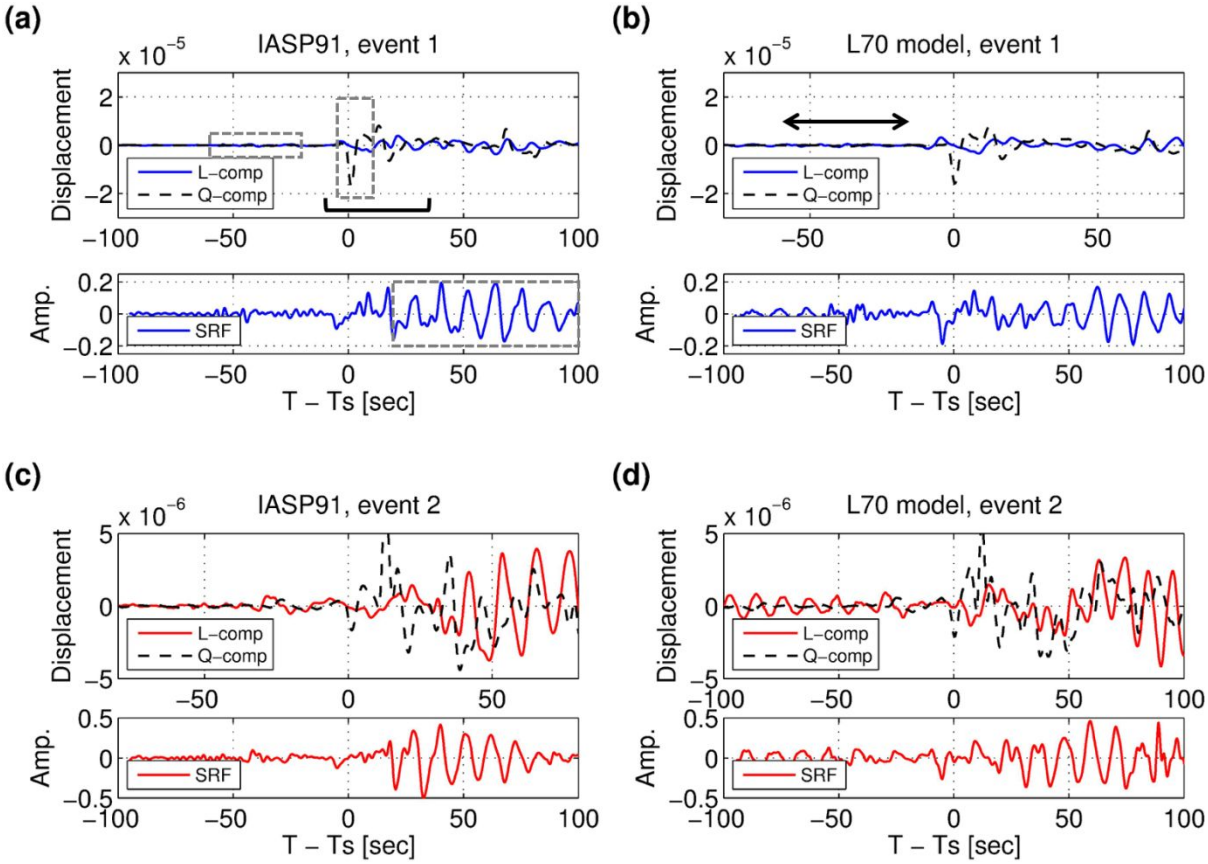

Figure 3. Examples showing *P* coda waves and their influence on signal-generated noise in the SRF. Gray dashed boxes in panel (a) indicate how LQR is measured from the L- and Q-component synthetic seismograms and how AMP is measured from synthetic SRF. Synthetic waveforms are computed from two earthquake sources (Fig. 1a, red beachballs) using the IASP91 (Kennett & Engdahl 1991) (a and c) and the L70 model (Fig. S1) (b and d). *S*-wave arrivals are aligned at zero time in the Q-component waveforms (dashed lines), and a time window for *P* coda waves are marked in a panel b (double arrow). Time-domain Wiener deconvolution method with minimum regularization (0.01% white noise) is performed within the parent waveform time window of 10 s before and 35 s after the *S* arrival (black bar in a panel a). Note the amplitude scale of SRF in case 2 is higher than that in case 1. See Figs S2 and S3 for cases for the time window of [-10 s 15 s] and [-10 s 10 s] with respect to *S* arrival, respectively.

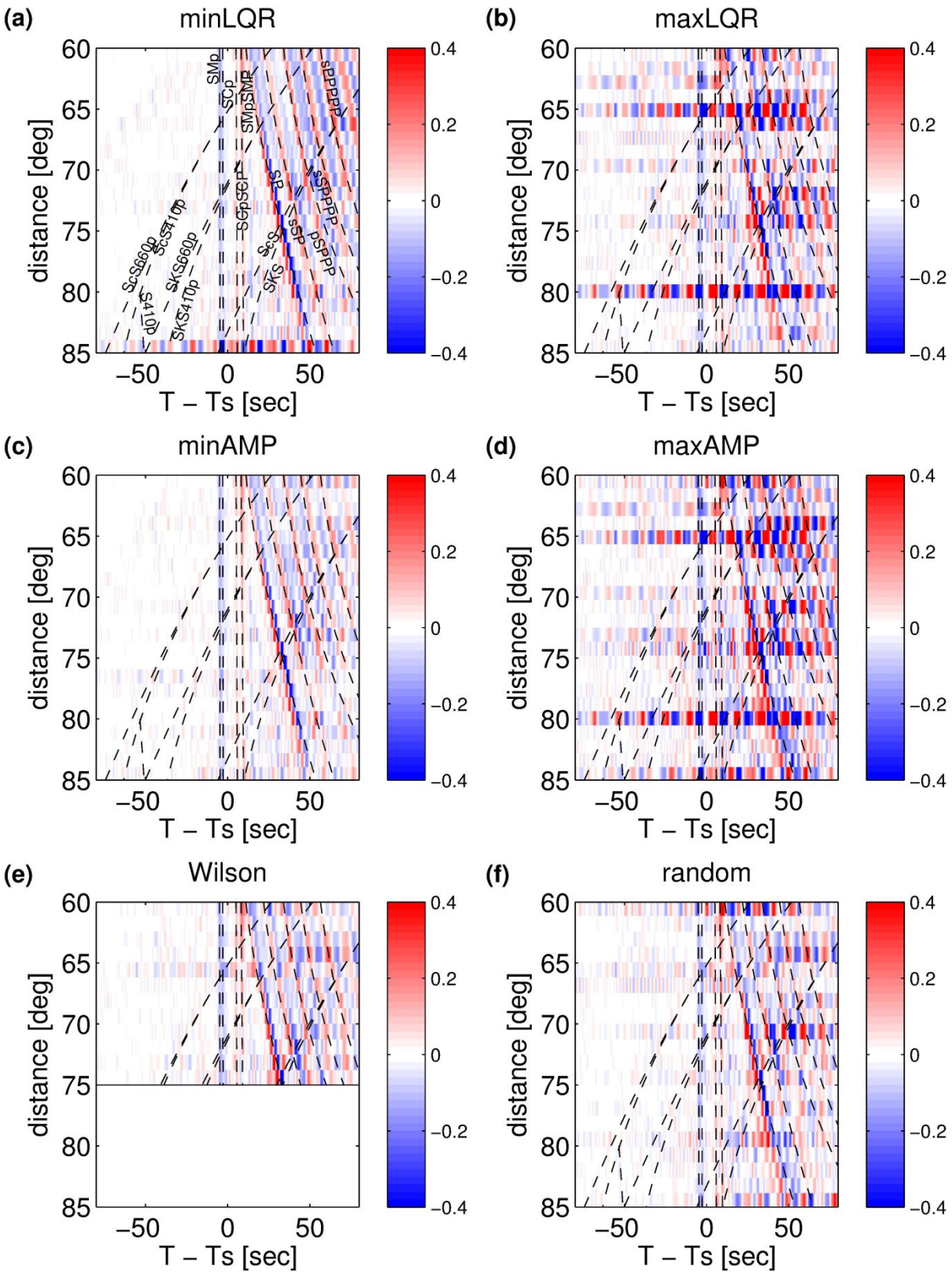
(a)
minLQR
(b)
maxLQR
(c)
minAMP
(d)
maxAMP
(e)
Wilson
(f)
random
distance [deg]
T – Ts [sec]
60
65
70
75
80
85
–50
0
50
0.4
0.2
0
–0.2
–0.4
SMo
SCp
SMpSMP
sPPPPP
SP
sSPPPP
sSP
pSPPP
ScS
SKS
ScS660p
ScS410p
SKS660p
SKS410p
S410p

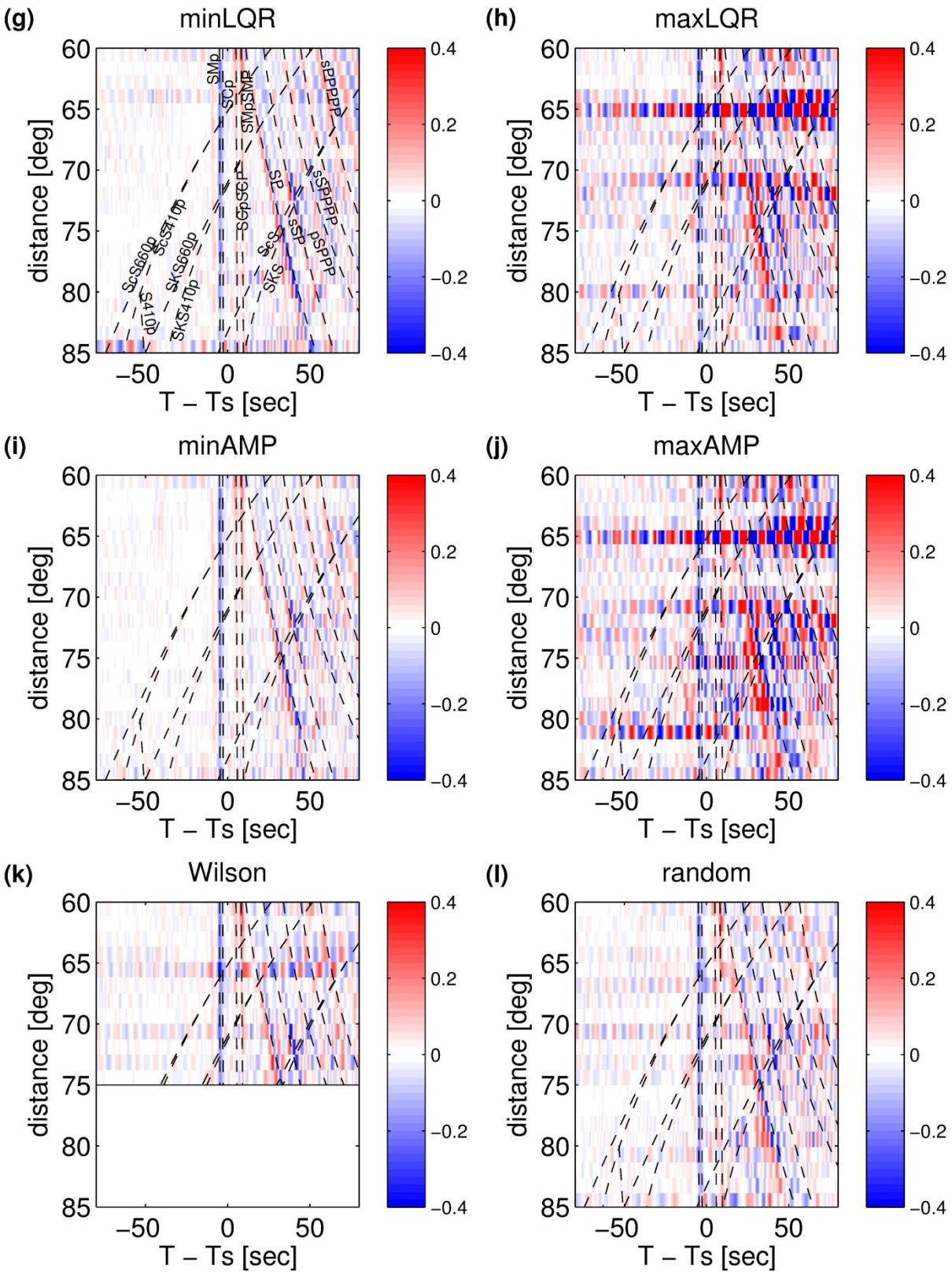

759

760

761 **Figure 4**. Images of synthetic SRFs for the IASP91 model (a–f) and L70 model (g–l) against

762 epicentral distance and six data selection criteria. The SRFs are plotted in the same way as

Fig. 2. (a, g) Stacked SRFs with the 25% lowest LQR. (b, h) Stacked SRFs with the 25% highest LQR. (c, i) Stacked SRFs with the 25% lowest AMP. (d, j) Stacked SRFs with the 25% highest AMP. (e, k) Stacked SRFs with the criterion by Wilson *et al*. (2006). Note that Wilson *et al*. (2006) used restricted epicentral distances of 60°–75° for earthquakes with focal depths shallower than 300 km. (f, l) Stacked SRFs with 25% random data selection. Dashed lines indicate phase arrival times predicted by the IASP91 model.

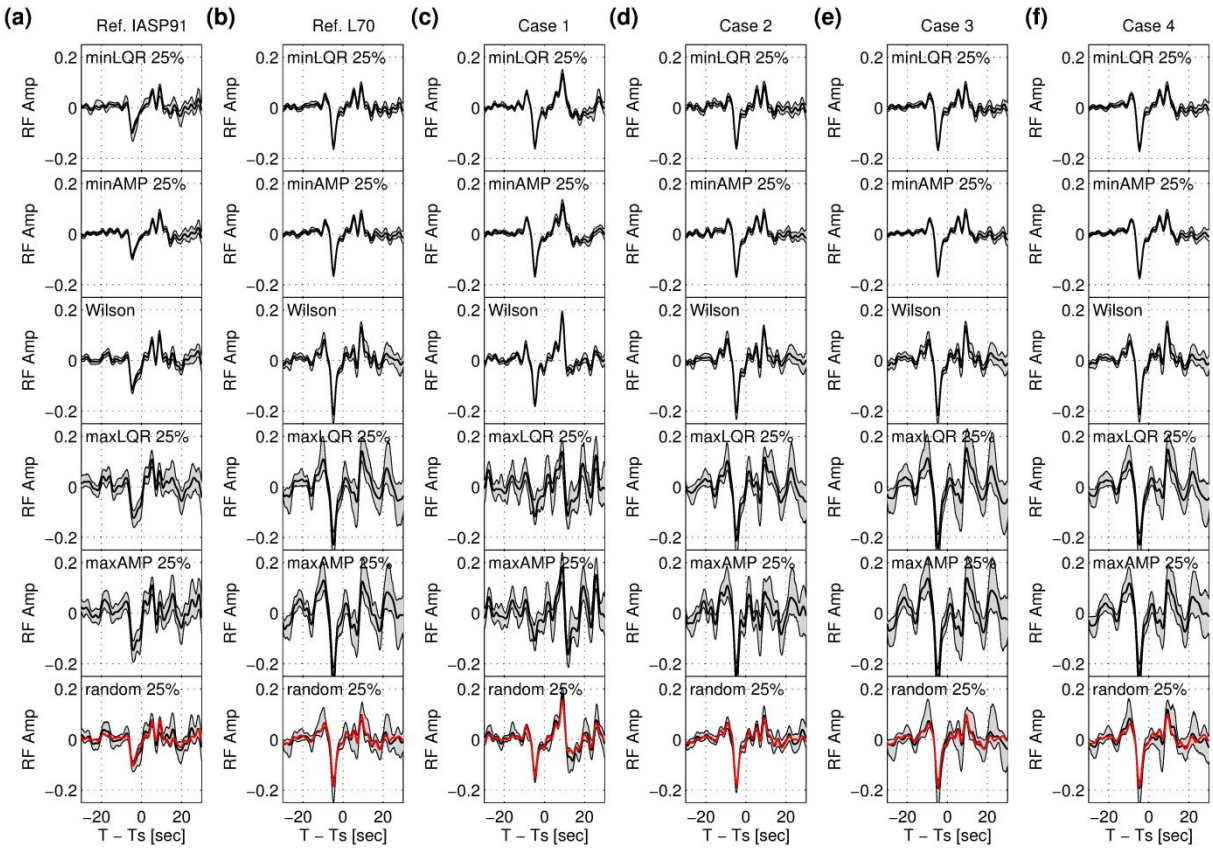

Figure 5. Stacked SRFs for various cases against six data selection criteria: 25% lowest LQR, 25% lowest AMP, the criterion by Wilson *et al*. (2006), 25% highest LQR, and 25% highest AMP, and 25% random data selection, from the top to bottom rows, respectively. Gray region indicates bootstrap error estimates of the SRFs. (a) Stacked SRFs for IASP91 model. (b) Stacked SRFs for L70 model. (c) Stacked SRFs for the case 1; same as (b) but with the window of parent waveform -10 s before and 15 s after the *S* wave. (d) Stacked SRFs for the case 2; same as (b) but with the Hanning tapering window of 5%. (e) Stacked SRFs for the case 3; same as (b), but with frequency-domain water-level deconvolution and water level of 0.05%. (f) Stacked SRFs for the case 4; same as (b), but with frequency-domain water-level deconvolution and water level of 0.2%. Note stacked SRFs without any selection criteria are shown in red lines for comparisons. The stack of all traces is shown in red in the bottom panel.

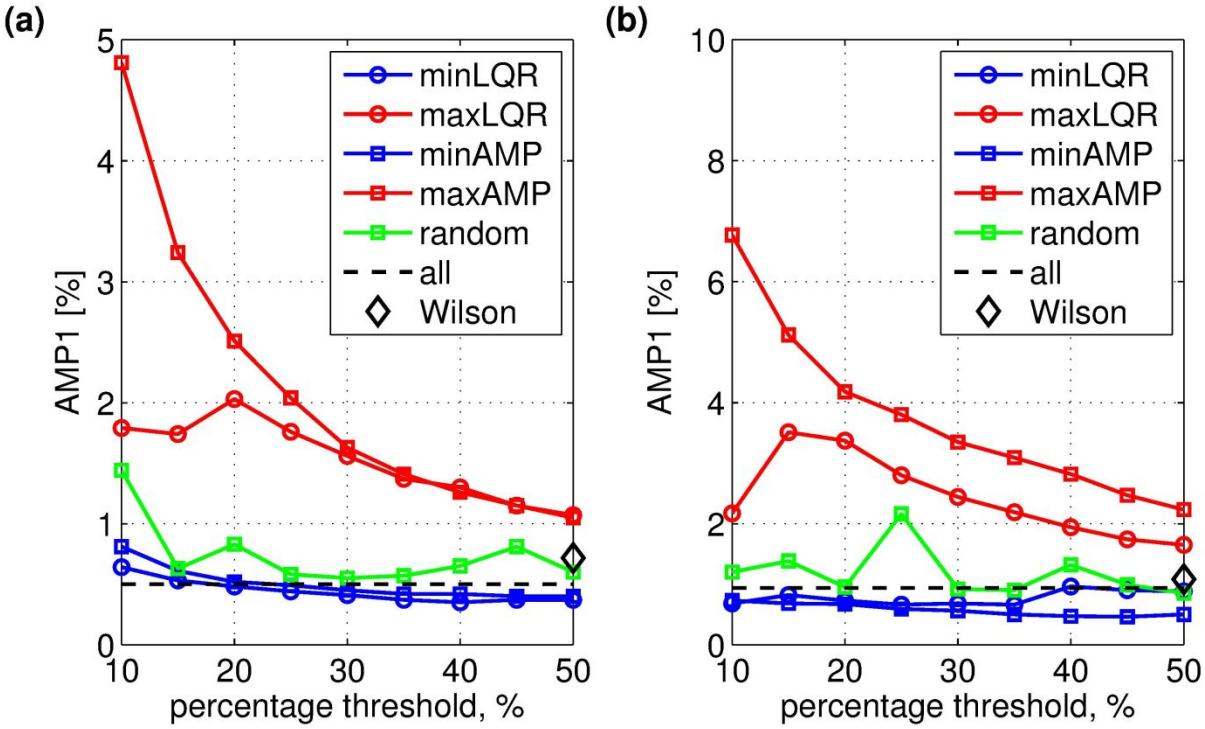

Figure 6. Root-mean-square (RMS) amplitudes of the synthetic SRFs at -60 to -20 s with respect to the *S* arrival (AMP1 in %), plotted against data-selection ratios (10–50%). (a) AMP1 for IASP91 model (Kennett & Engdahl 1991) with six criteria, which are lowest LQR (blue circle), highest LQR (red circle), lowest AMP (blue square), highest AMP (red square), random data selection (green square) and the criterion by Wilson *et al.* (2006) (black diamond), in addition to all SRFs (black dashed line). (b) AMP1 for L70 model (Fig. S1) with the same criteria as (a).

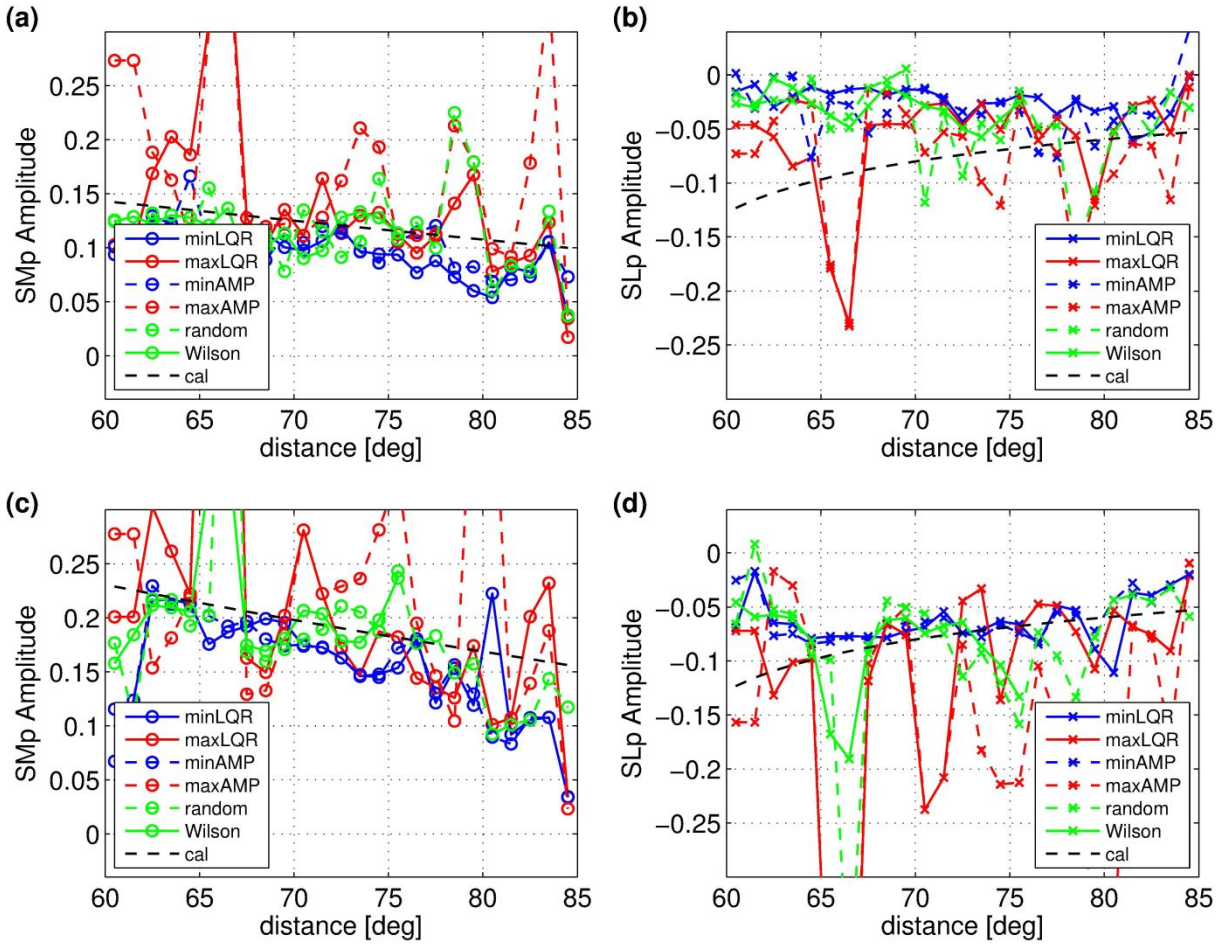

Figure 7. Amplitudes of *SMp* and *SLp* phases from the synthetic SRFs, plotted against the epicentral distance for the six different data selection criteria. The measured amplitudes are compared with the theoretical transmission coefficients (Aki & Richards 2002), shown in black dashed line. (a) Distance-dependent amplitude of *SMp* from IASP91 model (Kennett & Engdahl 1991). (b) Distance-dependent amplitude of *SLp* from IASP91 model. (c) Distance-dependent amplitude of *SMp* from L70 model (Fig. S1). (d) Distance-dependent amplitude of *SLp* from L70 model. Note that the theoretical calculation of *SLp* transmission coefficient from the L70 model is reproduced in Fig. 7b for comparison. In the absence of a negative velocity contrast in the IASP91 model, notable amplitude peak, especially with the highest LQR or AMP criteria, can still be identified and potentially misinterpreted as *SLp* signal in the LAS. Lowest LQR or AMP criteria substantially minimize these dubious signals.

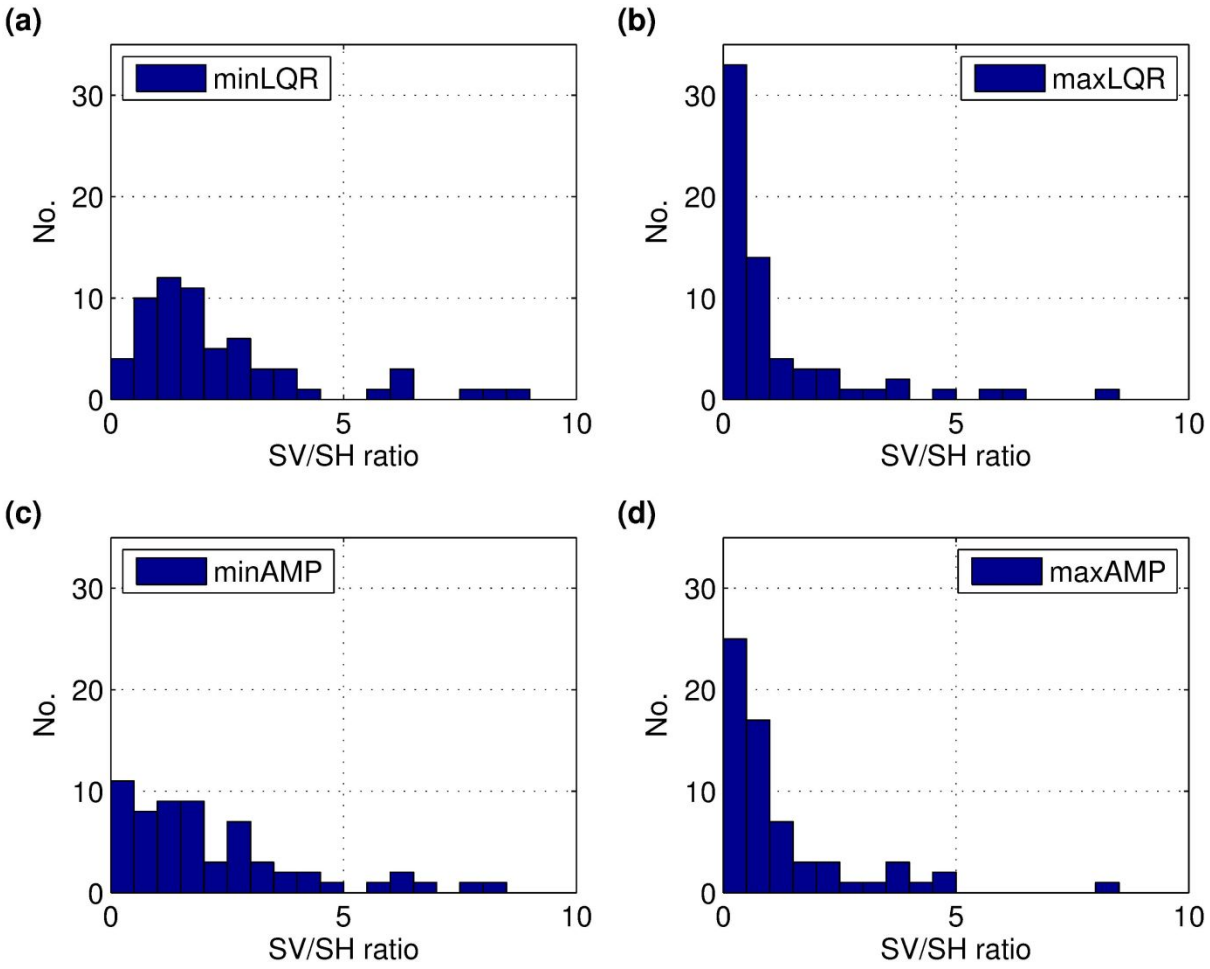

Figure 8. Histograms of *SV/SH* ratio against four data selection criteria; (a) 25% lowest LQR, (b) 25% highest LQR, (c) 25% lowest AMP, and (d) 25% highest AMP.

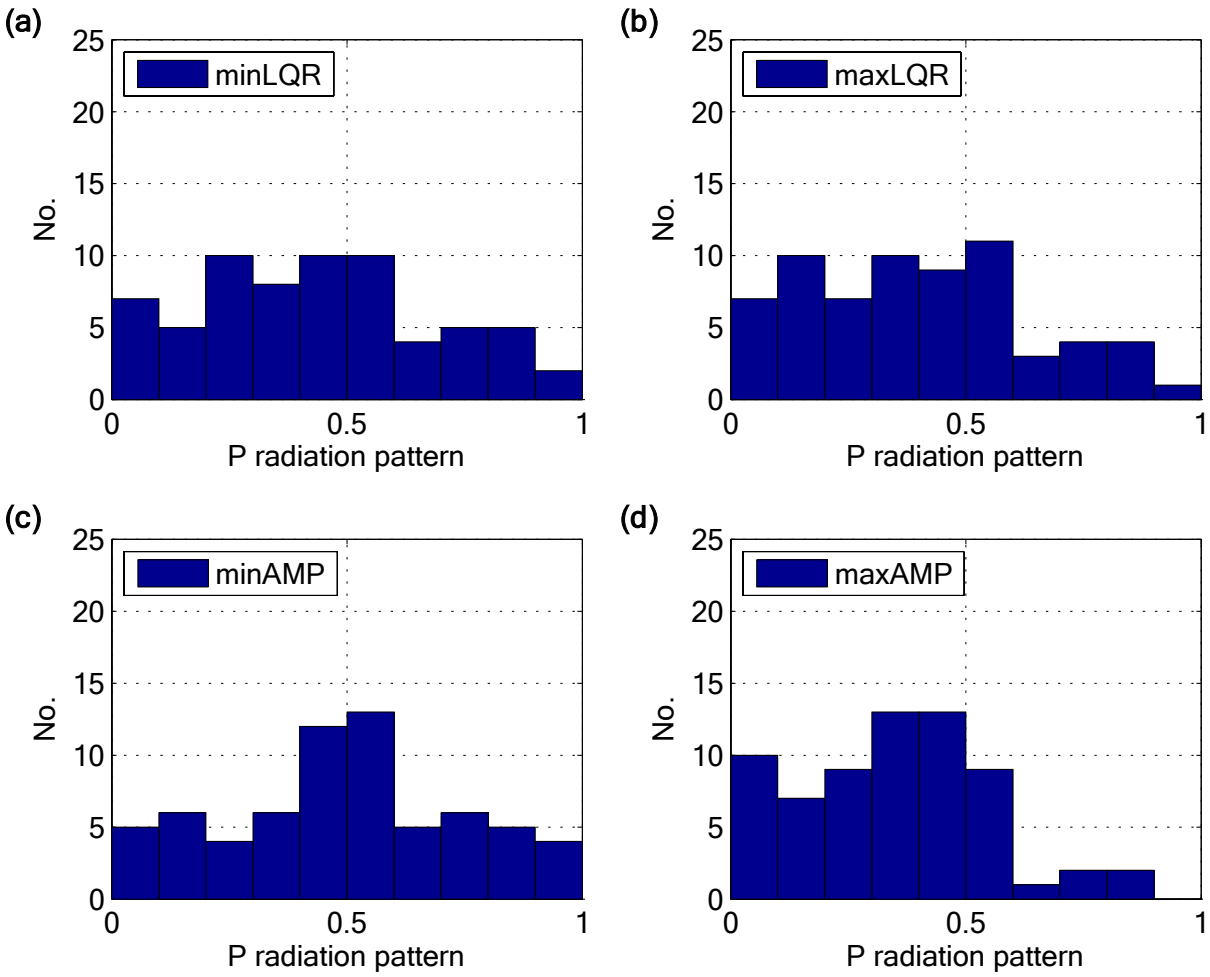

Figure 9. Histograms of *P* radiation pattern against four data selection criteria; (a) 25% lowest LQR, (b) 25% highest LQR, (c) 25% lowest AMP, and (d) 25% highest AMP. The *P* radiation pattern is computed with the slowness of *pPPPP* against focal mechanisms of selected events.

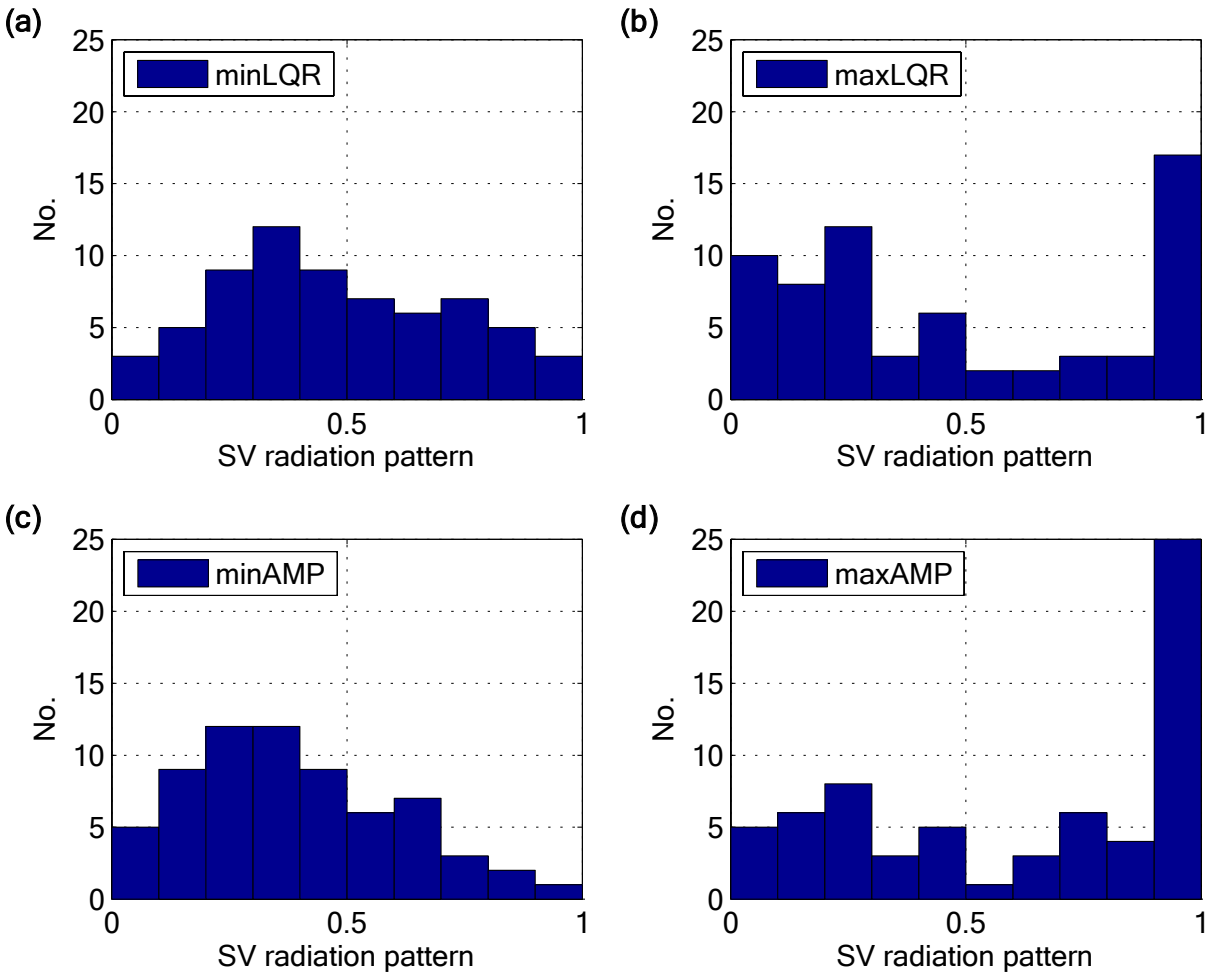

Figure 10. Histograms of *SV* radiation pattern against four data selection criteria; (a) 25% lowest LQR, (b) 25% highest LQR, (c) 25% lowest AMP, and (d) 25% highest AMP. The *SV* radiation pattern is computed with the slowness of *SP* wave against focal mechanisms of selected events.

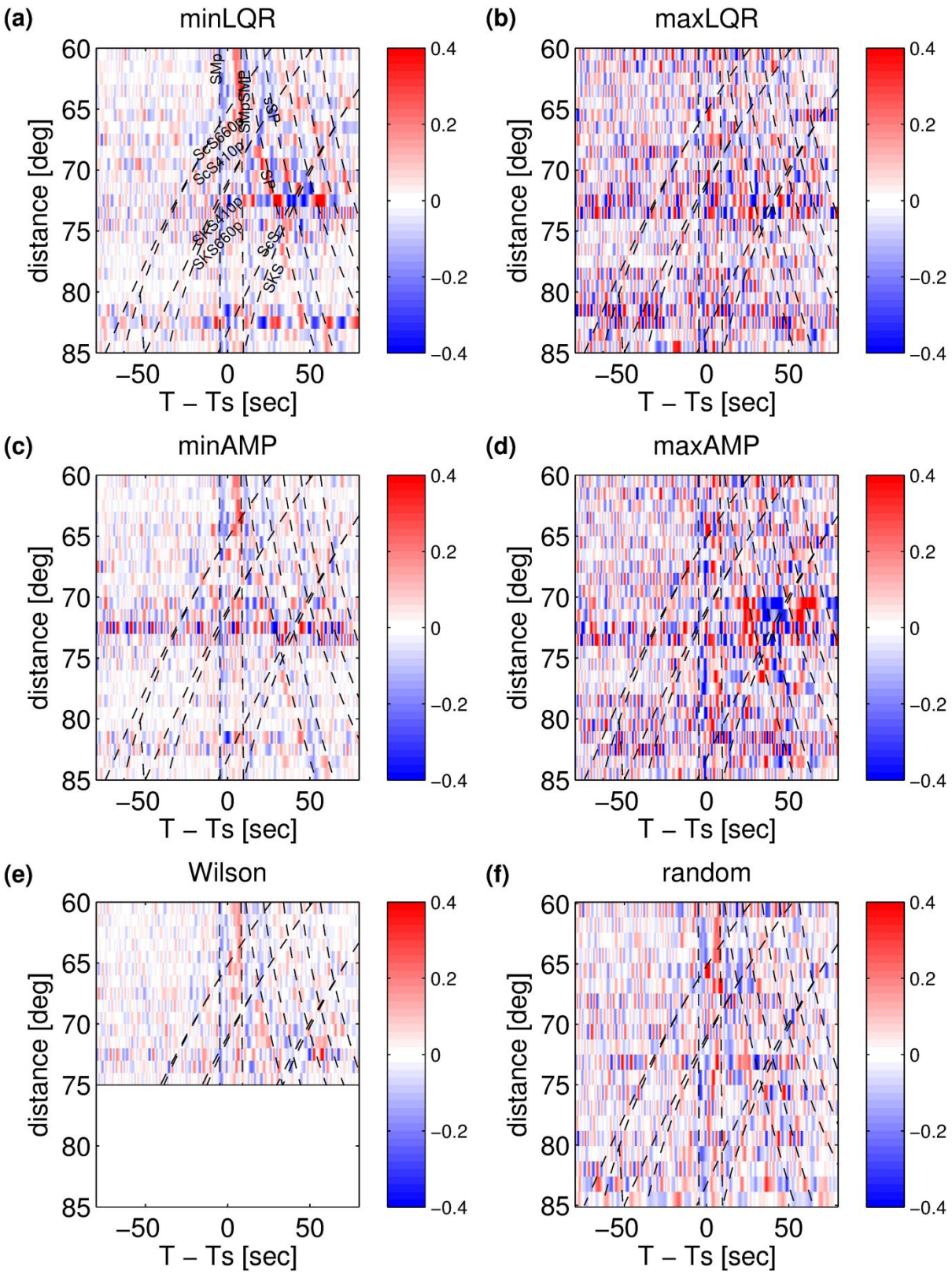

Figure 11. Images of SRFs for station TJN as a function of the distance of 60°–85° with six different data selection criteria. The SRFs are plotted in the same way as Fig. 2. (a) Stacked SRFs with the 25% lowest LQR. (b) Stacked SRFs with the 25% highest LQR. (c) Stacked

SRFs with the 25% lowest AMP. (d) Stacked SRFs with the 25% highest AMP. (e) Stacked SRFs with the criterion by Wilson *et al*. (2006). (f) Stacked SRFs with 25% random data selection. Dashed lines indicate phase arrival times predicted by the IASP91 model. See Fig. S10 for the images of -30–30 s time window.

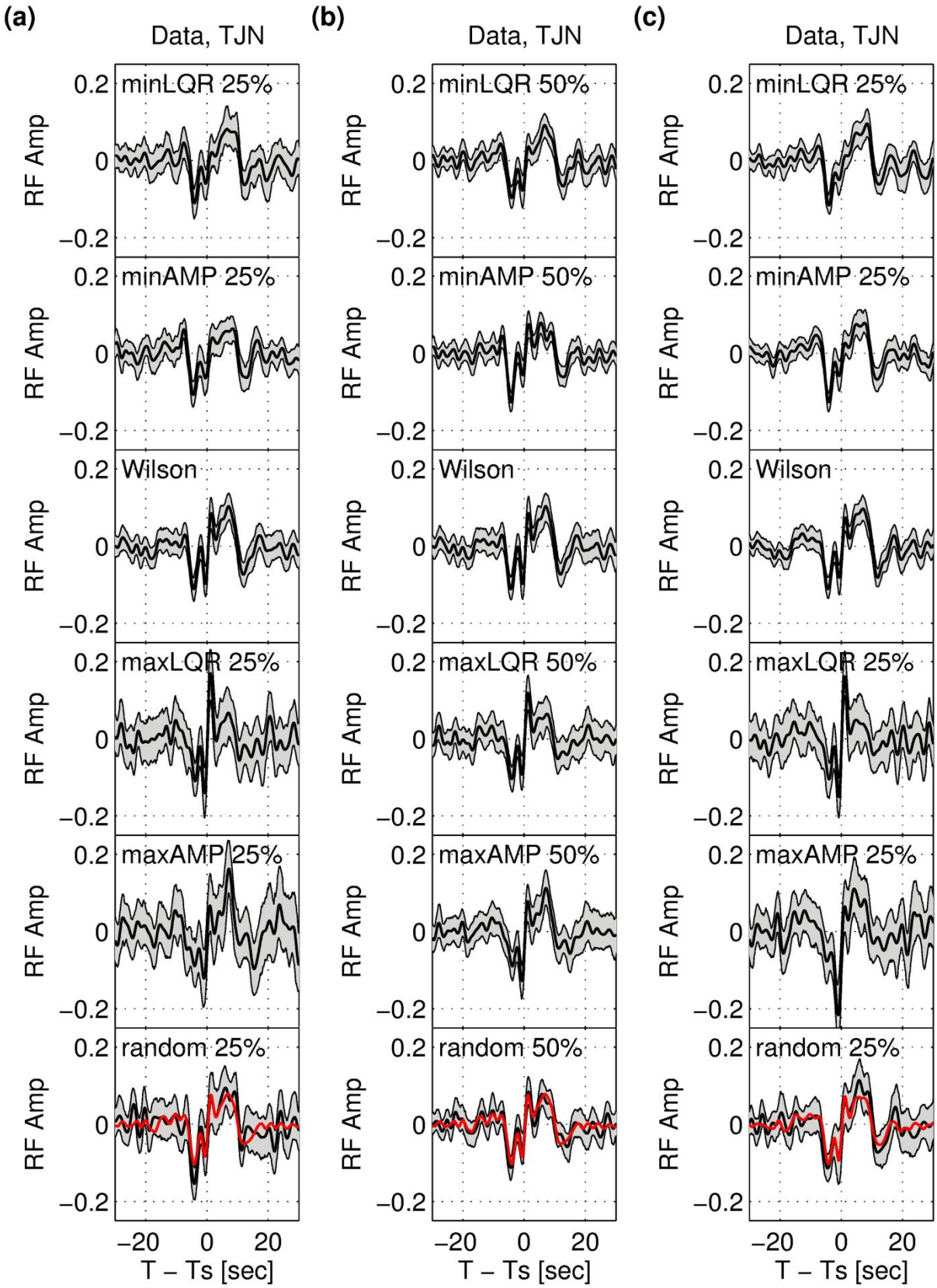

Figure 12. Stacked SRFs for station TJN with six data selection criteria with (a) a percentage threshold of 25%, (b) 50 %, and (b) 25% with a stronger regularization (1% white noise).

Gray region indicates bootstrap error estimates of the SRFs. The six data selection criteria are as follows: 25% lowest LQR, 25% lowest AMP, the criterion by Wilson *et al*. (2006), 25% highest LQR, and 25% highest AMP, and 25% random data selection, from the top to bottom rows, respectively.

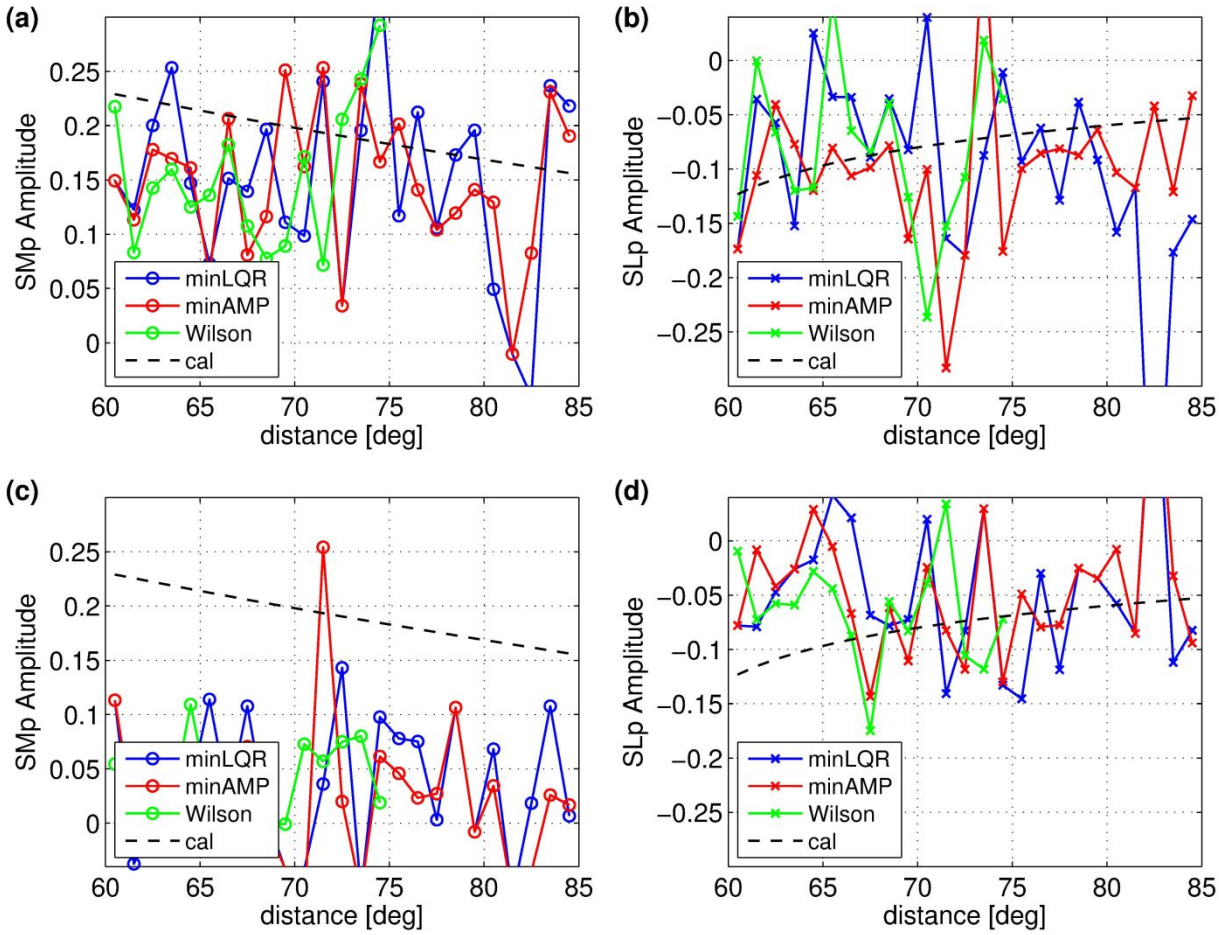

Figure 13. Amplitudes of *SMp* and *SLp* phases from the SRFs for station TJN, plotted against the distance of 60°–85° for three different data selection criteria (25% lowest LQR, 25% lowest AMP, and the criterion by Wilson *et al*. (2006)). The measured amplitudes are compared with the theoretical transmission coefficients (Aki & Richards 2002), shown in black dashed line. (a) Distance-dependent amplitude of *SMp*. (b) Distance-dependent amplitude of *SLp*. (c) Distance-dependent amplitude of *SMp* with a strong regularization (1% white noise). (d) Distance-dependent amplitude of *SLp* with a strong regularization (1% white noise).

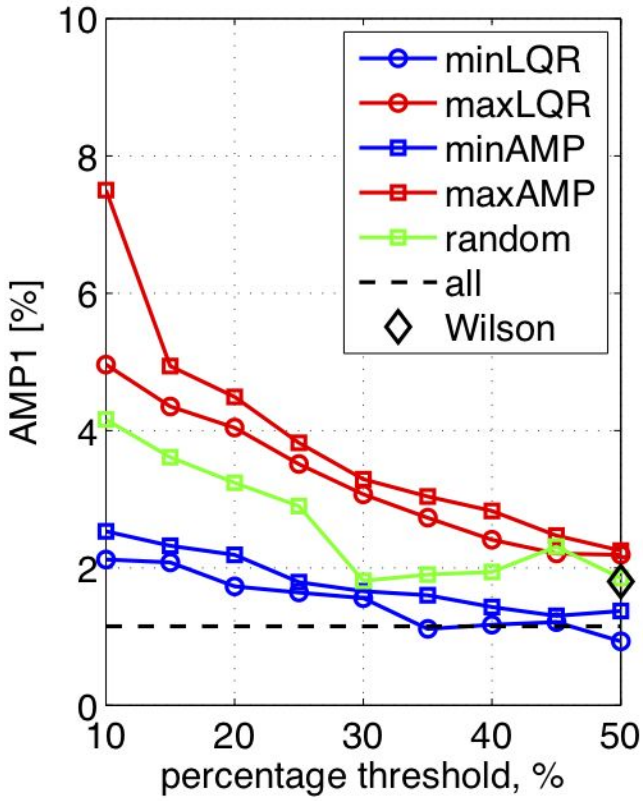

Figure 14. Root-mean-square (RMS) amplitudes of the SRFs at -60 to -20 s with respect to the *S* arrival (AMP1 in %) for station TJN, plotted against data-selection ratios (10–50%). The six data selection criteria are as follows: lowest LQR (blue circle), highest LQR (red circle), lowest AMP (blue square), highest AMP (red square), random data selection (green square) and the criterion by Wilson *et al*. (2006) (black diamond), in addition to all SRFs (black dashed line).

Supporting Information

Additional Supporting Information may be found in the online version of this article:

Supporting Information file includes one table and 14 figures providing velocity models for synthetic tests (Fig. S1), illustrations showing how the synthetic SRFs are constructed with our proposed data selection criteria for shorter time windows for the time-domain Wiener deconvolution (Figs S2 and S3), effect of using different data windowing and tapering length (Figs S4 and S5, respectively), effect of using various water levels in the alternative frequency-domain deconvolution (Figs S6 and S7), histograms of epicentral distance and event back-azimuth (Fig. S8) as well as source parameters (Fig. S9) against data selection criteria, and an alternative 50% threshold for six data selection criteria for the SRFs from station TJN (Figs S11 and S12) in addition to 25% threshold (Fig. S10). SRFs images with 25% threshold and a strong regularization (1% white noise) are shown in Figs S13 and S14.

Table S1. Velocity models.

Figure S1. Velocity models. The 1-D IASP91 model (Kennett & Engdahl 1991) is shown in black, and the L70 model is shown in red. The L70 model includes a 35 km thick high-velocity mantle lid with a 7.5% shear velocity increase below Moho, a low velocity zone with a 9% shear velocity reduction beneath 70 km depth, and a small 1.5% shear velocity increase beneath 120 km depth. See also Table S1.

Figure S2. Examples showing *P* coda waves and their influence on signal-generated noise in the SRF. Gray dashed boxes in panel (a) indicate how LQR is measured from the L- and Q-

component synthetic seismograms and how AMP is measured from synthetic SRF. Synthetic waveforms are computed from catalogued earthquake sources using the IASP91 (Kennett & Engdahl 1991) (a and c) and the L70 model (b and d). Time-domain Wiener deconvolution method is performed with the parent waveform time window of 10 s before and 15 s after the *S* arrival (black bar in a panel a). Note the amplitude scale of SRF in event 2 is higher than that in event 1.

Figure S3. Examples showing *P* coda waves and their influence on signal-generated noise in the SRF. Gray dashed boxes in panel (a) indicate how LQR is measured from the L- and Q-component synthetic seismograms and how AMP is measured from synthetic SRF. Synthetic waveforms are computed from catalogued earthquake sources using the IASP91 (Kennett & Engdahl 1991) (a and c) and the L70 model (b and d). Time-domain Wiener deconvolution method is performed with the parent waveform time window of 10 s before and 10 s after the *S* arrival (black bar in a panel a). Note the amplitude scale of SRF in event 2 is higher than that in event 1.

Figure S4. Images of synthetic SRFs for the case 1 from the L70 model as a function of the distance of 60°–85° with following six data selection criteria; (a) 25% lowest LQR, (b) 25% highest LQR, (c) 25% lowest AMP, (d) 25% highest AMP, (e) criterion by Wilson *et al.* (2006), and (f) 25% random data selection. The parent waveforms are windowed 10 s before and 15 s after the *S*-wave arrival and tapered with a 15% Hanning taper at both ends of the signal window. Dashed lines indicate phase arrival times predicted by the IASP91 model (Kennett & Engdahl 1991). The SRFs are plotted in the same way as Fig. 2.

Figure S5. Images of synthetic SRFs for the case 2 from the L70 model as a function of the epicentral distance of 60°–85° with six different data selection criteria. The parent waveforms are windowed 10 s before and 35 s after the *S*-wave arrival and tapered with a 5% Hanning taper at both ends of the signal window. See a caption of Fig. S4 for more detail.

Figure S6. Images of synthetic SRFs for the case 3 from the L70 model as a function of the epicentral distance of 60°–85° with six different data selection criteria. The parent waveforms are windowed 10 s before and 35 s after the *S*-wave arrival and tapered with a 15% Hanning taper at both ends of the signal window. The frequency-domain deconvolution is done with a water level of 0.05%. See a caption of Fig. S4 for more detail.

Figure S7. Images of synthetic SRFs for the case 4 from the L70 model as a function of the distance of 60°–85° with six different data selection criteria. The parent waveforms are windowed 10 s before and 35 s after the *S*-wave arrival and tapered with a 15% Hanning taper at both ends of the signal window. The frequency-domain deconvolution is done with a water level of 0.2%. See a caption of Fig. S4 for more detail.

Figure S8. Histograms of epicentral distance and back azimuth against six data selection criteria. LQR and AMP data selection criteria with a percentage threshold of 25% result in negligible data selection bias in back azimuthal and epicentral distance.

Figure S9. Histograms of earthquake source parameters (dip, strike and rake) against four data selection criteria; (a, e, f) 25% lowest LQR, (b, f, j) 25% highest LQR, (c, g, k) 25% lowest AMP, and (d, h, l) 25% highest AMP. LQR and AMP data selection criteria result in negligible data selection preference in source parameters.

Figure S10. Images of SRFs for station TJN as a function of the epicentral distance of 60°–85° with following six data selection criteria; (a) 25% lowest LQR, (b) 25% highest LQR, (c) 25% lowest AMP, (d) 25% highest AMP, (e) criterion by Wilson *et al*. (2006), and (f) 25% random data selection. The parent waveforms are windowed 10 s before and 35 s after the *S*-wave arrival and tapered with a 15% Hanning taper at both ends of the signal window. See a caption of Fig. S4 for more detail. See also Fig. 10 for the images of -80–80 s window.

Figure S11. Images of SRFs for station TJN as a function of the distance of 60°–85° with following six data selection criteria; (a) 50% lowest LQR, (b) 50% highest LQR, (c) 50% lowest AMP, (d) 50% highest AMP, (e) criterion by Wilson *et al*. (2006), and (f) 50% random data selection. The parent waveforms are windowed 10 s before and 35 s after the *S*-wave arrival and tapered with a 15% Hanning taper at both ends of the signal window. See a caption of Fig. S4 for more detail. See Fig. S12 for the images plotted for -30–30 s window.

Figure S12. Images of SRFs for station TJN as a function of the distance of 60°–85° with following six data selection criteria; (a) 50% lowest LQR, (b) 50% highest LQR, (c) 50% lowest AMP, (d) 50% highest AMP, (e) criterion by Wilson *et al*. (2006), and (f) 50% random data selection. The parent waveforms are windowed 10 s before and 35 s after the *S*-wave arrival and tapered with a 15% Hanning taper at both ends of the signal window. See a caption of Fig. S4 for more detail.

Figure S13. Images of SRFs for station TJN as a function of the distance of 60°–85° with following six data selection criteria; (a) 25% lowest LQR, (b) 25% highest LQR, (c) 25% lowest AMP, (d) 25% highest AMP, (e) criterion by Wilson *et al*. (2006), and (f) 25%

random data selection. The parent waveforms are windowed 10 s before and 35 s after the *S*-wave arrival and tapered with a 15% Hanning taper at both ends of the signal window. Time domain wiener deconvolution is done with a strong regularization of 1% white noise. See Fig. S14 for the images plotted for -30–30 s window.

Figure S14. Images of SRFs for station TJN as a function of the distance of 60°–85° with following six data selection criteria; (a) 25% lowest LQR, (b) 25% highest LQR, (c) 25% lowest AMP, (d) 25% highest AMP, (e) criterion by Wilson *et al*. (2006), and (f) 25% random data selection. The parent waveforms are windowed 10 s before and 35 s after the *S*-wave arrival and tapered with a 15% Hanning taper at both ends of the signal window. Time domain wiener deconvolution is done with a strong regularization of 1% white noise.

Geophysical International Journal

Data-oriented constraint on the interpretation of *S* receiver function and its application to observations of seismic discontinuities in the lithosphere-asthenosphere system

Xuzhang Shen[1], YoungHee Kim[2*], Teh-Ru Alex Song[3], and Hobin Lim[2]

1 Guangdong Provincial Key Laboratory of Geodynamics and Geohazards, School of Earth Sciences and Engineering, Sun Yat-Sen University, Guangzhou, 510275, China

2 School of Earth and Environmental Sciences, Seoul National University Seoul, 08826, Republic of Korea (younghkim@snu.ac.kr)

3 Seismological Laboratory, Department of Earth Sciences, University College London, WC1E 6BT, London, United Kingdom

Summary

This paper aims to improve the robustness of interpretation in the *S* receiver function (SRF), a technique commonly used to retrieve forward scattering of *S*-to-*P* converted waves (*Sdp*) originated from the lithosphere-asthenosphere system (LAS) beneath the stations. Although the SRF does not suffer interferences from backward scattering waves such as the first multiples from the Moho, one major drawback in the method is that *Sdp* phases can interfere with *P* coda waves and it is conceivable that these signal-generated noise may be misinterpreted as *Sdp* phase from the LAS beneath seismic stations. Through systematic analysis of full-waveform synthetics and SRFs from catalogued source parameters, we find that the strong *P* coda waves before the *S* wave in the longitudinal-component waveforms result in unwanted signal-generated noise before the *S* wave in the synthetic SRFs. If the mean amplitude of SRFs after the *S* wave is large, dubious signal-generated noise before the *S* arrival are strong as well. In this study, we honor the level of these unwanted signal-generated noise and devise data-oriented screening criteria to minimize the interference between *P* coda waves and genuine *S*-to-*P* converted waves. The first criterion is LQR, a direct measure of the amplitude ratio between longitudinal *P* coda waves and radial *S* wave in the waveform data. The second criterion is AMP, the amplitude of SRFs after the *S* arrival. We illustrate that these criteria effectively measure the energy level of mantle waves such as the *SP* wave. With synthetics and real data, we demonstrate the effectiveness of LQR and AMP criteria in minimizing these unwanted signal-generated noise in the stacked SRFs down to 1–2%, improving detection threshold and interpretation of *Sdp* phases from seismic discontinuities in the LAS.

Key words: Body waves; Structure of the Earth; Wave propagation, Wave scattering and diffraction; Coda waves

1 Introduction

Oceanic lithosphere is typically thought to be the outcome of melting of undepleted mantle and subsequent cooling, whereas continental lithosphere, especially beneath the cratons, is often considered as the result of large-scale plume melting, stacking oceanic lithospheres or/and arc collision (e.g. Lee *et al*. 2010). Small-scale convective instability, episodes of metasomatism and hydration, among other mechanisms, potentially facilitate the modification and disruption of oceanic and continental lithosphere. Unraveling robust seismic signature with the lithosphere-asthenosphere system (LAS) is crucial to understanding of the formation, modification and destruction of the plates and the formation of continents. For instance, the lithosphere-asthenosphere boundary (LAB), a mechanical boundary separating the rigid lithosphere and underlying viscous asthenosphere is thought to be the result of a simple thermal boundary due to long-term cooling. Seismic LAB from such a thermal boundary is considered smooth and gradual, where the velocity reduction with depth takes place over a transition thickness on the order of 50 km (Fischer *et al*. 2010). However, recent efforts have demonstrated that seismic LAB can be much sharper (e.g. Rychert *et al*. 2007; Kawakatsu *et al*. 2009; Tharimena *et al*. 2017). Beneath the continents and many localities in the oceans, seismic discontinuities have also been observed at depth ranges much shallower than expected, and the nature of such mid-lithospheric discontinuities (MLDs) remains elusive (e.g. Karato 2012; Schmerr 2012; Selway *et al*. 2015).

Therefore, it is clear that a robust and high-resolution seismic detection and characterization of LAB or/and MLDs can revolutionize our understandings of plate tectonics (e.g. Eaton *et al*. 2009; Fischer *et al*. 2010; Kawakatsu & Utada 2017). In the last decade, the depth and spatial resolution of the seismic discontinuities are greatly improved, thanks to the explosion of seismic data and progression of varieties of seismic techniques, including teleseismic *P*-to-*S* receiver function (PRF) (e.g. Langston 1977; Rondenay 2009) and *S*-to-*P*

receiver function (SRF) (e.g. Farra & Vinnik 2000), *ScS* reverberations (e.g. Bagley & Revenaugh 2008), and multiple *S*-wave triplications (e.g. Tan & Helmberger 2007) and underside *SS* precursors (e.g. Rychert & Shearer 2011; Schmerr 2012). Among these methods, PRF and SRF provide the highest resolution of seismic discontinuities in the LAS because of the use of relatively high-frequency waves (e.g. 0.1–1.0 Hz) in the analysis.

While the PRF and SRF methods can effectively detect converted phases (*Pds* or *Sdp,* where '*d*' marks the depth or location of the conversion) through source normalization (or deconvolution) and stacking, they are not without issues. For example, the PRF suffers interferences from backward scattering waves such as the first multiples from the Moho, making it difficult to identify converted-phase arrivals within the LAS. On the other hand, the SRF, by construction, separates the converted phases from the multiples (e.g. Ferra & Vinnik 2000), and it is preferable to identify robust signal from the LAS. However, one major drawback is that *Sdp* converted waves can be interfered by *P* coda waves, which consist of multiple mantle *P* waves (e.g. Wilson *et al*. 2006), multiples of reflections between the surface and the transition zone (e.g. Bock 1994) or/and *S*-to-*P* scattering waves within the crust and lithosphere between the source and the receiver (e.g. Vinnik & Romanowicz 1991). Depending on the strength of scatters as well as epicentral distance, azimuth, earthquake source depth, and source mechanisms, the amplitudes and timings of these *P* coda waves may vary and a significant level of wave energy preceding the *S*-wave arrival can be erroneously taken as *S*-to-*P* phases converted beneath the stations. Therefore, a robust identification and interpretation of *S*-to-*P* converted waves in the SRF are not necessarily trivial, and data selection criteria can become the key to provide a more robust determination of sharp features in the LAS.

The purpose of this paper is thus to introduce simple but effective screening criteria for the data selection and therefore removal of data or SRFs with strong unwanted signal-

generated noise. We will first briefly review data selection criteria established in the literatures (e.g. Kumar *et al*. 2005; Yuan *et al*. 2006; Wilson *et al*. 2006; Abt *et al*. 2010; Kind *et al*. 2015; Shen *et al*. 2017). To devise an objective criterion to minimize the interference from *P* coda waves, as a proof of concept, we first examine scenario of SRFs recorded in South Korea seismic network, sitting on a geologically stable continental platform (Fig. 1). Through systematic analysis of full-waveform synthetics and SRFs from catalogued teleseismic earthquakes in 2005–2015 (Takeuchi *et al*. 1996; Kawai *et al*. 2006), we demonstrate the usage and effectiveness of the new data screening and selection criteria against previous efforts (e.g. Wilson *et al*. 2006) with synthetics as well as observed SRFs in South Korea.

2 Construction of SRF and previous efforts in the data selection criteria

The calculation of SRF involves two important steps, that are (1) coordinate rotation, which isolates *Sdp* phase from the incident *S* wave, and (2) deconvolution, which removes source and propagation path effects (e.g. Farra & Vinnik 2000). Three-component north-east-vertical (N–E–Z) data are rotated to L–Q–T (or *P–SV–SH*) ray coordinate system (see also Rondenay 2009). While both of these coordinate systems are frequently implemented in past SRF studies (see review by Rondenay 2009; Kind *et al*. 2012), as demonstrated by Svenningsen *&* Jacobsen (2004) and discussed by Rondenay (2009), the difference of SRFs constructed in these two coordinate systems is minimum and much less than 1% (see Fig. 3 in Svenningsen *&* Jacobsen (2004)). Since the aim of this paper is to design the metrics to indicate the level of unwanted signal-generated noise prior to the *S* wave, we choose to discuss and illustrate the usage of our designed metrics in the L–Q–T system throughout this paper.

As the L component is dominated by the *P* wave, Q and T components mostly contain energies from *SV* and *SH* waves, respectively. SRFs are then computed by deconvolving the *S* waveform in the Q component from the corresponding L component, in either time domain or frequency domain. To improve the signal-to-noise ratio (SNR), SRFs are binned and stacked. Throughout the paper, we will illustrate the usage and performance of our data-oriented screening criteria with the time-domain Wiener deconvolution method (Robinson & Treitel 1967), whereas examples with the frequency-domain deconvolution of various water levels can be referred to the Supplementary Information.

Earlier works put emphasis on the selection of earthquakes in restricted epicentral distances or/and source depths (e.g. Wilson *et al*. 2006; Yuan *et al*. 2006). In an attempt to evaluate the robustness of the observed *Sdp* phases, Yuan *et al*. (2006) performed full waveform synthetics (Wang 1999) and suggested optimal epicentral distances of 55°−85° for the construction of SRF, which avoid post-critical incoming *S* wave. However, the synthetic waveforms only include downgoing waves and upgoing waves were excluded. Consequently, the influence of surface-reflected *P* waves on the *Sdp* detection cannot be evaluated. On the other hand, Wilson *et al*. (2006) conducted full waveform synthetics (Fuchs & Müeller 1971) and quantitatively measured the energy level before the *S* wave in the SRFs. They suggested a data selection criterion for the SRF at restricted epicentral distances of 60°–75° and source depths of 300 km or less.

The criterion by Wilson *et al*. (2006) was however based on synthetics from a single thrust-fault source mechanism and an one-dimensional (1-D) velocity model with a relatively thick crust of 70 km. Therefore, the established criterion needs not necessarily be the most general choice. As *P* coda waves can consist of multiple mantle *P* waves or/and *S*-to-*P* scattering waves within the crust and lithosphere between the source and the receiver, the amplitude and timing of these *P* coda waves not only depend on source depth (Wilson *et al*.

2006), but it may also depend on the strength of scatters and source-receiver geometry and source mechanisms, or effectively the radiation pattern. Nevertheless, these data selection criteria have been commonly used in the SRF analysis, sometimes with a minor adjustment on either the range of epicentral distance or/and source depth (e.g. Hansen *et al*. 2009; Abt *et al*. 2010; Ford *et al*. 2010; Lekic & Fischer 2014; Hopper & Fischer 2015).

To improve the robustness and interpretation of the SRF and establish a more general data selection scheme, our focus is to expand the work by Wilson *et al*. (2006) and establish data-oriented selection criteria. In particular, by either contrasting the energy level between the *S*-wave arrival in the Q-component waveform and *P* coda waves in the L-component waveform, or measuring the amplitude of the SRF after the *S* wave, we introduce more direct and general selection and screening criteria that do not necessarily rely on a specific choice of the epicentral distance or source parameters, but honor the level of unwanted signal-generated noise before the *S* wave.

3 Design and construction of new data selection criteria for the SRF

As discussed in previous sections, multiple mantle *P* waves or *S*-to-*P* scattering within the crust and mantle between the source and receiver (Vinnik & Romonowicz 1991; Bock 1994; Wilson *et al*. 2006) can form the *P* coda waves. Depending on the amplitude of these *P* coda waves preceding the *S*-wave arrival, they can interfere with converted waves, *Sdp*, from the LAS beneath seismic stations, or even being erroneously identified as *Sdp*. Depending upon the epicentral distance, source depth and mechanism, the level of interference can vary. In other words, the energy level of *P* coda waves can be large even for a shallow event. Since the effect of diverse source mechanism or radiation pattern on the excitation of these *P* coda waves was not explored by Wilson *et al*. (2006), we conduct a systematic investigation

through full waveform synthetics and examine the impact of realistic source mechanisms, or more importantly, the radiation pattern on the excitation and amplitude of *P* coda waves.

As a proof of concept, we consider observations of one station from the South Korea seismic network (Lim *et al.* 2018) and examine full waveform synthetics from earthquakes with magnitude larger than 5.5 between 2004 and 2013 from the global CMT catalogue (Dziewonski *et al.* 1981; Ekström *et al.* 2012), located at the distances of 60°–85° from the seismic network (Fig. 1). The event magnitude threshold of 5.5 allows detection of clear *S*-wave arrivals and identification of *SMp* arrivals from the Moho beneath the continental platform in South Korea. Since most stations generally contain quality waveform data from 200–400 earthquakes after data quality control and screening, we randomly select 300 earthquakes in our synthetic test. As expected in most realistic scenarios, synthetics data are predominantly from shallow events. Synthetic waveforms are computed with the Direct Solution Method (Takeuchi *et al*. 1996; Kawai *et al*. 2006) using the 1-D IASP91 model (Kennett & Engdahl 1991) as well as a modified IASP91 model (denoted as 'L70'), which includes a 35 km thick high-velocity mantle lid with a 7.5% shear velocity increase below Moho, a low velocity zone with a 9% shear velocity reduction beneath 70 km depth, and a small 1.5% shear velocity increase beneath 120 km depth (Fig. S1; Table S1).

To calculate synthetic SRFs, we first rotate synthetic waveforms with a time window of 100 s prior to and 100 s after the *S* wave to the radial-tangential-vertical (R–T–Z) system using the theoretical event back-azimuth. Theoretical incidence angle of the *S* wave computed from the IASP91 model is used to rotate waveforms into the ray coordinate system in the L–Q–T components (e.g. Rondenay 2009) before deconvolution (e.g. Kind *et al.* 2012; Shen *et al*. 2017). The waveforms in the Q component (e.g. the parent waveform) are windowed 10 s before and 35 s after the *S*-wave arrival and tapered with a 15% Hanning

taper at both ends of the signal window. The L- and Q-component waveforms are then deconvolved by the parent waveform through the time-domain Wiener deconvolution method, which involves spiking of the output time series with the parent waveform and construction of Wiener-filter time series (Robinson & Treitel 1967). Minimum regularization with a white noise of 0.01% is applied in the calculation. Such a time series is then convolved with L- and Q-component waveforms to obtain L- and Q-component SRFs, respectively. The resulting SRFs are bandpass filtered at 3–50 s and normalized by the spike in the Q-component at zero time. Hereafter, we will refer our discussion in the L-component SRFs.

3.1 Inspections of synthetic SRFs

Figs 2a and b display stacked synthetic SRF record sections, which consist of 300 individual SRFs, stacked with a 1°-distance bin and aligned along the *S* arrival at zero time. Synthetics are computed with the IASP91 model (Fig. 2a) and the L70 model (Fig. 2b). The converted waves from the Conrad (*SCp*) and the Moho (*SMp*) have a negative polarity and they arrive at about 4–5 s before the *S* wave (Fig. 2). Crustal multiples (e.g. *SCpPCP* and *SMpPMP*) and other mantle waves such as *SP*, *sSP, pSPPP, sSPPPP* and *pSPPPPP* arrive at about 5–60 s after the *S* wave (Fig. 2). Converted waves at the upper mantle seismic discontinuities from incident *ScS* and *SKS* waves (e.g. *ScS410p*, *ScS660p*, *SKS410p* and *SKS660p*) have a very different moveout from the *SMp* and they are less visible than those shown in Yuan *et al*. (2006). On the other hand, as pointed out by Wilson *et al*. (2006), we can observe spurious but consistent energies before the *SMp* arrival that are not associated with converted waves from local structure beneath the receivers. Therefore, it is important to set up a general data selection scheme to minimize these spurious arrivals.

After systematically inspecting synthetic waveforms and the resulting SRFs, we use Fig. 3 to illustrate the motivation of our designated data selection criteria. We consider two

earthquakes (events 1 and 2) such that their epicentral distances are comparable at ~67° and the SNR of the *S* waves in the Q component are also similar (Fig. 1a, red beachballs). However, regardless of the choice of IASP91 model or L70 model (Fig. S1), the *P* coda waves in the L-component waveforms are comparably stronger in event 2 than those in event 1, arguing the effect of radiation pattern on the amplitude of these *P* coda waves. When examining their SRFs, those from event 1 display clear *SMp* or/and *SLp* with otherwise weak energy prior to the *S* wave (Figs 3a and b). On the other hand, SRFs from event 2 display strong and spurious energy before and after the *S* wave (e.g. Figs 3c and d). It is noteworthy to emphasize that, as the deconvolution scheme, data windowing and tapering procedures are exactly the same between event 1 and event 2, strong spurious energy before the *S* wave in the SRF directly corroborates with strong *P* coda waves in the L-component waveform of event 2 (see also Figs S2 and S3 for the results with different windowing schemes). As noted earlier, it is conceivable that these dubious signals may be mistakenly interpreted as *Sdp* waves beneath seismic stations.

3.2 Measurement of LQR and AMP and construction of stacked SRFs

Motivated by observation, we devise measures of LQR, the amplitude ratio between L-component *P* coda waves and Q-component *S* waves, and AMP, the amplitude of SRFs after the *S*-wave arrival. We then systematically test how the LQR and AMP thresholds may be used to detect and retain robust *Sdp* waves while minimizing dubious energies in the SRFs (Fig. 3). Here, we define LQR as

$$\mathrm{LQR} = \mathrm{RMS}(\mathrm{L}[t_3\ t_4]) \,/\, \mathrm{Max}(\mathrm{Q}[t_1\ t_2]), \qquad (1)$$

where Max(Q[t_1 t_2]) measures the peak amplitude of the *S* wave in the Q-component data window defined by t_1 and t_2, and RMS(L[t_3 t_4]) measures the RMS amplitude of the *P* coda in the L-component time window defined by t_3 and t_4. On the other hand, the AMP is defined as

$$\mathrm{AMP} = \mathrm{RMS}(\mathrm{SRF}[t_5\ t_6]), \qquad (2)$$

where RMS(SRF[t_5 t_6]) measures the RMS amplitude of the SRF in the time window defined by t_5 and t_6 with respect to the *S* arrival. In the subsequent analysis and demonstration, we set t_1 = -5 s, t_2 = 10 s, t_3 = -60 s, t_4 = -20 s, t_5 = 20 s, and t_6 = 100 s. Note that the choice of t_3 and t_4 is such that they do not include potential *Sdp* arrivals in the LAS.

After measuring the LQR and AMP against all synthetic SRFs, we observe that SRFs with the lowest LQR typically fall in the distance range of 60°–66° and those with the lowest AMP are typically in the distance range of 70°–77°. However, to fully take advantage of the slant stack technique, it is important to ensure effective noise removal and to minimise data selection bias in epicentral distance. Therefore, it is more desirable that selected SRFs are evenly distributed within the entire distance range of 60°–85° and are not falling in a narrow distance range. Consequently, synthetic SRFs in each 1°-distance bin are first selected according to a designated data selection threshold and subsequently stacked. The error is then estimated by the bootstrap method (Efron & Tibshiran 1998).

In the following tests, we systematically examine how different LQR and AMP thresholds determine the quality of the stacked SRFs. To determine the effectiveness of each data selection criteria in mitigating signal-generated noise, we sum stacked SRFs of each 1°-distance bin and measure the RMS amplitude of the summed SRF before the *SMp* arrival (denoted as AMP1). The AMP1 is defined as

$$\mathrm{AMP1} = \mathrm{RMS}(\mathrm{SRF}[t_7\ t_8]), \qquad (3)$$

where RMS(SRF[t_7 t_8]) measures the RMS amplitude of the SRF in the time window defined by t_7 and t_8 with respect to the *S* arrival. Here, we set t_7 = -60 s and t_8 = -20 s.

3.3 Evaluating the efficacy of the LQR and AMP criteria

In order to investigate the efficacy of LQR and AMP criteria for the SRFs, we consider two principles to judge the quality of stacked SRFs. First, if the data selection criterion is effective, we expect that the signal-generated noise before the *S* arrival shall be minimized. This can be visually inspected and quantitatively examined through the measurement of AMP1. Second, if the data selection criterion is effective, the amplitude of stacked SRFs against epicentral distance should follow closely the theoretical *S*-to-*P* transmission coefficient (Aki & Richards 2002) with minimum perturbation.

3.3.1 Presence/absence of signal-generated noise before *S*-wave arrival

To highlight how the data selection criteria influence signal-generated noise, synthetic SRFs with 25% lowest and 25% highest LQR (or AMP) in each distance bin are selected and subsequently stacked. For comparison, we also present stacked SRFs with the criterion by Wilson *et al*. (2006) and those with 25% randomly selected SRFs. Stacked SRF images at 60°–85° from the IASP91 model (Kennett & Engdahl 1991) and L70 model (Fig. S1) are shown in Fig. 4, whereas the sum of stacked SRFs and their 95% confidence interval are displayed in Figs 5a and 5b, respectively. For comparisons, stacked SRF waveforms (Figs 5c–f) and stacked SRF images (Figs S4–7) with different parent window length (case 1; -10 s before and 15 s after the *S* wave), tapering (case 2; 5% Hanning taper), deconvolution scheme and regularization (cases 3 and 4; frequency-domain deconvolution with water level of 0.05% and 0.2%, respectively) are also presented for comparisons.

For the IASP91 model, the first signal before the *S* arrival is a negative *SMp* phase arriving at about 4 s before the *S* arrival (Figs 4a–f and 5a). While the *SMp* signal can be consistently detected with different data selection criteria (Figs 4a–f and 5a), the amplitudes of *SMp* with the highest LQR and AMP criteria are much stronger and more variable than those with the lowest LQR or AMP criteria (Fig. 5a). In particular, signals up to 6–8% with positive amplitude can be detected before the *SMp* at the 95% confidence level (Fig. 5a). However, these signals are dubious as they do not corroborate with the absence of any sharp velocity gradient below the Moho (Fig. S1). While the criterion by Wilson *et al*. (2006) does a better job in reducing the amplitude of these dubious signals down to 3–4% (Fig. 5a), the lowest LQR and AMP criteria appear to be the most effective, minimizing dubious arrivals at the amplitude level of 1–2%, typically insignificant at the 95% confidence level (Fig. 5a).

For the L70 model, we can observe a consistent, but positive signal arriving at about 9 s before the *S* arrival (Figs 4g–l and 5b). As expected, it is the *S*-to-*P* converted arrival (*SLp*) from the negative velocity discontinuity at the depth of 70 km (Fig. S1), Such a *SLp* signal has the same polarity and comparable strength as those used in previous studies to infer LAB or MLDs in the LAS (e.g., Eaton et al., 2009; Abt et al., 2010; Kumar et al., 2012; Shen et al., 2015; Shen et al., 2017). However, except the lowest LQR or AMP criteria, all other data selection criteria produce strong oscillations throughout the entire SRF stacks (Figs 4g–l), following slowness very similar to the *SP* wave. Even the *SLp* appears to be detected in this circumstance, the quality of the detection is low with incorrect amplitude and very large uncertainties (Fig. 5b). With the lowest LQR or AMP criteria, the *SLp* signal appears more robust with the smallest bootstrap uncertainties (Fig. 5b). It is evident that the signal-generated noise before the *S* arrival are much weaker in the stacked SRFs produced with the criteria of the lowest LQR (Figs 4g and 5b) or AMP (Figs 4i and 5b) than those produced

with the highest LQR (Figs 4h and 5b), the highest AMP (Figs 4j and 5b), the criterion by Wilson *et al.* (2006) (Figs 4k and 5b) or with random data selection (Figs 4l and 5b).

These observations can be concluded with alternative window length of the parent waveform (case 1; Figs 5c and S4), tapering (case 2; Figs 5d and S5) or deconvolution scheme (e.g. frequency-domain water-level deconvolution) with different regularization (cases 3 and 4; Figs. 5e, 5f, S6, and S7). Stacked SRFs produced with the criteria of the lowest LQR or AMP are stable, regardless specific choices of these data processing procedures. Evidently, stacked SRFs with other criteria vary more substantially with the choice of data processing routines. More critically, while a stronger regularization does minimize amplitude oscillation (e.g. case 4; Fig. 5f), strong signal-generated noise arriving before the *SLp* arrival remains.

To quantitatively assess the quality of stacked SRF and the effectiveness of data selection criteria in mitigating the signal-generated noise, we compute AMP1 to measure the RMS amplitude in the designated time window before the *S* arrival. We systematically select a subset of all synthetic SRFs by varying the percentage threshold (10–50%) of the lowest and highest LQR or AMP, generate the summed SRF and calculate AMP1. As shown in Fig. 6, the value of AMP1 generally decreases with increasing percentage threshold of six different criteria. At 25% threshold, AMP1 of the lowest LQR or AMP is lower than that of the highest LQR or AMP by more than a factor of 4 (Fig. 6). Also, at 25% threshold and higher, AMP1 of the lowest LQR or AMP is less than AMP1 of all SRFs (Fig. 6a). In particular, we find that the SRFs constructed with the lowest AMP generally display a lower level of AMP1, and the improvement is even more substantial for the synthetic SRFs from the L70 model (Fig. 6b). AMP1 of the lowest AMP for the L70 model is lower by a factor of 2 or less than that measured against the summed SRF of the entire SRF dataset (Fig. 6b).

In the case of random data selection, the value of AMP1 does not show appreciable difference with respect to the percentage threshold (Fig. 6), whereas the criterion of Wilson *et al*. (2006) does not seem to improve AMP1 upon those from random data selection (Fig. 6), which is not unexpected as synthetic data are predominantly from shallow events. In a way, even with a smaller volume of the entire synthetic SRFs (e.g., 25% or less), the lowest LQR or AMP criterion achieves a much lower AMP1 than that of Wilson *et al*. (2006)'s using 50% of the entire synthetic SRFs. Notably, depending on the exact data selection threshold, AMP1 with lowest LQR or lowest AMP criteria can be 20–50% lower than AMP1 of all events (Fig. 6).

3.3.2 Validating the amplitude of the *S*-to-*P* converted waves

To further verify the robustness of the converted phases beneath the receiver and assess the stability of the signal, we measure the amplitudes of *Sdp* (e.g. *SMp* and *SLp*) and compare them against the theoretical *S*-to-*P* transmission coefficient (Aki & Richards 2002). If the amplitudes of *Sdp* from the stacked SRFs follow closely to the theoretical transmission coefficients, we consider that the data selection criteria are effective in removing signal-generated noise and recovering a truthful detection. Fig. 7a shows distance-dependent amplitudes of *SMp* measured against stacked SRFs of six different criteria for the IASP91 model. On the other hand, Figs 7c and 7d show distance-dependent amplitudes of *SMp* and *SLp* measured against stacked SRFs of different criteria for the L70 model, respectively. Fig. 7b shows the amplitudes of the SRFs measured in the same time window as that used in Fig. 7d for comparison. Since we do not expect a truthful detection of *SLp* for the IASP91 model, the measurements are indicative of the level of signal-generated noise.

Typically, the highest LQR or AMP criterion results in unstable estimate of *SMp* amplitudes (e.g. Figs 4 and 5), and their amplitudes strongly deviate from the theoretical

predictions (Figs 7a and c). Stacked SRFs from the random data selection or from the criterion of Wilson *et al*. (2006) also suffer similar distortion, but to a less degree (Fig. 7). On the other hand, given the selection criteria of 25% lowest LQR or AMP, the amplitude of *SMp* follows closely to theoretical calculation against distance (Figs 7a and c). Similarly, the amplitude of *SLp* against distance generally follows theoretical prediction when the data selection criteria of 25% lowest LQR or AMP are implemented (Fig. 7d). Our results indicate that the lowest LQR or AMP is useful for detecting *SLp* phases and retaining their amplitudes by reducing the dubious signals before the *S* wave. We note that the average amplitude within the time window for expected *SLp* arrivals is typically on the order of 2% for the lowest LQR, and of ~1% for the lowest AMP (Fig. 7b). Therefore, we suggest 2% as the minimum amplitude threshold above which the robust identification of local *Sdp* converted waves within the LAS can be made and interpreted.

In summary, we find that the SRFs constructed with the lowest LQR or AMP generally display a lower level of spurious energy before the *S* wave while the SRFs with the highest LQR or AMP, as expected, displays a higher level of signal generated noise (Figs 4–7). The improvement appears more substantial in the case where synthetic SRFs are computed from the L70 model (Fig. 6b). While the calculation of SRF can be influenced by the choice of time window and tapering in the parent waveform as well as the deconvolution scheme (e.g. Lekic & Fischer 2017), the performance of LQR and AMP data selection criteria does not depend on such specific choices. This characteristic makes the LQR and AMP very desirable since stacked SRFs with low LQR and low AMP are always very stable.

3.3.3 The sources of *P* coda waves?

To investigate the source of these *P* coda waves, we first examine if the attributes such as LQR or AMP depend on epicentral distance, event back azimuth or source

parameters. However, we do not observe any obvious selection bias in event epicentral distance or back azimuth against the criteria such as LQR and AMP (Fig. S8), nor do we find dependence of LQR or AMP on earthquake source mechanism (Fig. S9), suggesting that LQR and AMP, or the level of *P* coda waves, are predominantly dictated by the radiation pattern. In this regard, while we do not specifically include *SV/SH* amplitude ratio in the data selection criteria, high LQR or AMP criterion more often corresponds to data with a low *SV/SH* ratio (< 1) and low LQR or AMP typically corresponds to data with a high *SV/SH* ratio (> 1) (Fig. 8).

It has been argued by Wilson *et al*. (2006) that *P*-coda waves can come from multiples such as *pPPP*, *pPPPP* or/and *sPPPP* from deep events (> 300 km) and they may interfere with *Sdp* phases. However, for most practical analysis on the LAS, only those from really deep events of 450 km or deeper may directly interfere with *Sdp* from the LAS since these multiples, in most instances, arrive at least 1–2 minutes before the *S* arrival. Similar lines of arguments have been also pointed out by Vinnik & Romanowicz (1991). This assertion can be supported by the fact that *P* radiation patterns computed with the slowness such as *pPPPP* wave do not distinguish against LQR or AMP (Fig. 9). This is also consistent with our observation that, when shallow events dominate the synthetic dataset, Wilson *et al*. (2006)'s criterion does not necessarily outperform data selection scheme of random choice (Figs 5b–f; see also Figs S4–7).

As shown in Figs 4g–l, signal-generated noise before the *S* arrival appear to follow very similar slowness as those mantle waves such as *SP*, *sSP*, *sSPPP,* and *sSPPPP*, apparently forming precursors of these mantle waves and interfering with *Sdp* phases in the LAS. It is conceivable that energies prior to the *S* wave in the stacked SRF are likely to be scattering waves such as *S•P* and *SP•P*, where *S•P* denotes *S*-to-*P* scattering wave from the free surface

and *SP•P* denotes *SP*-to-*P* scattering wave from the scatter in the crust (Vinnik 1981; Vinnik & Romanowicz 1991). Depending on the lead time of scattering waves with respect to the *S* wave, the area of scattering is expected to be at least 25° from the receiver, and typically in the range of 30°–40° from the receiver (see Fig. 8a of Vinnik & Romanowicz (1991)), with the raypaths of *S* and *P* waves in the *S•P* (or *SP•P*) arriving in different vertical planes. As our wave propagation simulation is done with a laterally homogeneous and spherically symmetric earth model (Kawai *et al*. 2006) with a finite duration *S* wave, spherical waves propagating off the vertical plane defined by the source and receiver likely result in scattering waves such as *S•P*.

If *S•P* or/and *SP•P* scattering waves are indeed the cause of these signal-generated noise observed in SRFs, the *SV* radiation pattern in the area of scattering will directly control the amplitude of *S•P* and *SP•P* scattering waves (Vinnik & Romanowicz 1991). To validate this, we assume that the scattering area is near the surface reflection point of *SP* wave and compute *SV* radiation pattern with the slowness of *SP* wave in our synthetic dataset. As shown in Fig. 10, the *SV* radiation patterns against the lowest LQR and AMP criteria are generally much weaker than those against the highest LQR and AMP criteria. Effectively, LQR and AMP criteria help select data with weakest *SV* radiation pattern in the scattering area. Following the same line of reasoning, it is conceivable that *S•P* scattering waves can come from internal boundaries such as the Moho. While a more elaborated investigation should be done in the future, this is consistent with our simulation that signal-generated noise in SRF are much stronger in the L70 model, which includes a larger velocity contrast across the Moho than the IASP91 model as well as an additional velocity reduction at 70 km depth (Fig. S1).

Evidently, there is no lateral variation in surface topography, internal boundary or velocity in our simulation, and it is difficult to precisely estimate the scattering potential without invoking 2-D or 3-D full waveform modelling. It is also possible that signal-generated noise in 2-D or 3-D models are less coherent and do not add constructively. However, our data-oriented screening criteria such as LQR or AMP are designed to honor the data and provide direct and straightforward attributes to measure the level of these spurious energies. With lowest LQR or/and AMP, SRFs with strong signal-generated noise are effectively removed, improving the quality of stacked SRF and the detection of true *Sdp* arrivals in the LAS beneath seismic stations.

4 Application to South Korea seismic data: detection and characterization of seismic discontinuities in the LAS

Our synthetic tests have demonstrated that the effectiveness of LQR and AMP could serve as general data selection criteria for the construction of SRF. Here we apply these new data selection criteria to the dataset recorded by South Korea seismic network (Fig. 1) (Lim *et al*. 2018) and illustrate its effectiveness in real datasets. We select earthquake magnitudes greater than 5.5 within the epicentral distance range of 60°–85° from the seismic network. To construct the SRF, we follow exactly the same scheme detailed in the synthetic test in Section 3, but highlight a few key additional steps here to screen noisy data. First, when rotating three-component waveforms into L-Q-T coordinate system, the incidence angle of the incoming *S* wave is determined by maximizing the *SV*-wave energy on the Q component within the time window spanning ±2 s on either side of the theoretical *S*-wave onset. If the difference between the observed incidence angle and the predicted one (from IASP91) exceeds 25°, the waveforms are rejected. Secondly, data are also removed if the SNR of the *S*

wave in the Q component is less than 5. Thirdly, if the peak SRF amplitude in the L component is larger than 0.5 or if the mean amplitude of the SRF in the L component is larger than 50% of its peak amplitude, such SRFs are apparently oscillatory throughout the entire time window and they are also rejected.

As an example, we examine stacked SRFs at station TJN in South Korea seismic network (Fig. 1b) in detail. We process waveform data from 917 events in January 2005–January 2015 (Lim *et al*. 2018) and, after preliminary data quality control detailed earlier, 316 SRFs are retained and they are filtered at 3–50 s before subsequent data selection analysis. Here we measure LQR and AMP against the observed SRFs exactly the same way as discussed in Section 3. In general, the lowest LQR and AMP against the observed SRFs are typically higher than that against synthetics SRFs because of noise. With the nominal percentage threshold of 25%, we finally retain about 80 SRFs.

To illustrate how the stability of the SRF and detection of *SMp* and *SLp* depend on the data selection criteria, Fig. 11 (and Fig. S10) displays stacked SRF images constructed with the same six different data-selection criteria as discussed in the synthetic test in Section 3 (e.g. Fig. 4), With the lowest LQR or AMP criterion (Figs 11a and c), we can reasonably track a consistent signal with negative amplitude with respect to epicentral distance, arriving about 4 s before the *S* arrival, presumably *Sdp* from the Moho (*SMp*). However, it is less trivial to track *SMp* in stacked SRF image with the Wilson *et al*. (2006)'s criterion (Fig. 11e) or random selection criterion (Fig. 11f), and very difficult to do so against those constructed with the highest LQR or AMP criterion (Figs 11b and d). These observations can also be made against stacked SRF images using a stronger regularization of 1% white noise (Figs S13 and S14).

Stacking the SRFs shown in Fig. 11, Figs 12a and b displays summed SRF waveforms and their bootstrapped uncertainties against the six different data-selection criteria and data selection threshold of 25% and 50%, respectively. Again, using the lowest LQR, AMP or Wilson *et al*. (2006)'s criterion, detection of *SMp* can be made at the 95% confidence level (Fig. 12). With the highest LQR or AMP criterion, the *SMp* can be barely detected at the 95% confidence level with large uncertainties (Fig. 12a and b). Even with a stronger regularisation (1% white noise), *SMp* still possesses large uncertainties (Fig. 12c). It is important to note that the uncertainties of SRF with low LQR and AMP are much smaller than those with high LQR or AMP or random selection (Fig. 12). In principle, a consistent detection of *SMp* with small amplitude uncertainties serves as a very good indication on the quality of stacked SRF. Furthermore, with the lowest LQR or AMP criterion, a positive signal arriving at about 8 s before the *S* arrival, possibly *SLp* from the LAS, can be detected at 95% confidence level (Fig. 12), whereas such a *SLp* arrival cannot be detected otherwise with statistical significance (Fig. 12). We note that the amplitude of detected *SLp* is about 5–7%, considerably exceeding the 1–2% amplitude threshold for robust *SLp* detection with the lowest LQR or AMP criterion (e.g. Figs 4 and 5b).

Considering three data-selection criteria such as the lowest LQR, AMP and Wilson *et al*. (2006), Fig. 13 further examines distance-dependent amplitudes of detected *SMp* and *SLp* and they are compared against theoretical *S*-to-*P* transmission coefficient (Aki & Richards 2002) from the L70 model (Fig. S1). Here we do not seek an optimal fit to the data, but simply show if the amplitude measurements in general follow the theoretical trend against epicentral distance. While there are still substantial amplitude fluctuations with respect to theoretical prediction against epicentral distance, in this particular example at station TJN, measurements from the lowest AMP criterion follows closest to the theoretical trend,

regardless the degree of regularization (Figs 13a and b vs. Figs 13c and d). As expected, the amplitude of *SMp* and *SLp* is notably modulated by the degree of regularization.

At least locally beneath the station TJN, a relatively sharp boundary with a negative velocity gradient is robustly identified in the LAS beneath the old Korea craton (Lee *et al*. 1998). While the exact nature and spatial extent of such a boundary deserves further analysis and discussion, it is beyond the scope of this paper and we will detail the findings beneath the entire Korea network in a subsequent paper. Also, another key potential source of contamination on SRFs is scattering from laterally-varying structure (Lekic & Fischer 2017).

Lastly, Fig. 14 displays AMP1 against data-selection percentage threshold for six different criteria. Similar to what we observe in the synthetics (Fig. 6), the results from real data analysis at station TJN also show that not only AMP1 decreases with increasing percentage threshold, but the lowest LQR or AMP criterion gives the lowest AMP1 than Wilson *et al*. (2006) or the random data selection does (Fig. 14), compatible with synthetic test in Section 3 (Fig. 6). Despite the criterion of Wilson *et al*. (2006) restrains SRFs within 60°–75° from shallow events, the lowest LQR or AMP criterion does concern SRFs across the entire distance range of 60°–85°, including a few SRFs from deep earthquakes as well. Furthermore, since the level of random noise reduction is proportional to the square-root of SRF number in the stacks, there is a trade-off between eliminating random noise and signal-generated noise. While random noise can be reduced by stacking, it is not the case for signal-generated noise. In comparison to the cases shown in Figs 11 and 12, while we can still detect *SMp* and *SLp* at 95% confidence level with a higher percentage threshold of 50%, the uncertainty of SRF amplitude does not decrease as expected for random noise (Figs S11 and S12). By inspection, if N is the data selection percentage threshold, multiplying AMP1 in Fig. 6 (noise free) with the square root of 100/N generally reproduces the pattern of AMP1 shown

in Fig. 14. This can be useful in the discussion on how to properly select N against random noise with respect to data quality and noise level.

In the case of our test, permanent station TJN provides about 300 quality data over 10 years after data prescreening. As we present the result with 25% selection threshold (or ~75 traces) for the detection of the *SLp* phase (Figs 11–13), we find a 15% selection threshold (or ~45 traces) with the low AMP criteria can still provide consistent SRF and *SLp* detection. Concerning typical PASSCAL experiments or temporal arrays over a 2-year period, depending on the aperture of the array, the number of stations, background noise level and the scale of lateral heterogeneity in the LAS, it is conceivable that a network of 5 stations can record 45 traces with low LQR and produce reasonably robust SRF stacks.

As evident in the synthetic test and real data analysis, high SNR of the *S* wave in the Q-component seismogram by itself does not necessarily warrant the quality of stacked SRFs. The data selection criterion proposed by Wilson *et al*. (2006) is favorable for a specific focal mechanism, but it is not necessarily a general scheme that takes into account the effect of radiation pattern on the excitation of mantle *P* coda waves or/and scattering waves between the source and receiver in the L-component seismogram. In this study, the LQR criterion, by design, makes a direct amplitude measurement of the scattering wave in the L component and contrasts it against the amplitude of the *S* wave in the Q component. Obviously, the application of LQR criteria in real data analysis slightly depends on the choice of measurement time window, which may be adapted. Alternatively, the AMP data selection criterion makes a direct assessment on the amplitude of *SP*, *sSP* and other related multiples in the SRF, making it an ideal proxy to indicate the strength of scattering waves away from the receiver side (e.g., Vinnik & Romonowicz 1991). Finally, these data selection criteria can be easily adapted to a different coordinate system (e.g., *P-SV-SH*) when desired.

5 Conclusions

Teleseismic scattered waves such as *S*-to-*P* converted phases (*Sdp*) provide enhanced sensitivity to localized velocity gradients across the lithospheric discontinuities. In this study, through systematic analysis of full-waveform synthetic waveforms and SRFs from catalogued earthquake focal mechanism and depth, we find that the strong *P* coda waves before the *S* wave recorded in the L component could result in the dubious *Sdp* phases in the synthetic SRFs before the *S* arrival. Furthermore, if the mean amplitude of SRFs after the *S* wave is large, dubious signals of SRFs before the *S* arrival become strong as well. Such signal-generated noise before the *S* arrival can be mistakenly interpreted as *Sdp* phase derived from lithosphere-asthenosphere system (LAS) beneath seismic stations.

To minimize the interference of *P* coda waves on *Sdp* phases in the LAS, we devise data-oriented criteria such as LQR, the amplitude ratio between *P* coda waves of the L-component waveform and the *S* wave of the Q-component waveform, and AMP, the amplitude of SRFs after the *S* arrival. These screening criteria provide a direct and straightforward attribute to measure and indicate the level of spurious energies before the *S* arrival in the SRF. With low LQR or AMP, regardless of the choice of deconvolution scheme, tapering or/and data windowing, unwanted signal-generated noise are largely removed, which improves the detection and quality of locally converted *Sdp* in the LAS. With the criteria such as the lowest LQR or AMP, the minimum amplitude threshold above which robust *SLp* can be detected is reduced down to about 1–2%, smaller than the amplitude threshold of 3–4% by the criterion of Wilson *et al*. (2006). The effectiveness of these criteria largely manifests the amplitude of *SP* wave as well as the control of *SV* radiation pattern in the scattering area on the amplitude of signal-generated noise due to *S*-to-*P* scattering (Vinnik & Romanowicz 1991). Applying the newly designed selection criteria to real data in the South Korea seismic

network, we demonstrate that the lowest LQR or AMP criterion provides robust detection of *SLp* beneath the test station TJN, offering a great potential to better characterize seismic discontinuities in the LAS.

Acknowledgements

Authors thank R. Kind (GFZ, Potsdam) for discussions. X. Shen acknowledges the National Natural Science Foundation of China (Grant 41874052 and 41574077), and National Key Research and Development Program of China (2017YFC1500100). Y. Kim and H. Lim acknowledge National Research Foundation of Korea Grant funded by the Korean Government (NRF-2014S1A2A2027609), and Korea Meteorological Administration Research and Development Program under Grant KMI 2018-02910. T.-R. A. Song acknowledges the support by the Natural Environment Research Council, UK (NE/P001378/1). Synthetic waveforms are computed using the high-performance computation facility, GRACE, at University College London. Receiver functions are computed with the codes provided by L. Zhu (Saint Louis University) (http://www.eas.slu.edu/People/LZhu/home.html). Some figures were plotted with Generic Mapping Tools (Wessel & Smith 1995). Lastly, authors thank the Editor A. Morelli, W. Geissler and an anonymous reviewer who helped improve this paper.

References

Abt, D. L., Fischer, K. M., French, S. W., Ford, H., Yuan, A. H. & Romanowicz, B., 2010. North American lithospheric discontinuity structure imaged by Ps and Sp receiver functions, *Journal of Geophysical Research: Solid Earth*, ***115***(B9), https://doi.org/10.1029/2009JB006914.

Aki, K. & Richards, P.G., 2002. Quantitative Seismology, 2nd Ed. *University Science Books*, ISBN 0-935702-96-2.

Bagley, B. & Revenaugh, J., 2008. Upper mantle seismic shear discontinuities of the Pacific, *Journal of Geophysical Research: Solid Earth*, ***113***(B12), https://doi.org/10.1029/2008JB005692.

Bock, B., 1994. Multiples as precursors to S, SKS and ScS, *Geophysical Journal International*, ***119***, 421–427.

Dziewonski, A., Chou, T. A. & Woodhouse, J., 1981. Determination of earthquake source parameters from waveform data for studies of global and regional seismicity, *Journal of Geophysical Research: Solid Earth*, ***86***(B4), 2825–2852, https://doi.org/10.1029/JB086iB04p02825.

Eaton, D. W., Darbyshire, F., Evans, R. L., Grütter, H., Jones, A. G. & Yuan, X., 2009. The elusive lithosphere–asthenosphere boundary (LAB) beneath cratons, *Lithos*, ***109***(1–2), 1–22, https://doi.org/10.1016/j.lithos.2008.05.009.

Efron, B. & Tibshirani, R., 1998. The problem of regions, *Annals of Statistics*, 1687–1718.

Ekström, G., Nettles, M. & Dziewoński, A., 2012. The global CMT project 2004–2010: Centroid-moment tensors for 13,017 earthquakes, *Physics of the Earth and Planetary Interiors*, ***200***, 1–9, https://doi.org/10.1016/j.pepi.2012.04.002.

Farra, V. & Vinnik, L., 2000. Upper mantle stratification by P and S receiver functions, *Geophysical Journal International*, ***141***(3), 699–712, https://doi.org/10.1046/j.1365-246x.2000.00118.x.

Fischer, K. M., Ford, H. A., Abt, D. L. & Rychert, C. A., 2010. The lithosphere-asthenosphere boundary, *Annual Review of Earth and Planetary Sciences*, ***38***, 551–575, https://doi.org/10.1146/annurev-earth-040809-152438.

Ford, H. A., Fischer, K. M., Abt, D. L., Rychert, C. A. & Elkins-Tanton, L. T., 2010. The lithosphere–asthenosphere boundary and cratonic lithospheric layering beneath Australia from Sp wave imaging. *Earth and Planetary Science Letters*, ***300***(3–4), 299–310. doi:10.1016/j.epsl.2010.10.007.

Fuchs, K. & Müller, G., 1971. Computation of synthetic seismograms with the reflectivity method and comparison with observations, *Geophysical Journal International*, ***23***(4), 417–433, https://doi.org/10.1111/j.1365-246X.1971.tb01834.x.

Hansen, S. E., Nyblade, A. N., Julia, J., Dirks, P. H. G. M. & Durrheim, R. J., 2009. Upper-mantle low-velocity zone structure beneath the Kaapvaal craton from S-wave receiver functions, *Geophysical Journal International*, ***178***(2), 1021–1027, https://doi.org/10.1111/j.1365-246X.2009.04178.x.

Hopper, E. & Fischer, K. M., 2015. The meaning of midlithospheric discontinuties: A case study in the northern US craton, *Geochemistry, Geophysics, Geosystems*, ***16***(12), 4057–4083, https://doi.org/10.1002/2015GC006030.

Karato, S.-i., 2012. On the origin of the asthenosphere, *Earth and Planetary Science Letters*, ***321***, 95–103, https://doi.org/10.1016/j.epsl.2012.01.001.

Kawai, K., Takeuchi, N. & Geller, R. J., 2006. Complete synthetic seismograms up to 2 Hz for transversely isotropic spherically symmetric media, *Geophysical Journal International*, ***164***(2), 411–424, https://doi.org/10.1111/j.1365-246X.2005.02829.x.

Kawakatsu, H. & Utada, H., 2017. Seismic and electrical signatures of the lithosphere–asthenosphere system of the normal oceanic mantle, *Annual Review of Earth and Planetary Sciences*, ***45***, 139–167, https://doi.org/10.1146/annurev-earth-063016-020319.

Kawakatsu, H., Kumar, P., Takei, Y., Shinohara, M., Kanazawa, T., Araki, E. & Suyehiro, K., 2009. Seismic evidence for sharp lithosphere-asthenosphere boundaries of oceanic plates, *Science*, ***324***(5926), 499–502, https://doi.org/10.1126/science.1169499.

Kennett, B. & Engdahl, E., 1991. Traveltimes for global earthquake location and phase identification, *Geophysical Journal International*, ***105***(2), 429–465, https://doi.org/10.1111/j.1365-246X.1991.tb06724.x.

Kind, R., Yuan, X., & Kumar, P., 2012. Seismic receiver functions and the lithosphere-asthenosphere boundary, Tectonophysics, **536–537**, 25–43, doi:10.1016/j.tecto.2012.03.005, 2012.

Kind, R., Yuan, X., Mechie, J. & Sodoudi, F., 2015. Structure of the upper mantle in the north-western and central United States from USArray S-receiver functions, *Solid Earth*, ***6***(3), 957.

Kumar, P., Yuan, X., Kind, R. & Mechie, J., 2012. The lithosphere-asthenosphere boundary observed with USArray receiver functions, *Solid Earth*, ***3***(1), 149.

Kumar, P., Kind, R., Hanka, W., Wylegalla, K., Reigber, C., Yuan, X., Woelbern, I., Schwintzer, P., Fleming, K. & Dahl-Jensen, T., 2005. The lithosphere–asthenosphere boundary in the North-West Atlantic region, *Earth and Planetary Science Letters*, ***236***(1–2), 249–257, https://doi.org/doi.org/10.1016/j.epsl.2005.05.029.

Langston, C. A., 1977. Corvallis, Oregon, crustal and upper mantle receiver structure from teleseismic P and S waves, *Bulletin of the Seismological Society of America*, ***67***(3), 713–724.

Lee, C.-T. A., Luffi, P. & Chin, E. J., 2011. Building and destroying continental mantle, *Annual Review of Earth and Planetary Sciences*, ***39***, 59–90, https://doi.org/10.1146/annurev-earth-040610-133505.

Lee, K.-S., Chang, H.-W. & Park, K.-H., 1998. Neoproterozoic bimodal volcanism in the central Ogcheon belt, Korea: age and tectonic implication. *Precambrian Research*, ***89***, 47–57.

Lekic, V. & Fischer, K. M., 2014. Contrasting lithospheric signatures across the western United States revealed by Sp receiver functions, *Earth and Planetary Science Letters*, ***402***, 90–98, https://doi.org/10.1146/j.epsl.2013.11.026.

Lekic, V. & Fischer, K. M., 2017. Interpreting spatially stacked Sp receiver functions, *Geophysical Journal International*, ***210***(2), 874–886, https://doi.org/10.1093/gji/ggx206.

Lim, H., Kim, Y., Song, T.-R. A. & Shen, X., 2018. Measurement of seismometer orientation using the tangential P-wave receiver function based on harmonic decomposition, *Geophysical Journal International*, ***212***(3), 1747–1765, https://doi.org/10.1093/gji/ggx515.

Nettles, M. & Dziewoński, A. M., 2008. Radially anisotropic shear velocity structure of the upper mantle globally and beneath North America, *Journal of Geophysical Research: Solid Earth*, ***113***(B2), https://doi.org/10.1029/2006JB004819.

Robinson, E. A. & Treitel, S., 1967. Principles of digital wiener filtering, *Geophysical Prospecting*, ***15***(3), 311–332, https://doi.org/10.1111/j.1365-2478.1967.tb01793.x.

Rondenay, S., 2009. Upper mantle imaging with array recordings of converted and scattered teleseismic waves, *Surveys in Geophysics*, ***30***(4–5), 377–405, https://doi.org/10.1007/s10712-009-9071-5.

Rychert, C. A. & Shearer, P. M., 2011. Imaging the lithosphere-asthenosphere boundary beneath the Pacific using SS waveform modeling, *Journal of Geophysical Research: Solid Earth*, ***116***(B7), https://doi.org/10.1029/2010JB008070.

Rychert, C. A., Rondenay, S. & Fischer, K. M., 2007. P-to-S and S-to-P imaging of a sharp lithosphere-asthenosphere boundary beneath eastern North America, *Journal of Geophysical Research: Solid Earth*, ***112***(B8), https://doi.org/10.1029/2006JB004619.

Schmerr, N., 2012. The Gutenberg discontinuity: Melt at the lithosphere-asthenosphere boundary, *Science*, ***335***(6075), 1480–1483, https://doi.org/10.1126/science.1215433.

Selway, K., Ford, H. & Kelemen, P., 2015. The seismic mid-lithosphere discontinuity, *Earth and Planetary Science Letters*, ***414***, 45–57, https://doi.org/10.1016/j.epsl.2014.12.029.

Shen, X., Yuan, X. & Ren, J., 2015. Anisotropic low-velocity lower crust beneath the northeastern margin of Tibetan Plateau: Evidence for crustal channel flow, *Geochemistry, Geophysics, Geosystems*, ***16***(12), 4223–4236, https://doi.org/10.1002/2015GC005952.

Shen, X., Liu, M., Gao, Y., Wang, W., Shi, Y., An, M., Zhang, Y. & Liu, X., 2017. Lithospheric structure across the northeastern margin of the Tibetan Plateau: Implications for the plateau's lateral growth, *Earth and Planetary Science Letters*, ***459***, 80–92, https://doi.org/10.1016/j.epsl.2016.11.027

Svenningsen, L. & Jacobsen, B. H., 2004. Comment on "Improved inversion for seismic structure using transformed, S-wavevector receiver functions: Removing the effect of the free surface" by Anya Reading, Brian Kennett, and Malcolm Sambridge, *Geophysical Research Letters*, **31**(L24609), doi:10.1029/2004GL021413.

Takeuchi, N., Geller, R. J. & Cummins, P. R., 1996. Highly accurate P-SV complete synthetic seismograms using modified DSM operators, *Geophysical Research Letters*, ***23***(10), 1175–1178, https://doi.org/10.1029/96GL00973.

Tan, Y. & Helmberger, D. V., 2007. Trans-Pacific upper mantle shear velocity structure, *Journal of Geophysical Research: Solid Earth*, ***112***(B8), https://doi.org/10.1029/2006JB004853.

Tharimena, S., Rychert, C., Harmon, N. & White, P., 2017. Imaging Pacific lithosphere seismic discontinuities – Insights from SS Precursor modeling. *Journal of Geophysical Research: Solid Earth*, ***122***(3), 2131–2152. doi:10.1002/2016JB013526.

Vinnik, L. P., 1981. Evaluation of the effective cross-section of scattering in the lithosphere, *Physics of the Earth Planetary Interiors*, ***26***, 268-284.

Vinnik, L. P. & Romanowicz, B. A., 1991. Origin of precursors to teleseismic S waves, *Bulletin of the Seismological Society of America*, ***81***(4), 1216–1230.

Wang, R., 1999. A simple orthonormalization method for stable and efficient computation of Green's functions, *Bulletin of the Seismological Society of America*, ***89***(3), 733–741.

Wessel, P., & Smith, W. H., 1995. New version of the generic mapping tools: Eos, Transactions, *American Geophysical Union*, ***76***, 326–329, https://doi.org/10.1029/95EO00198.

Wilson, D. C., Angus, D., Ni, J. F. & Grand, S. P., 2006. Constraints on the interpretation of S-to-P receiver functions, *Geophysical Journal International*, ***165***(3), 969–980, https://doi.org/10.1111/j.1365-246X.2006.02981.x.

Yuan, X., Kind, R., Li, X. & Wang, R., 2006. The S receiver functions: synthetics and data example, *Geophysical Journal International*, ***165***(2), 555–564, https://doi.org/10.1111/j.1365-246X.2006.02885.x.

Figures

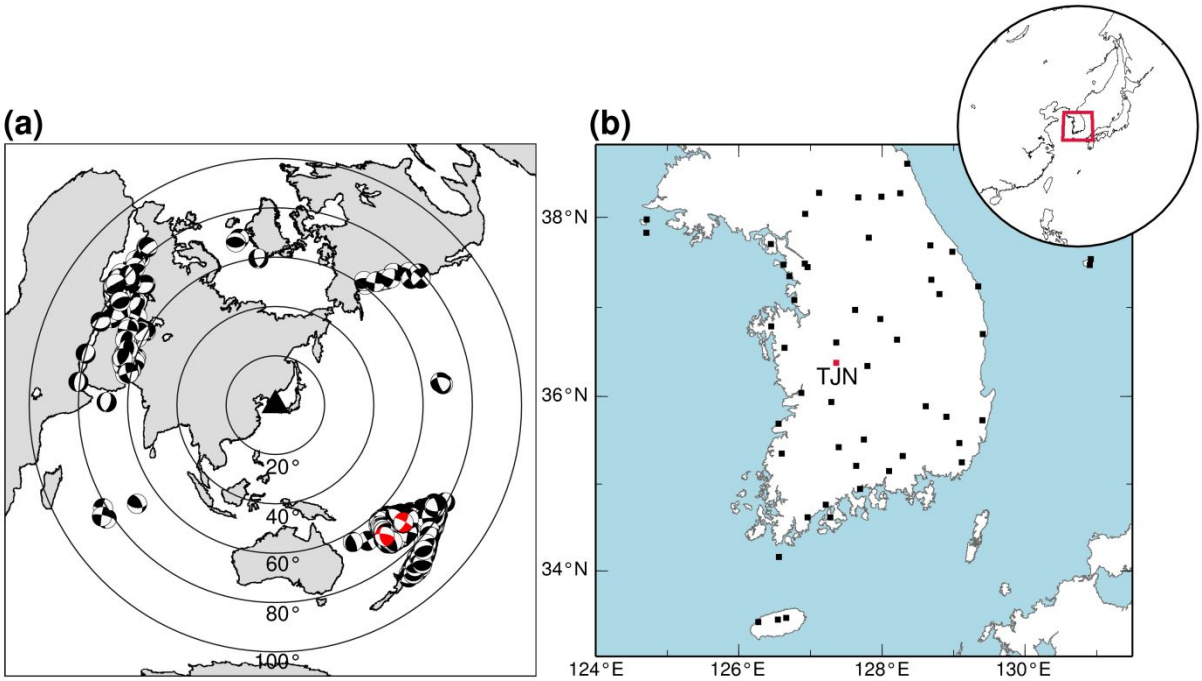

Figure 1. Distribution of earthquakes with magnitude greater than 5.5 and South Korea seismic network. (a) Distribution of earthquakes within the epicentral distances of 60°–85° from the center of the Korean seismic network (black triangle). The Centroid Moment Tensor (CMT) solutions of the events are from Dziewonski *et al*. (1981) and Ekstrom *et al*. (2012). Two earthquakes for synthetics in Fig. 3 are highlighted in red. (b) South Korea seismic network. Broadband seismic stations are shown in black squares, and the only station is labelled with the station ID (TJN).

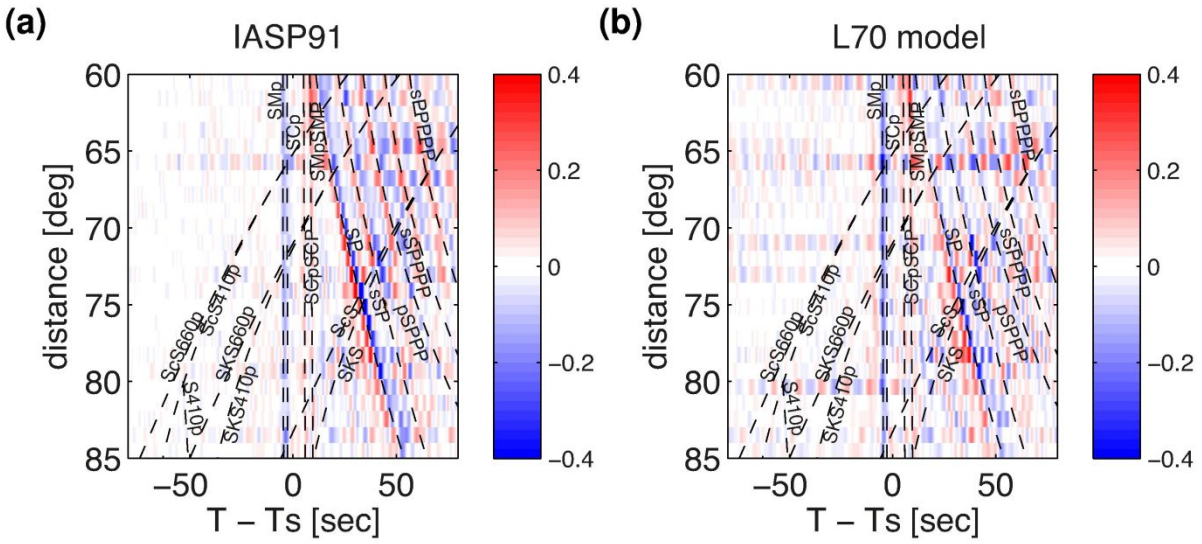

Figure 2. Stacks of 300 synthetic SRFs as a function of the epicentral distance of 60°–85°. The SRFs are binned with a distance of a 1° window and stacked, and their amplitudes are displayed in blue-to-red color. Theoretical phase arrival times from the IASP91 model (Kennett & Engdahl 1991) are marked as dashed lines with phase names labeled. (a) Synthetic SRFs calculated from the IASP91 model (Kennett & Engdahl 1991). (b) Synthetic SRFs from L70 model (Fig. S1).

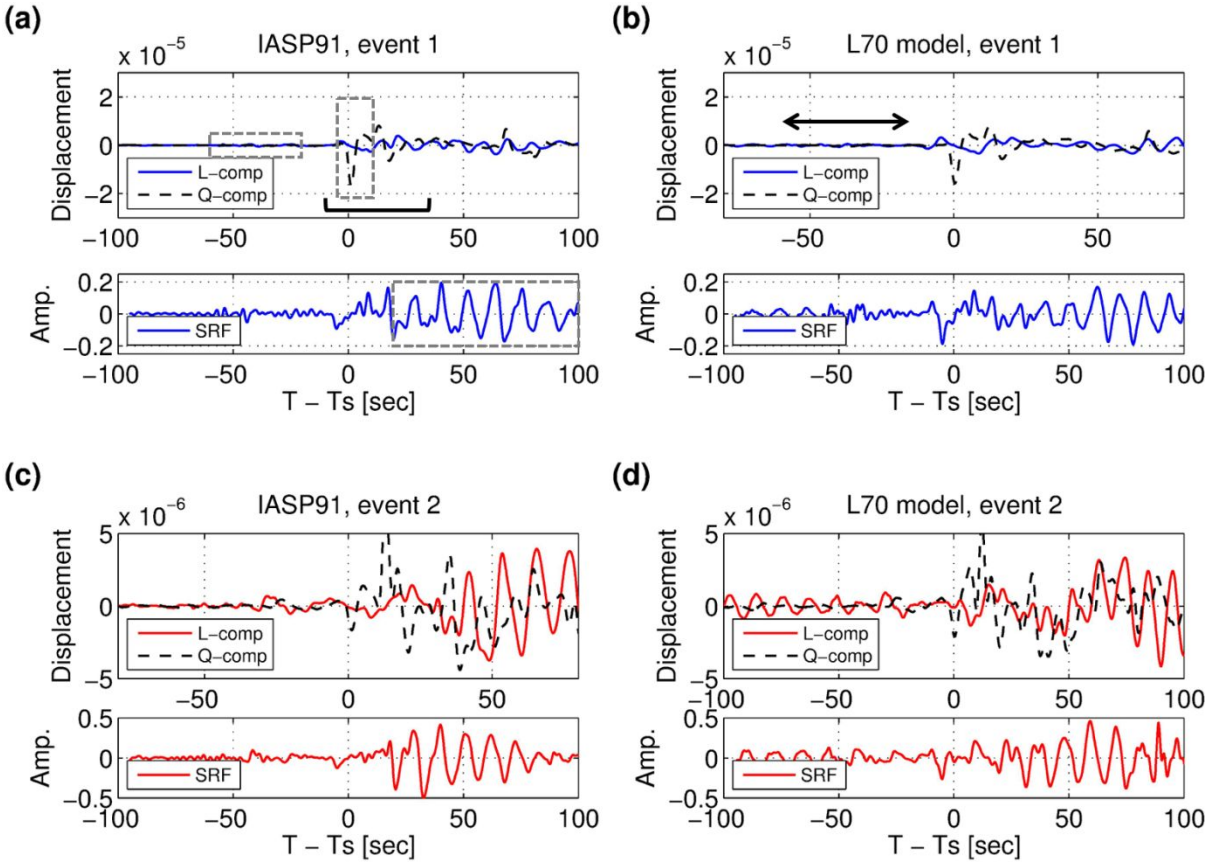

Figure 3. Examples showing *P* coda waves and their influence on signal-generated noise in the SRF. Gray dashed boxes in panel (a) indicate how LQR is measured from the L- and Q-component synthetic seismograms and how AMP is measured from synthetic SRF. Synthetic waveforms are computed from two earthquake sources (Fig. 1a, red beachballs) using the IASP91 (Kennett & Engdahl 1991) (a and c) and the L70 model (Fig. S1) (b and d). *S*-wave arrivals are aligned at zero time in the Q-component waveforms (dashed lines), and a time window for *P* coda waves are marked in a panel b (double arrow). Time-domain Wiener deconvolution method with minimum regularization (0.01% white noise) is performed within the parent waveform time window of 10 s before and 35 s after the *S* arrival (black bar in a panel a). Note the amplitude scale of SRF in case 2 is higher than that in case 1. See Figs S2 and S3 for cases for the time window of [-10 s 15 s] and [-10 s 10 s] with respect to *S* arrival, respectively.

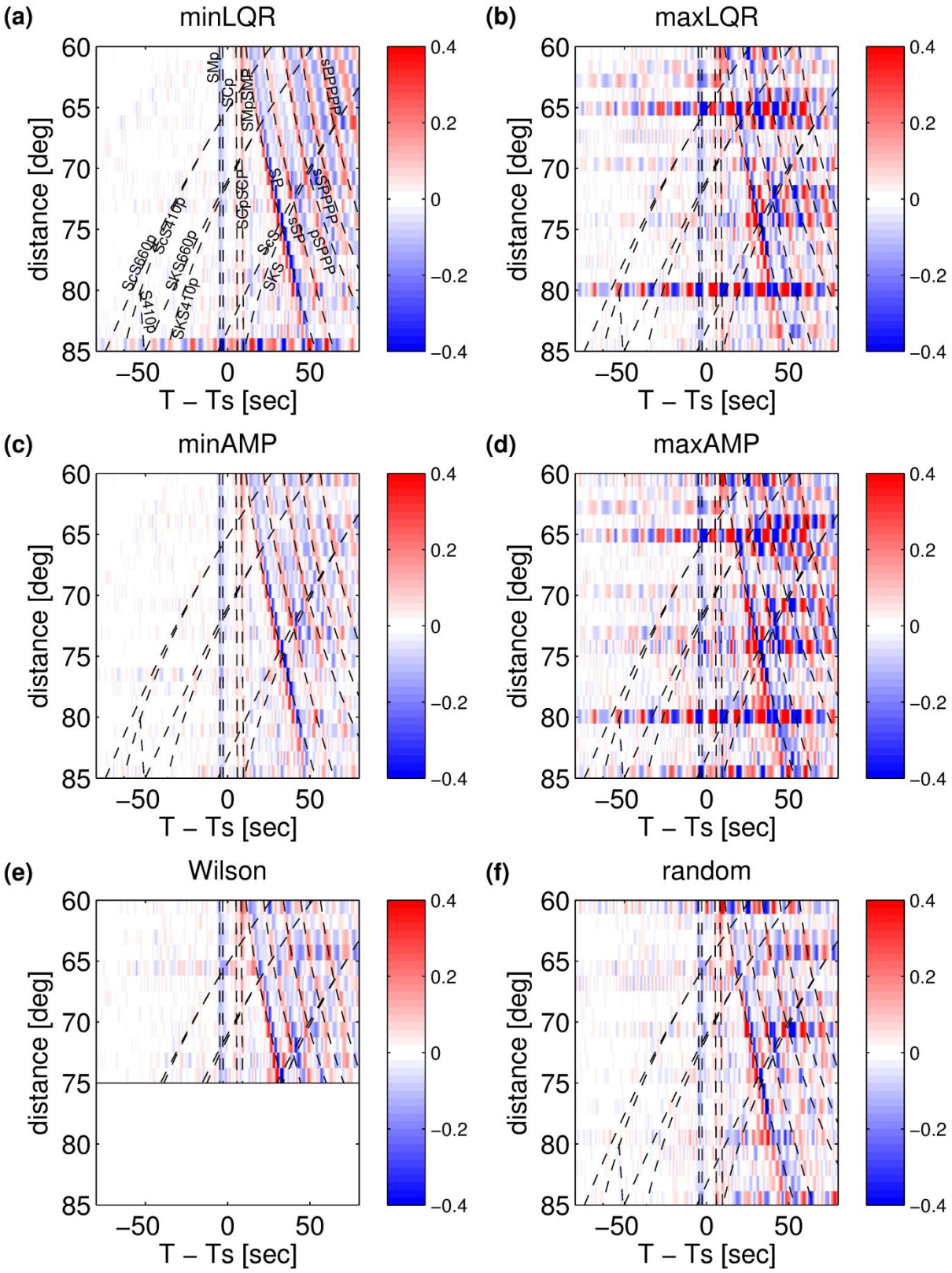
(a)
minLQR
(b)
maxLQR
(c)
minAMP
(d)
maxAMP
(e)
Wilson
(f)
random
distance [deg]
T – Ts [sec]
60
65
70
75
80
85
–50
0
50
0.4
0.2
0
–0.2
–0.4
SMp
SCp
SMpSMP
sPPPPP
SP
sSP
pSPPP
ScS
SKS
ScS660p
ScS410p
SKS660p
SKS410p
S410p

757

758

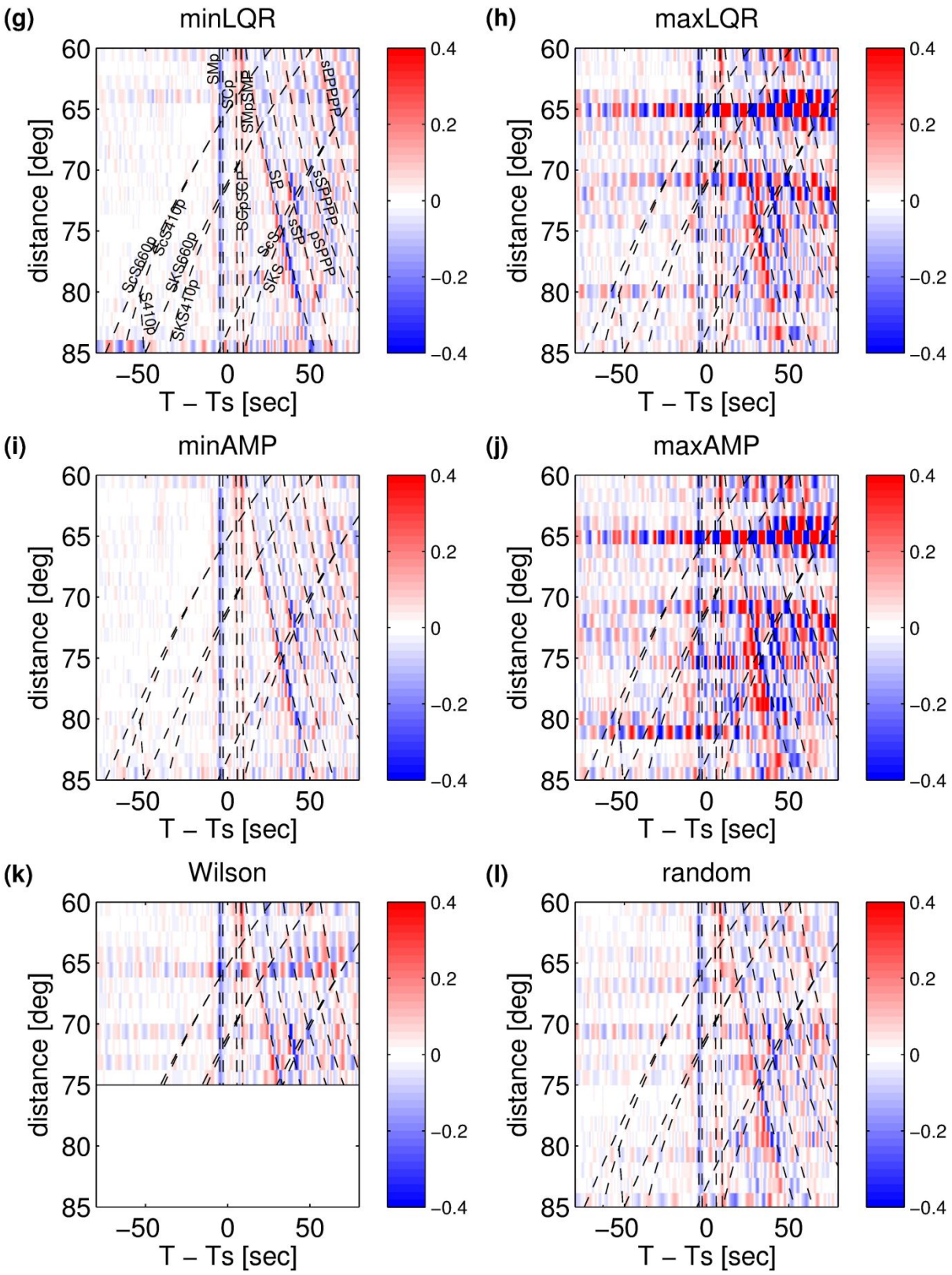

Figure 4. Images of synthetic SRFs for the IASP91 model (a–f) and L70 model (g–l) against epicentral distance and six data selection criteria. The SRFs are plotted in the same way as

Fig. 2. (a, g) Stacked SRFs with the 25% lowest LQR. (b, h) Stacked SRFs with the 25% highest LQR. (c, i) Stacked SRFs with the 25% lowest AMP. (d, j) Stacked SRFs with the 25% highest AMP. (e, k) Stacked SRFs with the criterion by Wilson *et al*. (2006). Note that Wilson *et al*. (2006) used restricted epicentral distances of 60°–75° for earthquakes with focal depths shallower than 300 km. (f, l) Stacked SRFs with 25% random data selection. Dashed lines indicate phase arrival times predicted by the IASP91 model.

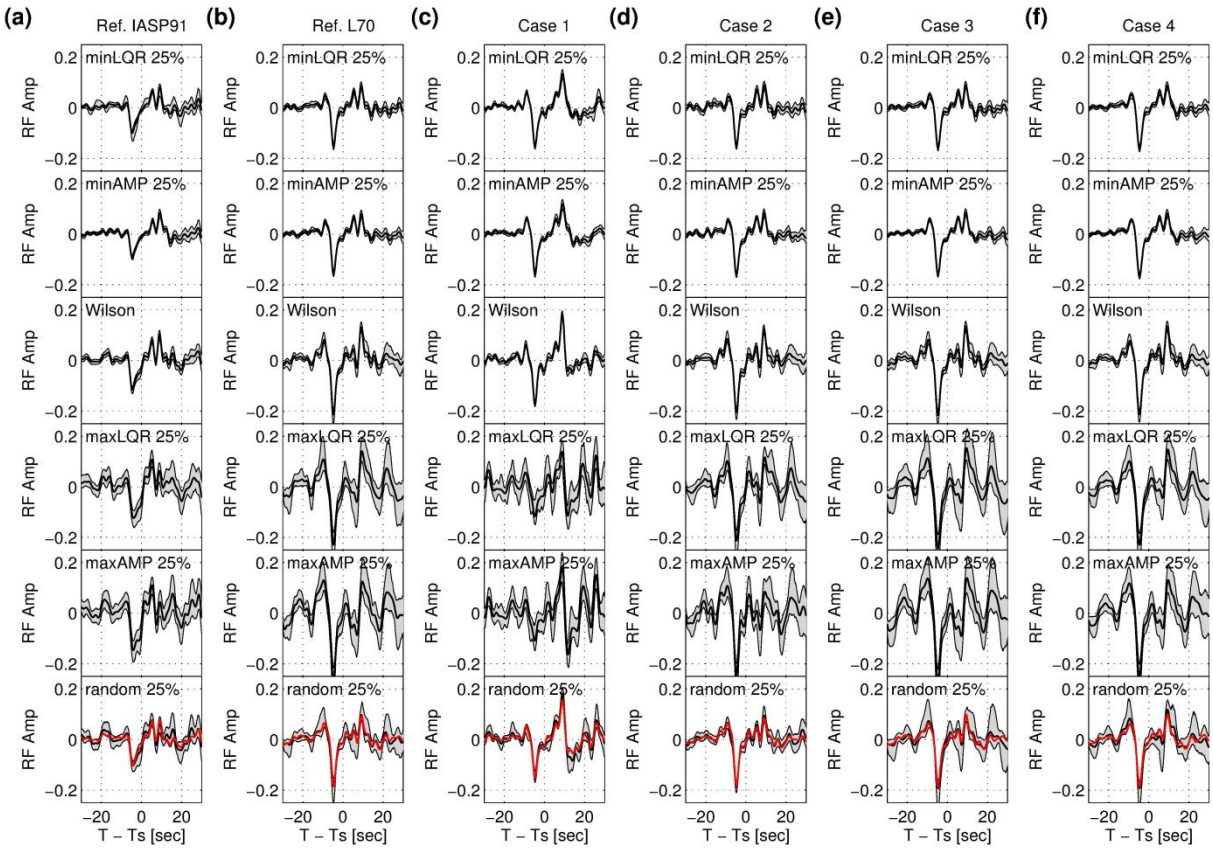

Figure 5. Stacked SRFs for various cases against six data selection criteria: 25% lowest LQR, 25% lowest AMP, the criterion by Wilson *et al*. (2006), 25% highest LQR, and 25% highest AMP, and 25% random data selection, from the top to bottom rows, respectively. Gray region indicates bootstrap error estimates of the SRFs. (a) Stacked SRFs for IASP91 model. (b) Stacked SRFs for L70 model. (c) Stacked SRFs for the case 1; same as (b) but with the window of parent waveform -10 s before and 15 s after the *S* wave. (d) Stacked SRFs for the case 2; same as (b) but with the Hanning tapering window of 5%. (e) Stacked SRFs for the case 3; same as (b), but with frequency-domain water-level deconvolution and water level of 0.05%. (f) Stacked SRFs for the case 4; same as (b), but with frequency-domain water-level deconvolution and water level of 0.2%. Note stacked SRFs without any selection criteria are shown in red lines for comparisons. The stack of all traces is shown in red in the bottom panel.

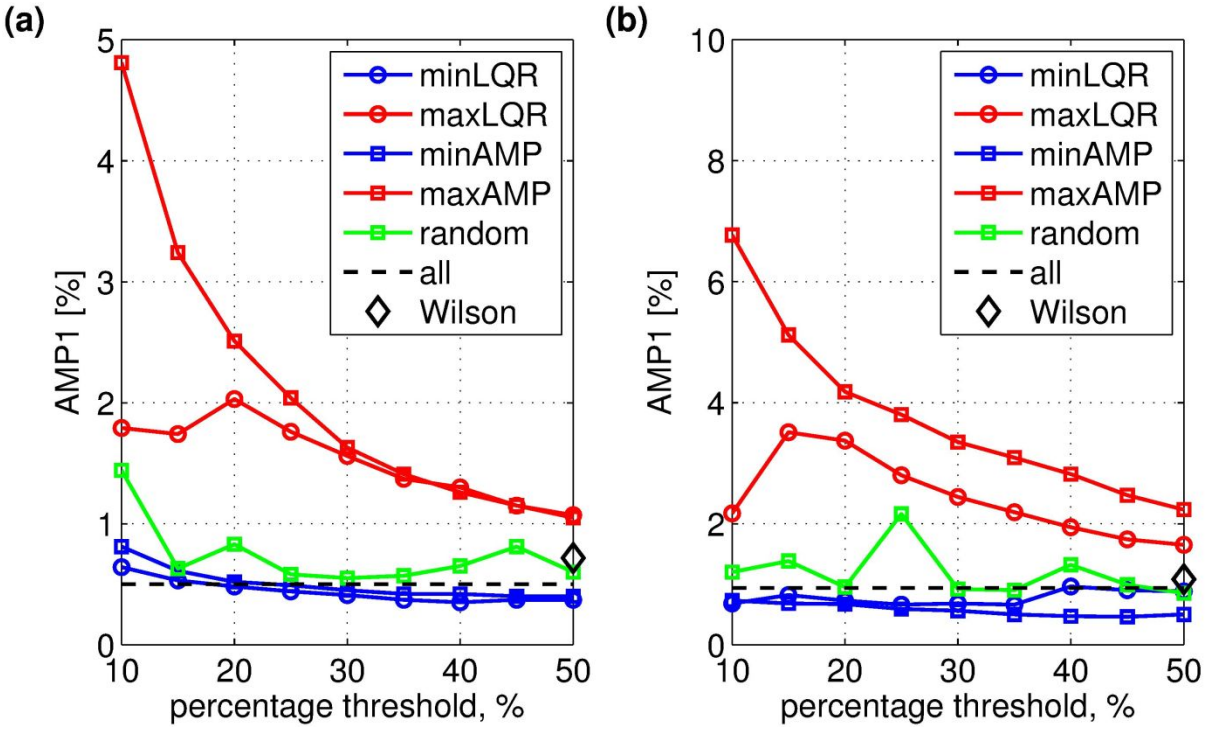

Figure 6. Root-mean-square (RMS) amplitudes of the synthetic SRFs at -60 to -20 s with respect to the *S* arrival (AMP1 in %), plotted against data-selection ratios (10–50%). (a) AMP1 for IASP91 model (Kennett & Engdahl 1991) with six criteria, which are lowest LQR (blue circle), highest LQR (red circle), lowest AMP (blue square), highest AMP (red square), random data selection (green square) and the criterion by Wilson *et al.* (2006) (black diamond), in addition to all SRFs (black dashed line). (b) AMP1 for L70 model (Fig. S1) with the same criteria as (a).

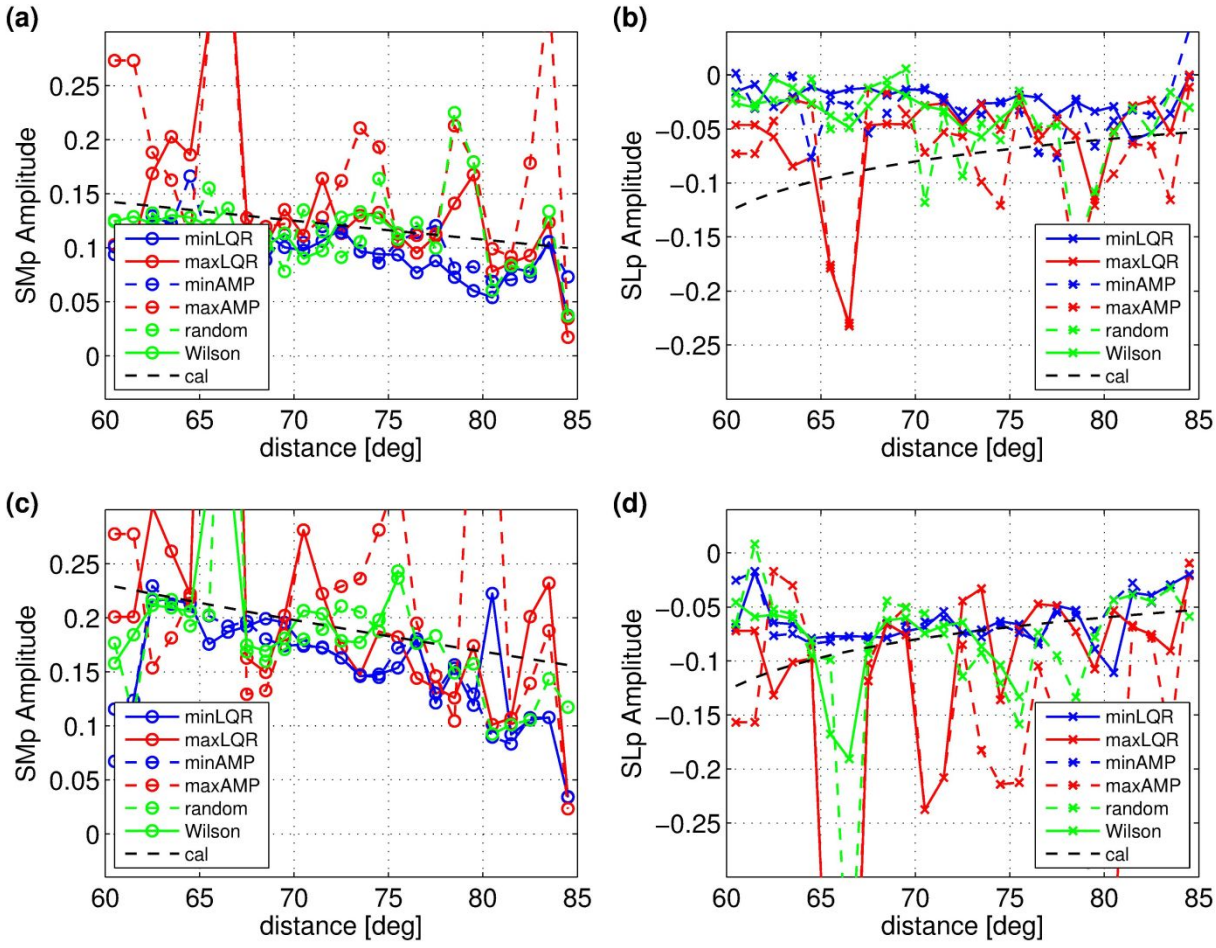

Figure 7. Amplitudes of *SMp* and *SLp* phases from the synthetic SRFs, plotted against the epicentral distance for the six different data selection criteria. The measured amplitudes are compared with the theoretical transmission coefficients (Aki & Richards 2002), shown in black dashed line. (a) Distance-dependent amplitude of *SMp* from IASP91 model (Kennett & Engdahl 1991). (b) Distance-dependent amplitude of *SLp* from IASP91 model. (c) Distance-dependent amplitude of *SMp* from L70 model (Fig. S1). (d) Distance-dependent amplitude of *SLp* from L70 model. Note that the theoretical calculation of *SLp* transmission coefficient from the L70 model is reproduced in Fig. 7b for comparison. In the absence of a negative velocity contrast in the IASP91 model, notable amplitude peak, especially with the highest LQR or AMP criteria, can still be identified and potentially misinterpreted as *SLp* signal in the LAS. Lowest LQR or AMP criteria substantially minimize these dubious signals.

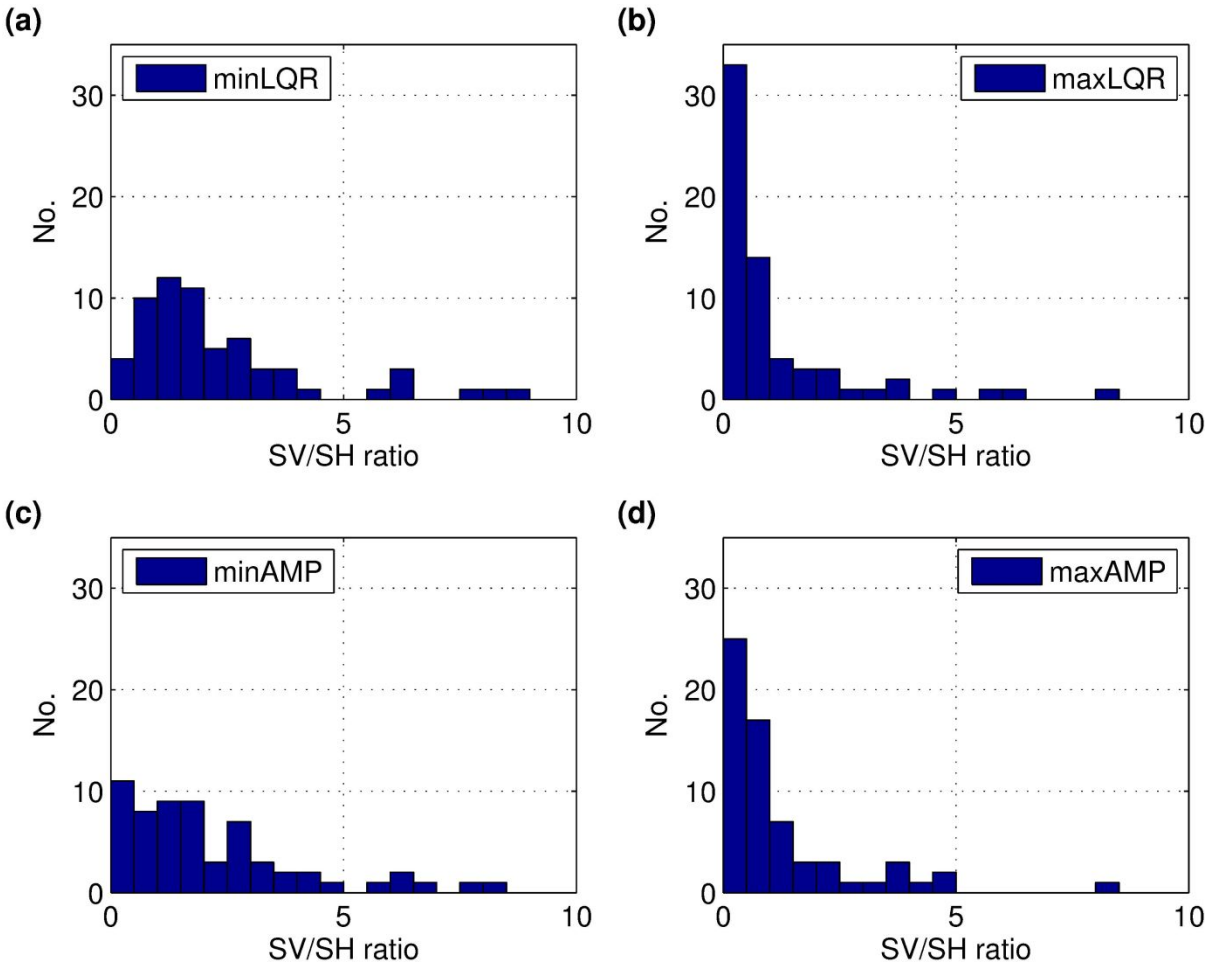

Figure 8. Histograms of *SV/SH* ratio against four data selection criteria; (a) 25% lowest LQR, (b) 25% highest LQR, (c) 25% lowest AMP, and (d) 25% highest AMP.

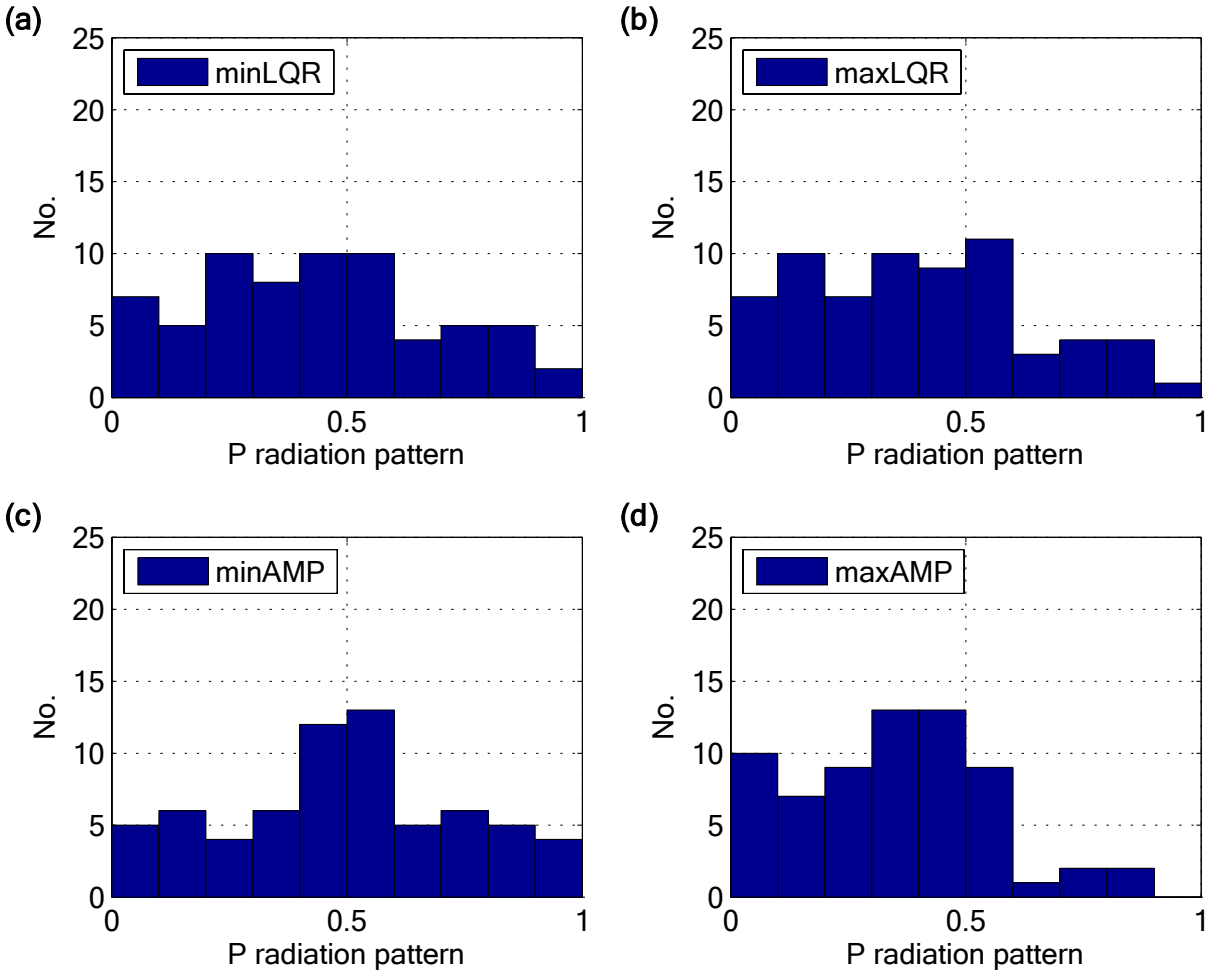

Figure 9. Histograms of *P* radiation pattern against four data selection criteria; (a) 25% lowest LQR, (b) 25% highest LQR, (c) 25% lowest AMP, and (d) 25% highest AMP. The *P* radiation pattern is computed with the slowness of *pPPPP* against focal mechanisms of selected events.

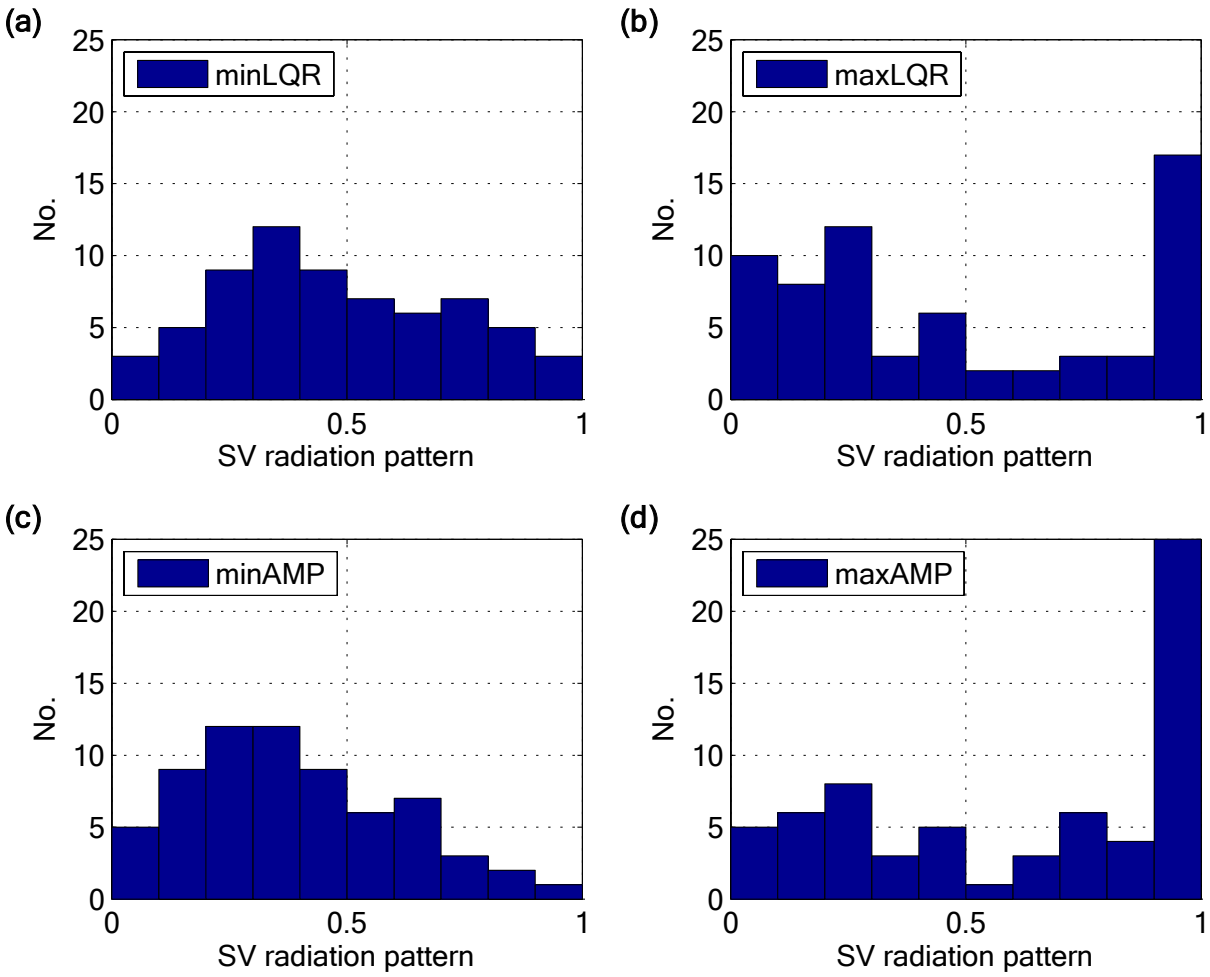

Figure 10. Histograms of *SV* radiation pattern against four data selection criteria; (a) 25% lowest LQR, (b) 25% highest LQR, (c) 25% lowest AMP, and (d) 25% highest AMP. The *SV* radiation pattern is computed with the slowness of *SP* wave against focal mechanisms of selected events.

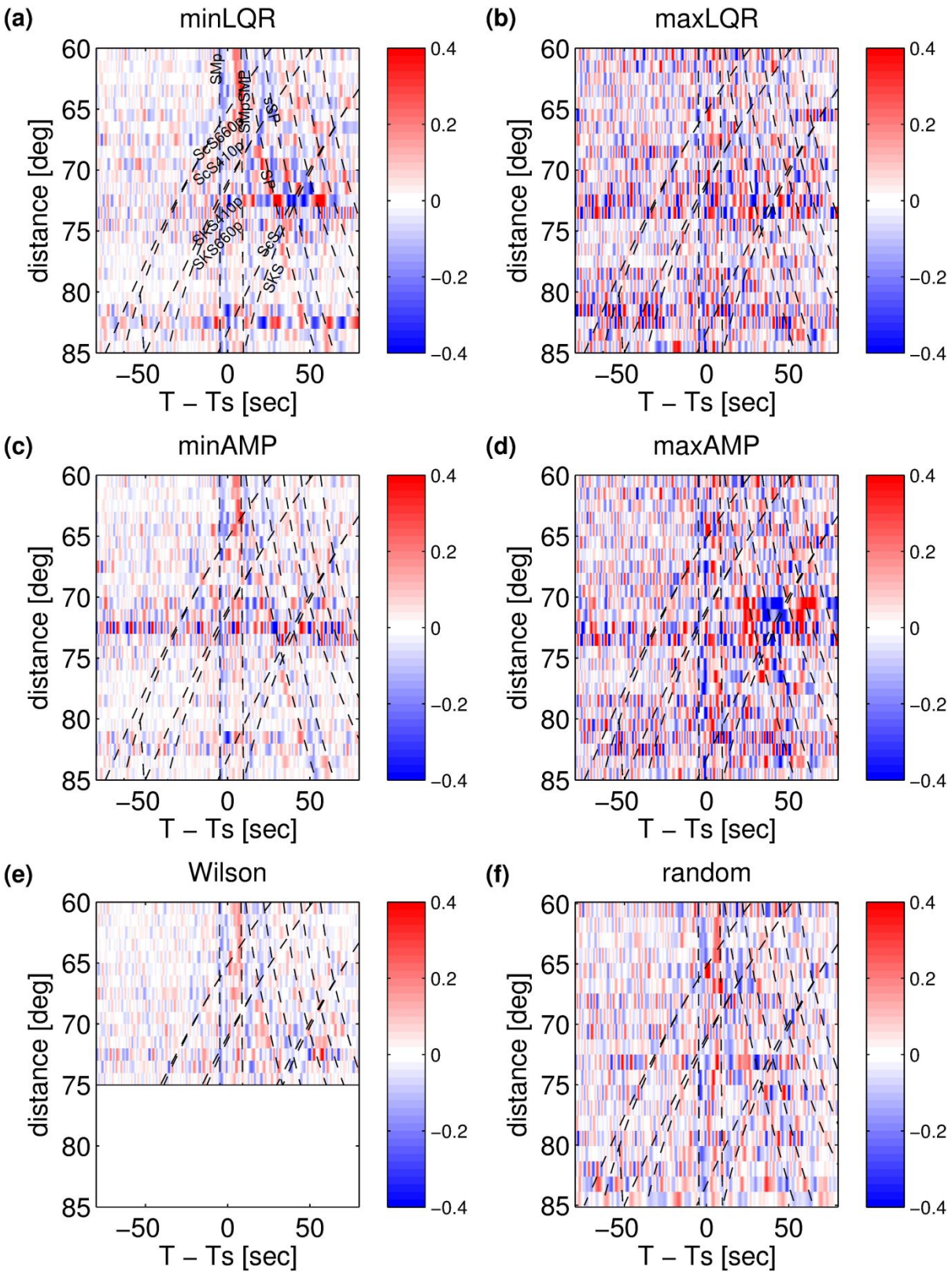

Figure 11. Images of SRFs for station TJN as a function of the distance of 60°–85° with six different data selection criteria. The SRFs are plotted in the same way as Fig. 2. (a) Stacked SRFs with the 25% lowest LQR. (b) Stacked SRFs with the 25% highest LQR. (c) Stacked

SRFs with the 25% lowest AMP. (d) Stacked SRFs with the 25% highest AMP. (e) Stacked SRFs with the criterion by Wilson *et al*. (2006). (f) Stacked SRFs with 25% random data selection. Dashed lines indicate phase arrival times predicted by the IASP91 model. See Fig. S10 for the images of -30–30 s time window.

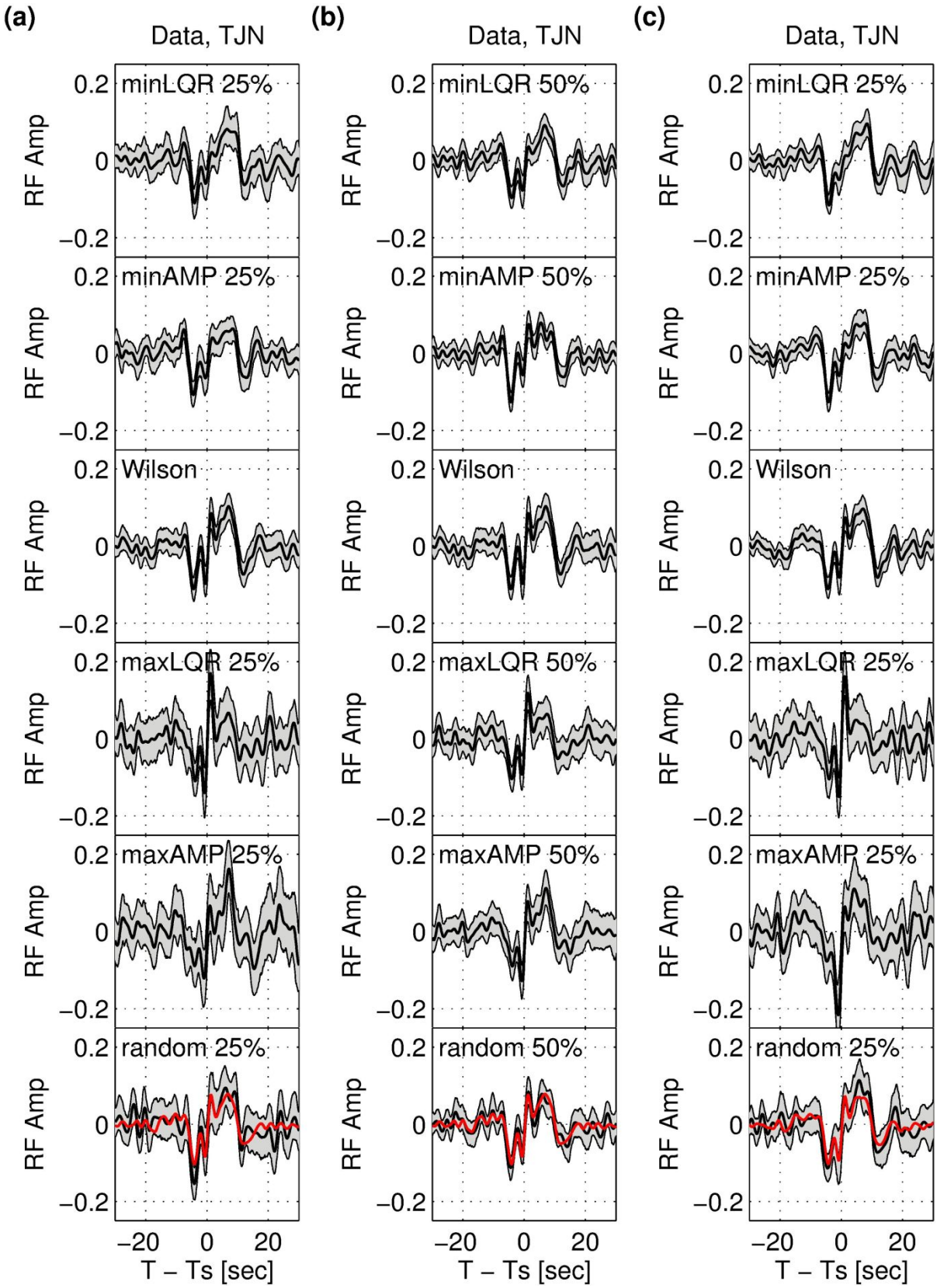

Figure 12. Stacked SRFs for station TJN with six data selection criteria with (a) a percentage threshold of 25%, (b) 50 %, and (b) 25% with a stronger regularization (1% white noise).

Gray region indicates bootstrap error estimates of the SRFs. The six data selection criteria are as follows: 25% lowest LQR, 25% lowest AMP, the criterion by Wilson *et al*. (2006), 25% highest LQR, and 25% highest AMP, and 25% random data selection, from the top to bottom rows, respectively.

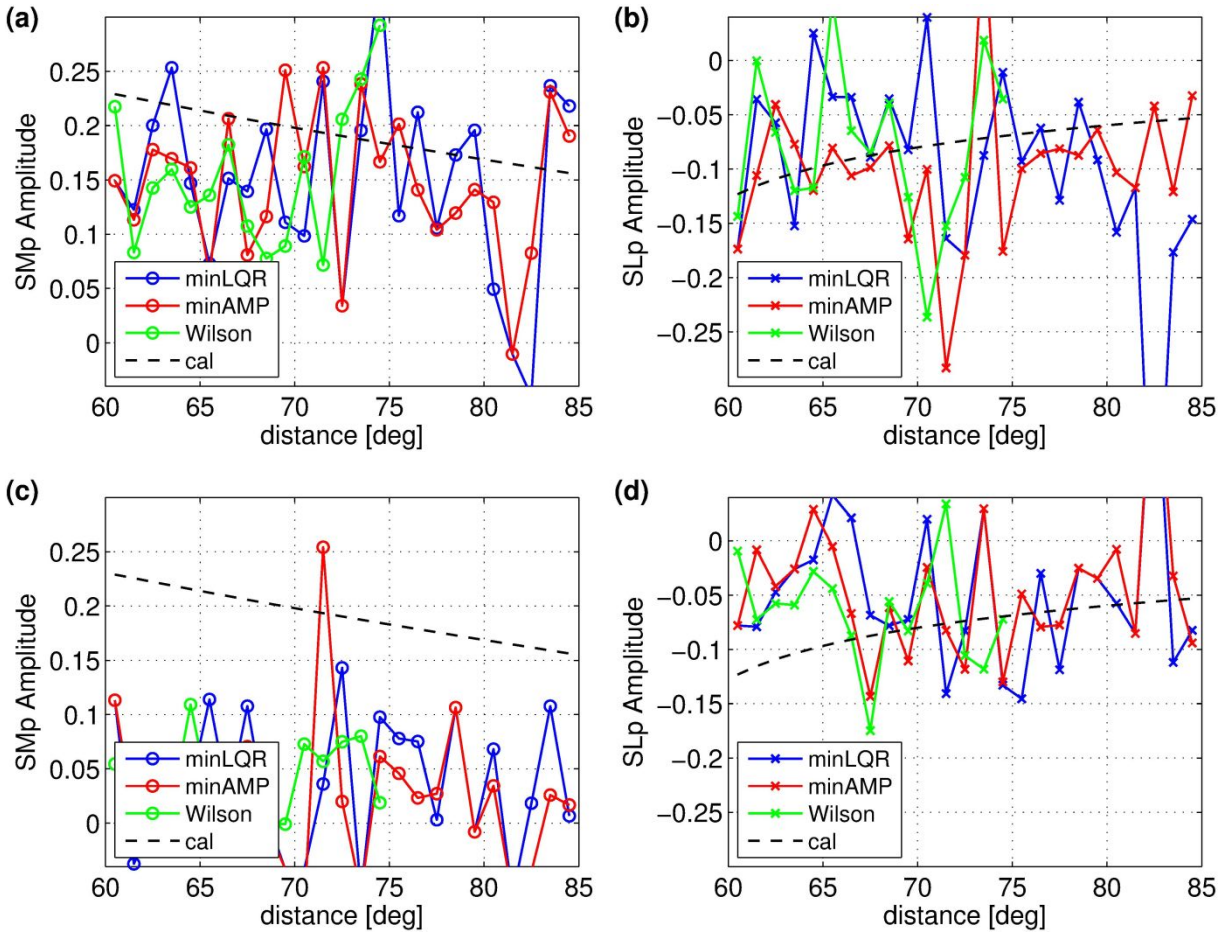

Figure 13. Amplitudes of *SMp* and *SLp* phases from the SRFs for station TJN, plotted against the distance of 60°–85° for three different data selection criteria (25% lowest LQR, 25% lowest AMP, and the criterion by Wilson *et al*. (2006)). The measured amplitudes are compared with the theoretical transmission coefficients (Aki & Richards 2002), shown in black dashed line. (a) Distance-dependent amplitude of *SMp*. (b) Distance-dependent amplitude of *SLp*. (c) Distance-dependent amplitude of *SMp* with a strong regularization (1% white noise). (d) Distance-dependent amplitude of *SLp* with a strong regularization (1% white noise).

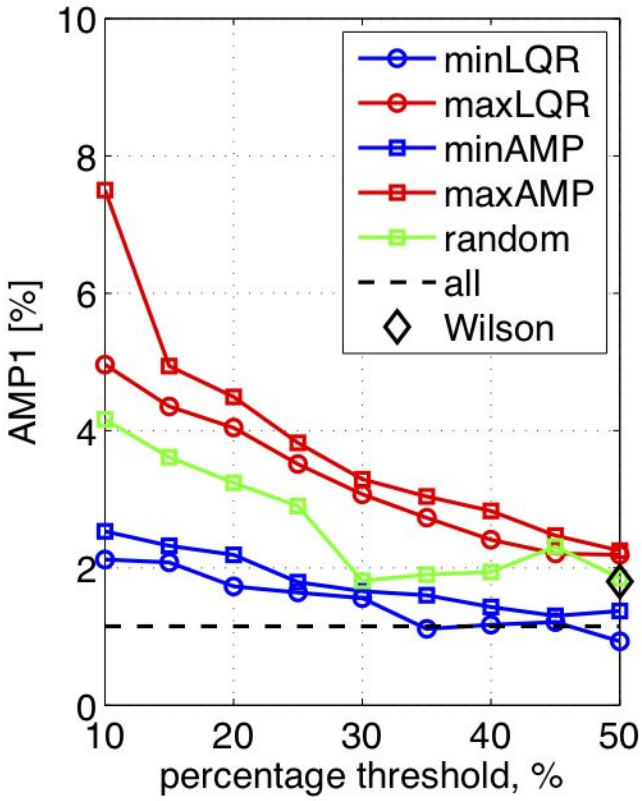

Figure 14. Root-mean-square (RMS) amplitudes of the SRFs at -60 to -20 s with respect to the *S* arrival (AMP1 in %) for station TJN, plotted against data-selection ratios (10–50%). The six data selection criteria are as follows: lowest LQR (blue circle), highest LQR (red circle), lowest AMP (blue square), highest AMP (red square), random data selection (green square) and the criterion by Wilson *et al*. (2006) (black diamond), in addition to all SRFs (black dashed line).

Supporting Information

Additional Supporting Information may be found in the online version of this article:

Supporting Information file includes one table and 14 figures providing velocity models for synthetic tests (Fig. S1), illustrations showing how the synthetic SRFs are constructed with our proposed data selection criteria for shorter time windows for the time-domain Wiener deconvolution (Figs S2 and S3), effect of using different data windowing and tapering length (Figs S4 and S5, respectively), effect of using various water levels in the alternative frequency-domain deconvolution (Figs S6 and S7), histograms of epicentral distance and event back-azimuth (Fig. S8) as well as source parameters (Fig. S9) against data selection criteria, and an alternative 50% threshold for six data selection criteria for the SRFs from station TJN (Figs S11 and S12) in addition to 25% threshold (Fig. S10). SRFs images with 25% threshold and a strong regularization (1% white noise) are shown in Figs S13 and S14.

Table S1. Velocity models.

Figure S1. Velocity models. The 1-D IASP91 model (Kennett & Engdahl 1991) is shown in black, and the L70 model is shown in red. The L70 model includes a 35 km thick high-velocity mantle lid with a 7.5% shear velocity increase below Moho, a low velocity zone with a 9% shear velocity reduction beneath 70 km depth, and a small 1.5% shear velocity increase beneath 120 km depth. See also Table S1.

Figure S2. Examples showing *P* coda waves and their influence on signal-generated noise in the SRF. Gray dashed boxes in panel (a) indicate how LQR is measured from the L- and Q-

component synthetic seismograms and how AMP is measured from synthetic SRF. Synthetic waveforms are computed from catalogued earthquake sources using the IASP91 (Kennett & Engdahl 1991) (a and c) and the L70 model (b and d). Time-domain Wiener deconvolution method is performed with the parent waveform time window of 10 s before and 15 s after the *S* arrival (black bar in a panel a). Note the amplitude scale of SRF in event 2 is higher than that in event 1.

Figure S3. Examples showing *P* coda waves and their influence on signal-generated noise in the SRF. Gray dashed boxes in panel (a) indicate how LQR is measured from the L- and Q-component synthetic seismograms and how AMP is measured from synthetic SRF. Synthetic waveforms are computed from catalogued earthquake sources using the IASP91 (Kennett & Engdahl 1991) (a and c) and the L70 model (b and d). Time-domain Wiener deconvolution method is performed with the parent waveform time window of 10 s before and 10 s after the *S* arrival (black bar in a panel a). Note the amplitude scale of SRF in event 2 is higher than that in event 1.

Figure S4. Images of synthetic SRFs for the case 1 from the L70 model as a function of the distance of 60°–85° with following six data selection criteria; (a) 25% lowest LQR, (b) 25% highest LQR, (c) 25% lowest AMP, (d) 25% highest AMP, (e) criterion by Wilson *et al*. (2006), and (f) 25% random data selection. The parent waveforms are windowed 10 s before and 15 s after the *S*-wave arrival and tapered with a 15% Hanning taper at both ends of the signal window. Dashed lines indicate phase arrival times predicted by the IASP91 model (Kennett & Engdahl 1991). The SRFs are plotted in the same way as Fig. 2.

Figure S5. Images of synthetic SRFs for the case 2 from the L70 model as a function of the epicentral distance of 60°–85° with six different data selection criteria. The parent waveforms are windowed 10 s before and 35 s after the *S*-wave arrival and tapered with a 5% Hanning taper at both ends of the signal window. See a caption of Fig. S4 for more detail.

Figure S6. Images of synthetic SRFs for the case 3 from the L70 model as a function of the epicentral distance of 60°–85° with six different data selection criteria. The parent waveforms are windowed 10 s before and 35 s after the *S*-wave arrival and tapered with a 15% Hanning taper at both ends of the signal window. The frequency-domain deconvolution is done with a water level of 0.05%. See a caption of Fig. S4 for more detail.

Figure S7. Images of synthetic SRFs for the case 4 from the L70 model as a function of the distance of 60°–85° with six different data selection criteria. The parent waveforms are windowed 10 s before and 35 s after the *S*-wave arrival and tapered with a 15% Hanning taper at both ends of the signal window. The frequency-domain deconvolution is done with a water level of 0.2%. See a caption of Fig. S4 for more detail.

Figure S8. Histograms of epicentral distance and back azimuth against six data selection criteria. LQR and AMP data selection criteria with a percentage threshold of 25% result in negligible data selection bias in back azimuthal and epicentral distance.

Figure S9. Histograms of earthquake source parameters (dip, strike and rake) against four data selection criteria; (a, e, f) 25% lowest LQR, (b, f, j) 25% highest LQR, (c, g, k) 25% lowest AMP, and (d, h, l) 25% highest AMP. LQR and AMP data selection criteria result in negligible data selection preference in source parameters.

Figure S10. Images of SRFs for station TJN as a function of the epicentral distance of 60°–85° with following six data selection criteria; (a) 25% lowest LQR, (b) 25% highest LQR, (c) 25% lowest AMP, (d) 25% highest AMP, (e) criterion by Wilson *et al*. (2006), and (f) 25% random data selection. The parent waveforms are windowed 10 s before and 35 s after the *S*-wave arrival and tapered with a 15% Hanning taper at both ends of the signal window. See a caption of Fig. S4 for more detail. See also Fig. 10 for the images of -80–80 s window.

Figure S11. Images of SRFs for station TJN as a function of the distance of 60°–85° with following six data selection criteria; (a) 50% lowest LQR, (b) 50% highest LQR, (c) 50% lowest AMP, (d) 50% highest AMP, (e) criterion by Wilson *et al*. (2006), and (f) 50% random data selection. The parent waveforms are windowed 10 s before and 35 s after the *S*-wave arrival and tapered with a 15% Hanning taper at both ends of the signal window. See a caption of Fig. S4 for more detail. See Fig. S12 for the images plotted for -30–30 s window.

Figure S12. Images of SRFs for station TJN as a function of the distance of 60°–85° with following six data selection criteria; (a) 50% lowest LQR, (b) 50% highest LQR, (c) 50% lowest AMP, (d) 50% highest AMP, (e) criterion by Wilson *et al*. (2006), and (f) 50% random data selection. The parent waveforms are windowed 10 s before and 35 s after the *S*-wave arrival and tapered with a 15% Hanning taper at both ends of the signal window. See a caption of Fig. S4 for more detail.

Figure S13. Images of SRFs for station TJN as a function of the distance of 60°–85° with following six data selection criteria; (a) 25% lowest LQR, (b) 25% highest LQR, (c) 25% lowest AMP, (d) 25% highest AMP, (e) criterion by Wilson *et al*. (2006), and (f) 25%

random data selection. The parent waveforms are windowed 10 s before and 35 s after the *S*-wave arrival and tapered with a 15% Hanning taper at both ends of the signal window. Time domain wiener deconvolution is done with a strong regularization of 1% white noise. See Fig. S14 for the images plotted for -30–30 s window.

Figure S14. Images of SRFs for station TJN as a function of the distance of 60°–85° with following six data selection criteria; (a) 25% lowest LQR, (b) 25% highest LQR, (c) 25% lowest AMP, (d) 25% highest AMP, (e) criterion by Wilson *et al*. (2006), and (f) 25% random data selection. The parent waveforms are windowed 10 s before and 35 s after the *S*-wave arrival and tapered with a 15% Hanning taper at both ends of the signal window. Time domain wiener deconvolution is done with a strong regularization of 1% white noise.

Supporting Information for

Data-oriented constraint on the interpretation of *S* receiver function and its application to observations of seismic discontinuities in the lithosphere-asthenosphere system

Xuzhang Shen[1], YoungHee Kim[2*], Teh-Ru Alex Song[3], and Hobin Lim[2]

1 Guangdong Provincial Key Laboratory of Geodynamics and Geohazards, School of Earth Sciences and Engineering, Sun Yat-Sen University, Guangzhou, 510275, China

2 School of Earth and Environmental Sciences, Seoul National University Seoul, 08826, Republic of Korea (younghkim@snu.ac.kr)

3 Seismological Laboratory, Department of Earth Sciences, University College London, WC1E 6BT, London, United Kingdom

* Corresponding author

Email: younghkim@snu.ac.kr

Phone: +82-2-880-6735

Supporting Information file includes one table and 14 figures providing velocity models for synthetic tests (Fig. S1), illustrations showing how the synthetic SRFs are constructed with our proposed data selection criteria for shorter time windows for the time-domain Wiener deconvolution (Figs S2 and S3), effect of using different data windowing and tapering length (Figs S4 and S5, respectively), effect of using various water levels in the alternative frequency-domain deconvolution (Figs S6 and S7), histograms of epicentral distance, event back-azimuth (Fig. S8) as well as source parameters (Fig. S9) against data selection criteria, and an alternative 50% threshold for six data selection criteria for the SRFs from station TJN (Figs S11 and S12) in addition to 25% threshold (Fig. S10). SRFs images with 25% threshold and a strong regularization (1% white noise) are shown in Figs S13 and S14.

Table S1. Velocity models.

IASP91 model[a]				**L70 model**			
Depth (km)	Vp (km/s)	Vs (km /s)	Density (g/cm^3)	Depth (km)	Vp (km/s)	Vs (km /s)	Density (g/cm^3)
0	5.800	3.360	2.7200	0	5.8000	3.3600	2.7200
20	5.800	3.360	2.7200	20	5.8000	3.3600	2.7200
20	6.500	3.750	2.9200	20	6.5000	3.7500	2.9200
35	6.500	3.750	2.9200	35	6.5000	3.7500	2.9200
35	8.040	4.470	3.3198	35	8.2596	4.8053	3.3797
77.5	8.045	4.485	3.3455	70	8.2637	4.8141	3.3758
120	8.050	4.500	3.3713	70	8.0020	4.4187	3.3758
165	8.175	4.509	3.3985	120	8.0500	4.5000	3.3713
210	8.300	4.518	3.4258	165	8.1750	4.5090	3.3985
				210	8.3000	4.5180	3.4258

[a] Kennett & Engdahl (1991)

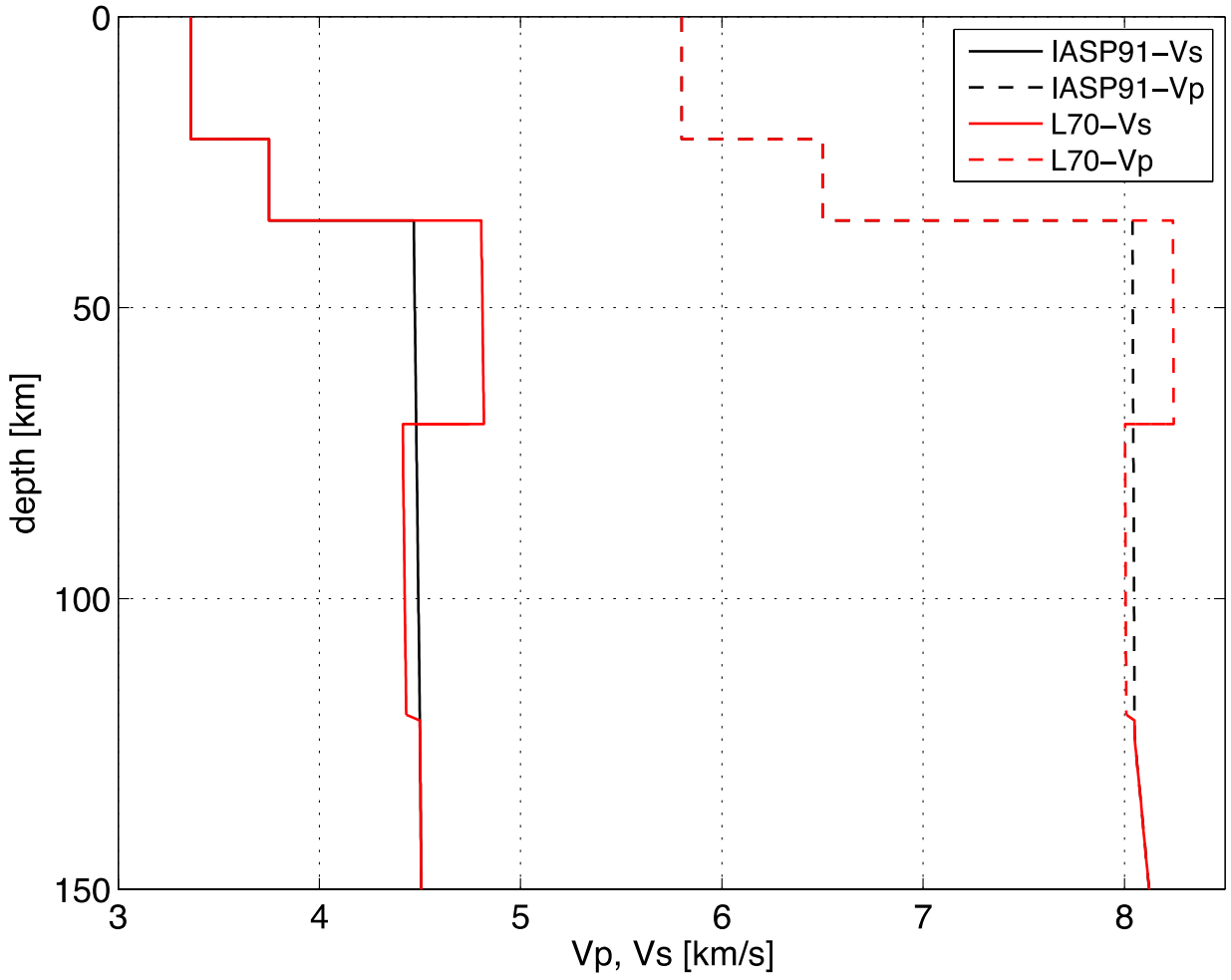

Figure S1. Velocity models. The 1-D IASP91 model (Kennett & Engdahl 1991) is shown in black, and the L70 model is shown in red. The L70 model includes a 35 km thick high-velocity mantle lid with a 7.5% shear velocity increase below Moho, a low velocity zone with a 9% shear velocity reduction beneath 70 km depth, and a small 1.5% shear velocity increase beneath 120 km depth. See also Table S1.

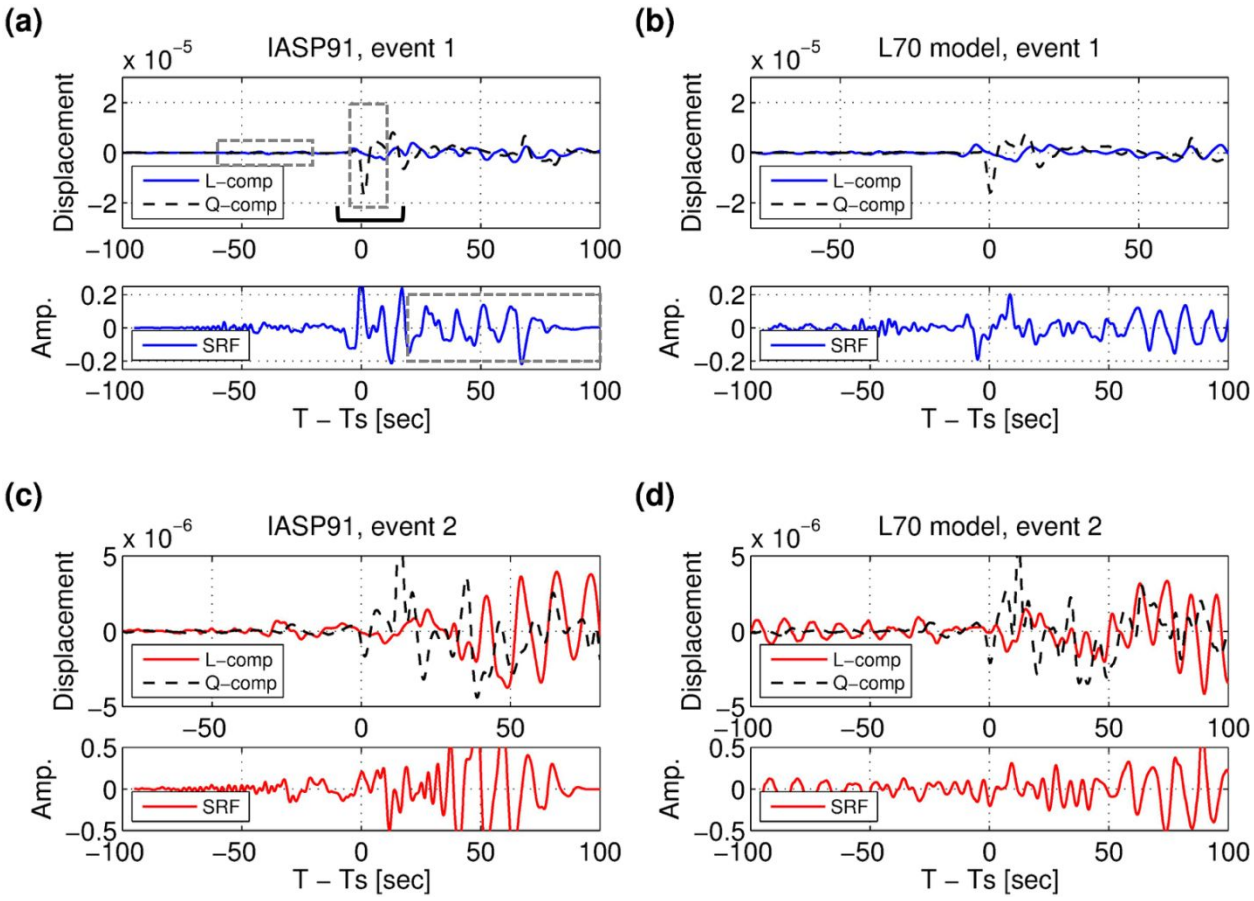

Figure S2. Examples showing *P* coda waves and their influence on signal-generated noise in the SRF. Gray dashed boxes in panel (a) indicate how LQR is measured from the L- and Q-component synthetic seismograms and how AMP is measured from synthetic SRF. Synthetic waveforms are computed from catalogued earthquake sources using the IASP91 (Kennett & Engdahl 1991) (a and c) and the L70 model (b and d). Time-domain Wiener deconvolution method is performed with the parent waveform time window of 10 s before and 15 s after the *S* arrival (black bar in a panel a). Note the amplitude scale of SRF in event 2 is higher than that in event 1.

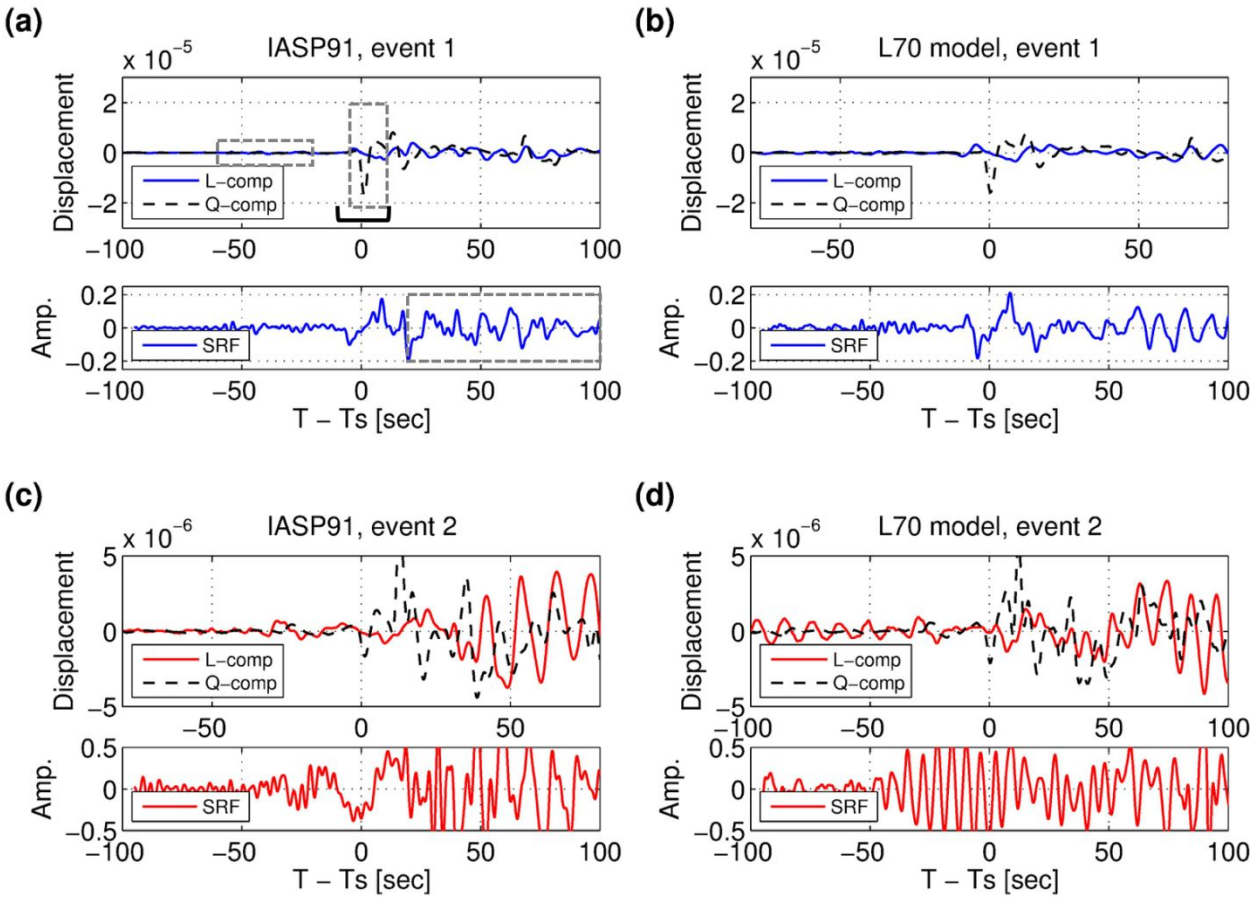

Figure S3. Examples showing *P* coda waves and their influence on signal-generated noise in the SRF. Gray dashed boxes in panel (a) indicate how LQR is measured from the L- and Q-component synthetic seismograms and how AMP is measured from synthetic SRF. Synthetic waveforms are computed from catalogued earthquake sources using the IASP91 (Kennett & Engdahl 1991) (a and c) and the L70 model (b and d). Time-domain Wiener deconvolution method is performed with the parent waveform time window of 10 s before and 10 s after the *S* arrival (black bar in a panel a). Note the amplitude scale of SRF in event 2 is higher than that in event 1.

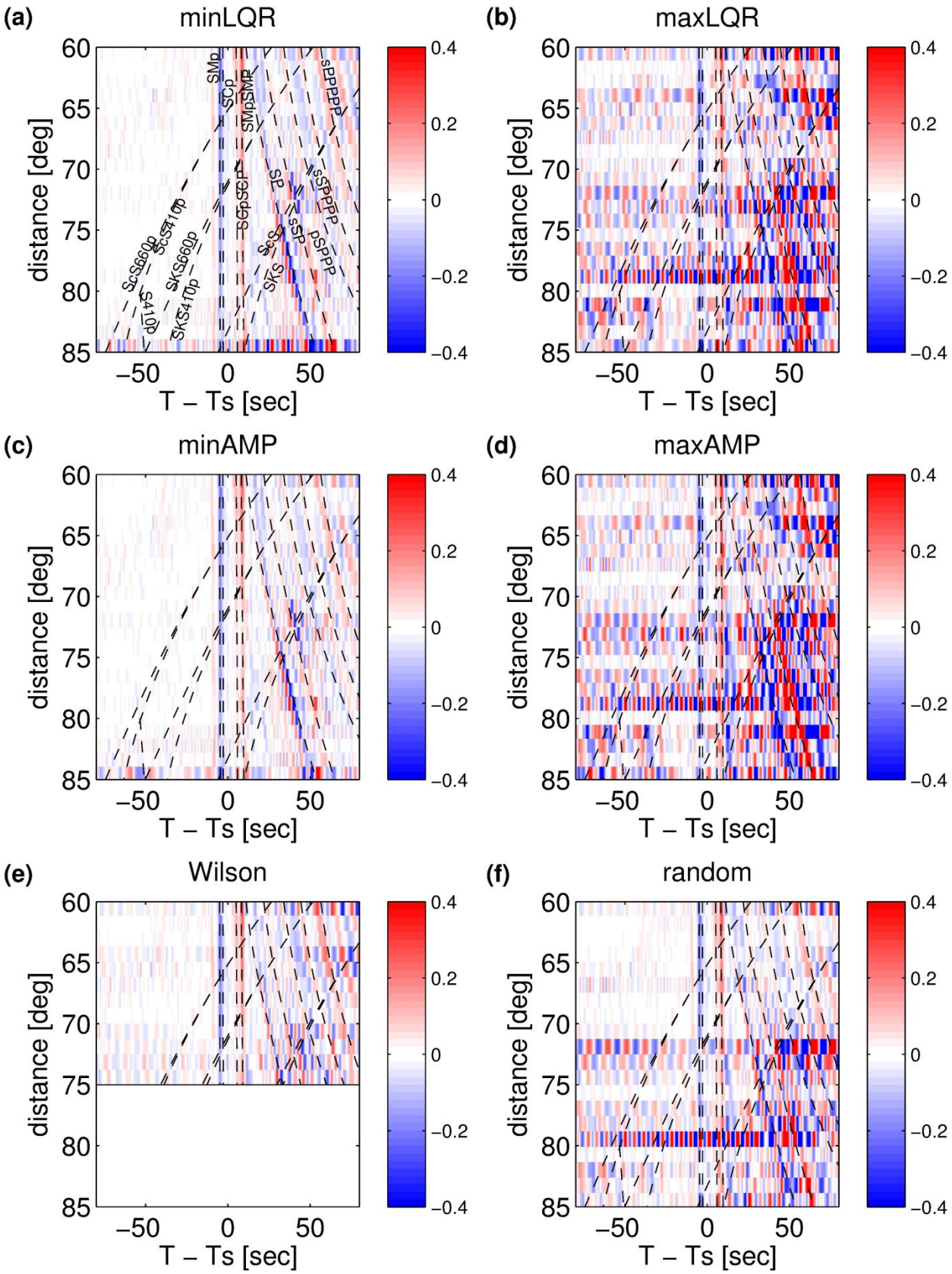
(a)
minLQR
(b)
maxLQR
(c)
minAMP
(d)
maxAMP
(e)
Wilson
(f)
random
distance [deg]
T – Ts [sec]
60
65
70
75
80
85
–50
0
50
0.4
0.2
0
–0.2
–0.4
SMp
SCp
SMpSMP
SCpSCP
SP
sSP
pSP
SKS
sSPPPP
pSPPP
ScS
ScS660p
ScS410p
SKS660p
SKS410p
S410p

Figure S4. Images of synthetic SRFs for the case 1 from the L70 model as a function of the distance of 60°–85° with following six data selection criteria; (a) 25% lowest LQR, (b) 25% highest LQR, (c) 25% lowest AMP, (d) 25% highest AMP, (e) criterion by Wilson *et al*. (2006), and (f) 25% random data selection. The parent waveforms are windowed 10 s before and 15 s after the *S*-wave arrival and tapered with a 15% Hanning taper at both ends of the signal window. Dashed lines indicate phase arrival times predicted by the IASP91 model (Kennett & Engdahl 1991). The SRFs are plotted in the same way as Fig. 2.

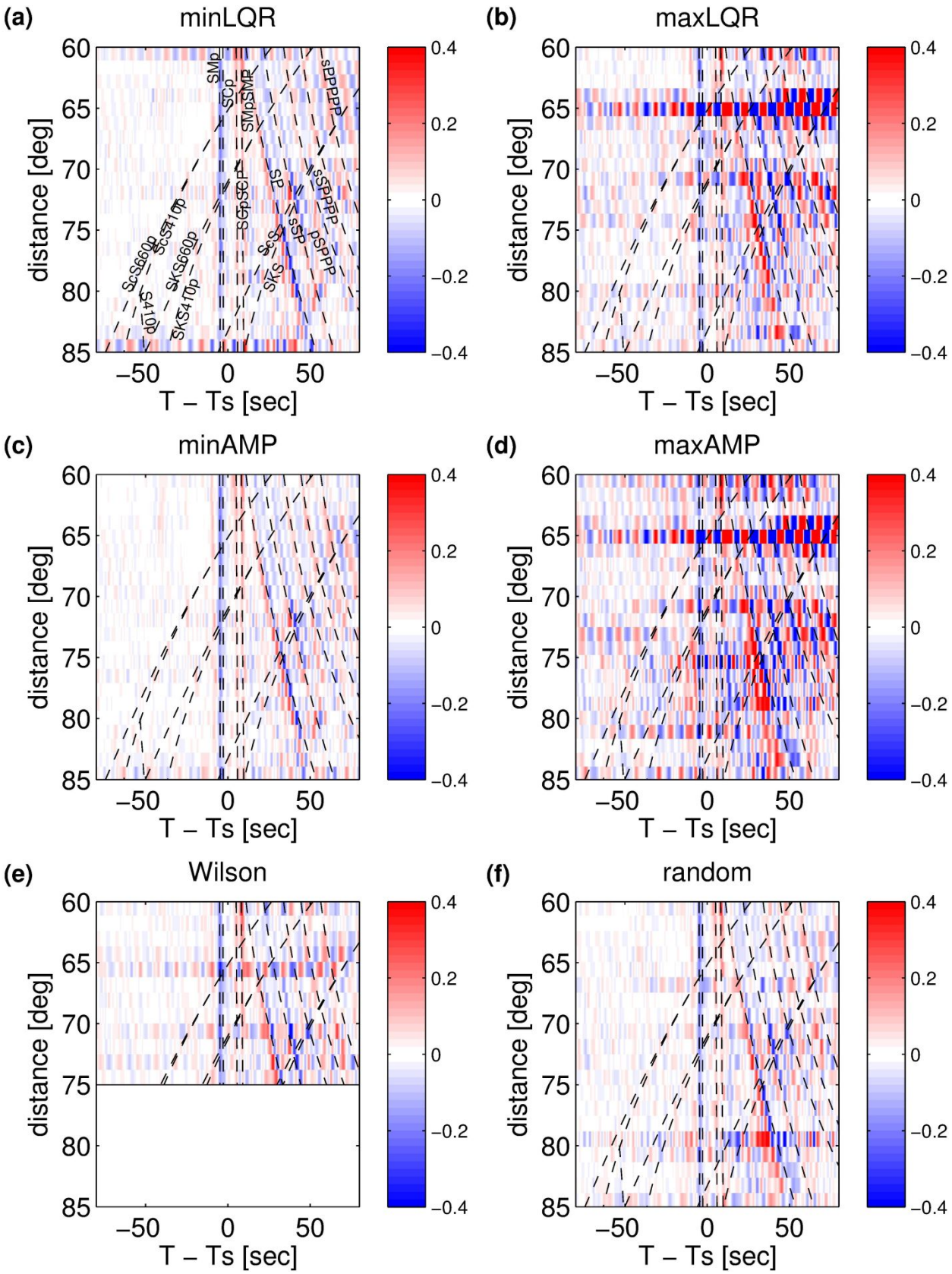
(a)
minLQR
(b)
maxLQR
(c)
minAMP
(d)
maxAMP
(e)
Wilson
(f)
random
distance [deg]
T – Ts [sec]
SMp
SCp
SMpSMP
SGpSGP
SP
sSP
ScS
SKS
sSPPPP
pSPPP
ScS660p
ScS410p
SKS660p
SKS410p
S410p
60
65
70
75
80
85
–50
0
50
0.4
0.2
0
–0.2
–0.4

Figure S5. Images of synthetic SRFs for the case 2 from the L70 model as a function of the epicentral distance of 60°–85° with six different data selection criteria. The parent waveforms are windowed 10 s before and 35 s after the *S*-wave arrival and tapered with a 5% Hanning taper at both ends of the signal window. See a caption of Fig. S4 for more detail.

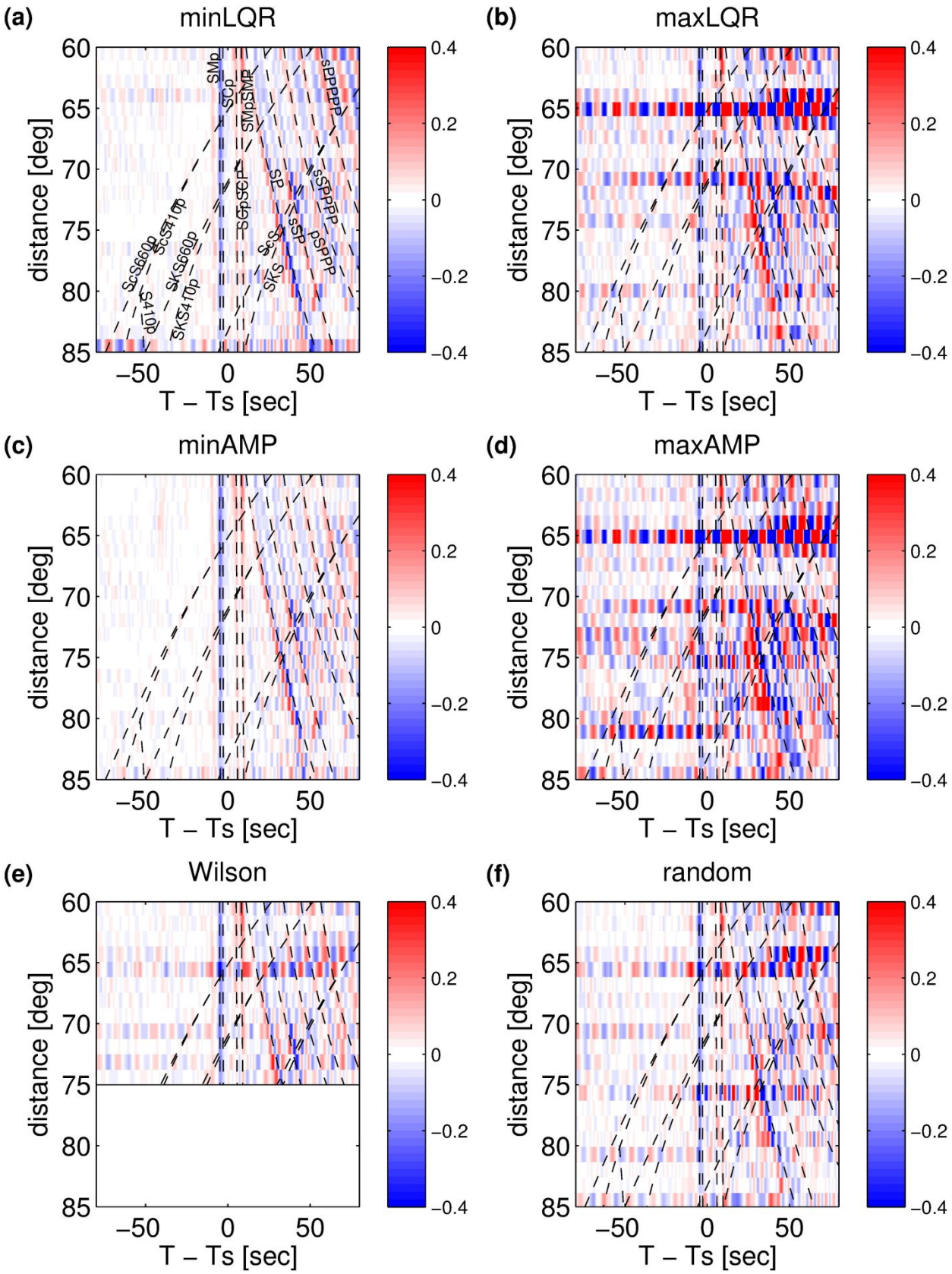
(a)
minLQR
(b)
maxLQR
(c)
minAMP
(d)
maxAMP
(e)
Wilson
(f)
random
distance [deg]
T – Ts [sec]
60
65
70
75
80
85
–50
0
50
0.4
0.2
0
–0.2
–0.4
SMp
SCp
SMpSMP
SP
sSP
pSPPP
sSPPPP
ScS
SKS
ScS660p
ScS410p
SKS660p
SKS410p
S410p

Figure S6. Images of synthetic SRFs for the case 3 from the L70 model as a function of the epicentral distance of 60°–85° with six different data selection criteria. The parent waveforms are windowed 10 s before and 35 s after the *S*-wave arrival and tapered with a 15% Hanning taper at both ends of the signal window. The frequency-domain deconvolution is done with a water level of 0.05%. See a caption of Fig. S4 for more detail.

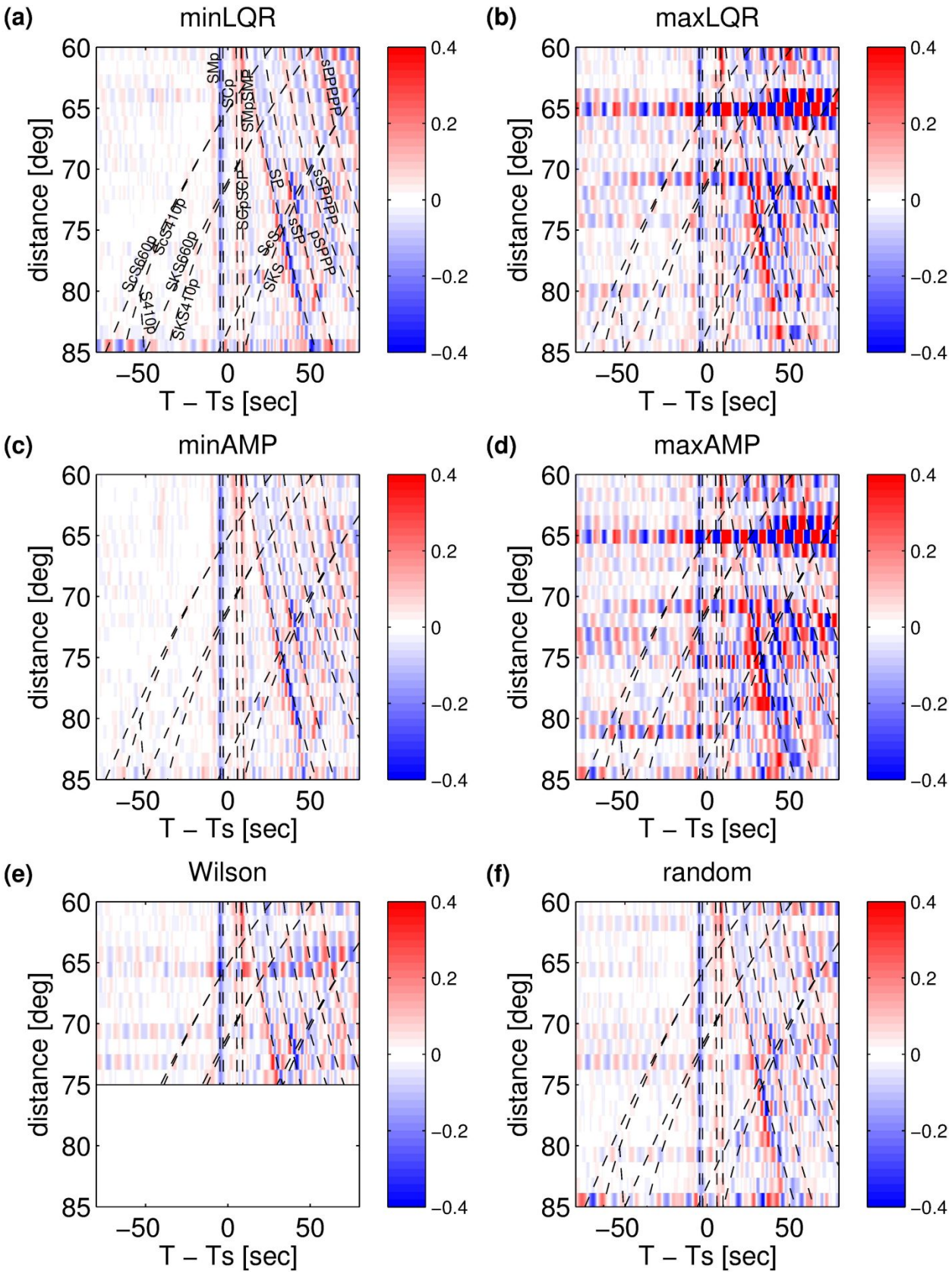
(a)
minLQR
(b)
maxLQR
(c)
minAMP
(d)
maxAMP
(e)
Wilson
(f)
random
distance [deg]
T – Ts [sec]
60
65
70
75
80
85
–50
0
50
0.4
0.2
0
–0.2
–0.4
SMp
SCp
SMpSMP
SP
sSP
pSPPP
sSPPPP
ScS
SKS
ScS660p
ScS410p
SKS660p
SKS410p
S410p

Figure S7. Images of synthetic SRFs for the case 4 from the L70 model as a function of the distance of 60°–85° with six different data selection criteria. The parent waveforms are windowed 10 s before and 35 s after the *S*-wave arrival and tapered with a 15% Hanning taper at both ends of the signal window. The frequency-domain deconvolution is done with a water level of 0.2%. See a caption of Fig. S4 for more detail.

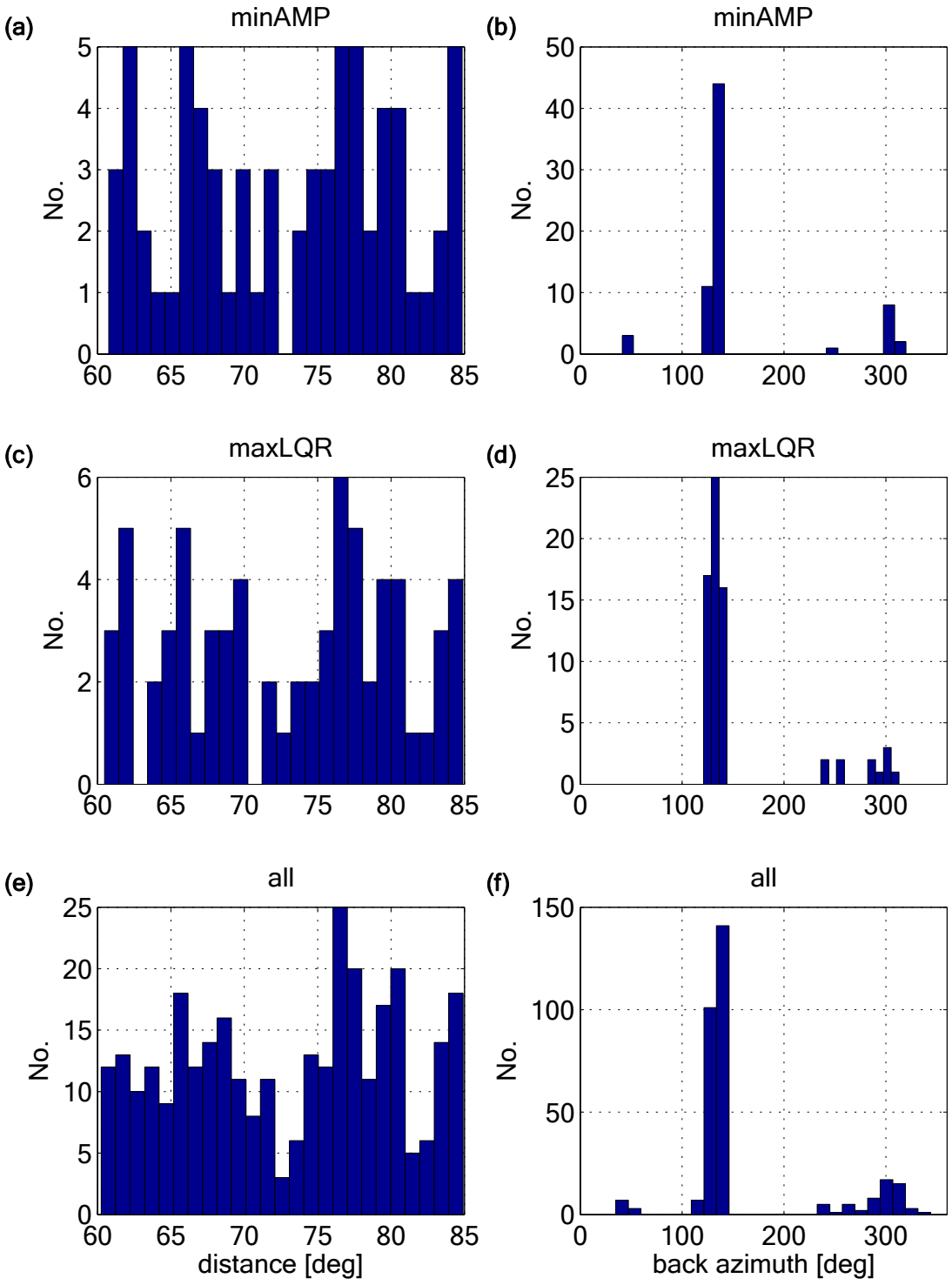

Figure S8. Histograms of epicentral distance and back azimuth against six data selection criteria. LQR and AMP data selection criteria with a percentage threshold of 25% result in negligible data selection bias in back azimuthal and epicentral distance.

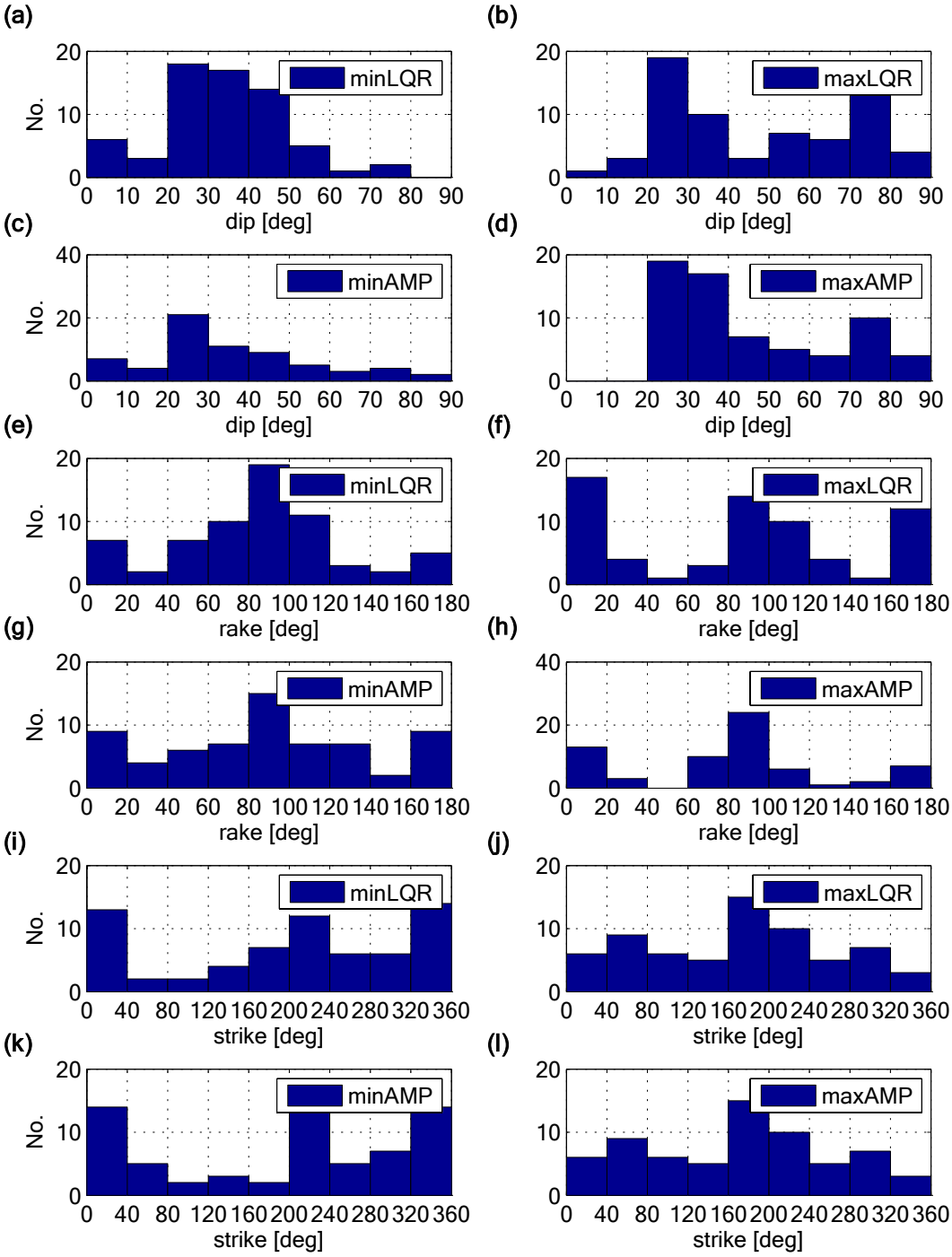

Figure S9. Histograms of earthquake source parameters (dip, strike and rake) against four data selection criteria; (a, e, i) 25% lowest LQR, (b, f, j) 25% highest LQR, (c, g, k) 25% lowest AMP, and (d, h, l) 25% highest AMP. LQR and AMP data selection criteria result in negligible data selection preference in source parameters.

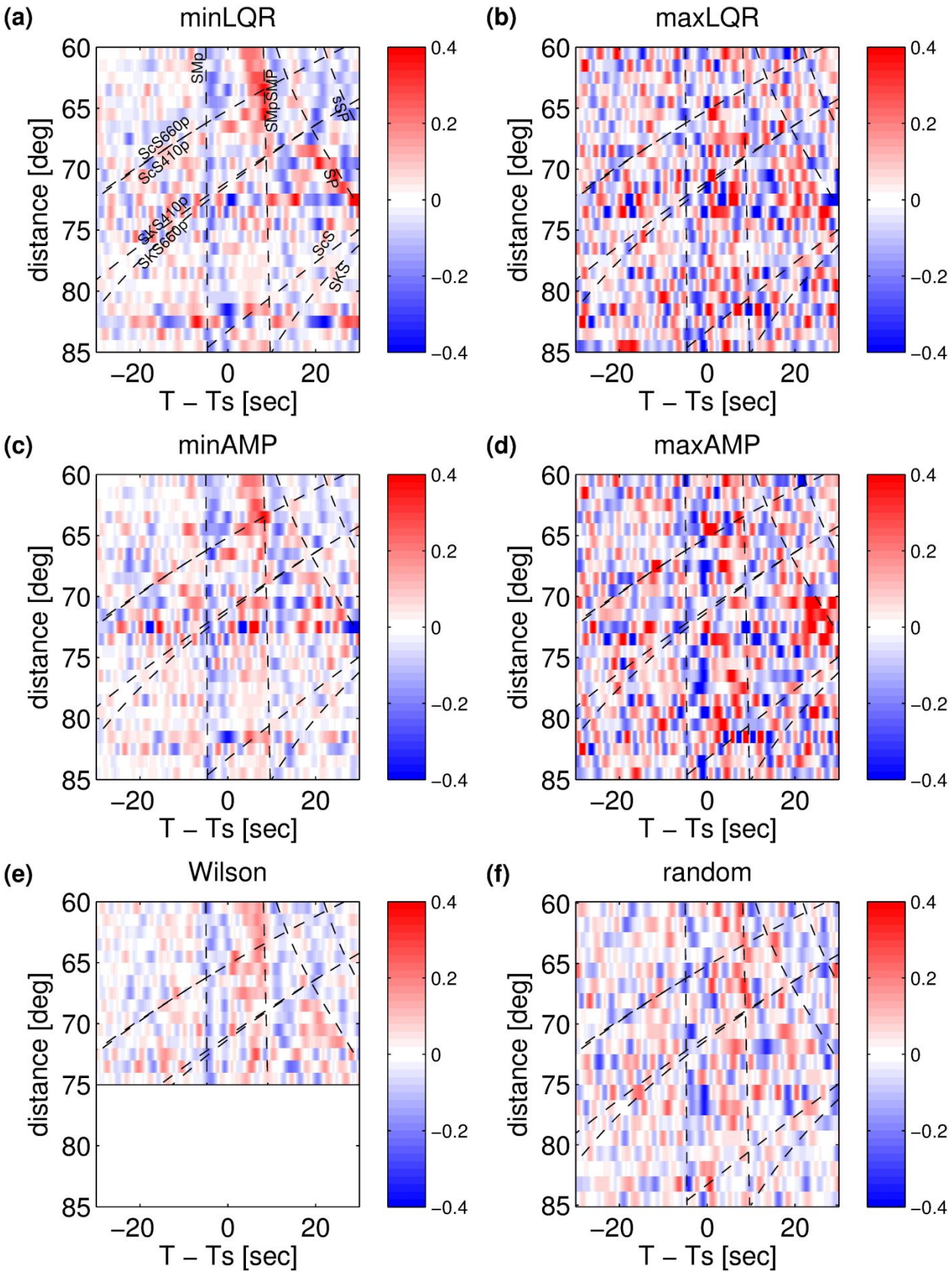
(a)
minLQR
(b)
maxLQR
(c)
minAMP
(d)
maxAMP
(e)
Wilson
(f)
random
distance [deg]
T – Ts [sec]
SMp
SMpSMP
sSP
ScS660p
ScS410p
sP
SKS410p
SKS660p
ScS
SKS
60
65
70
75
80
85
–20
0
20
0.4
0.2
0
–0.2
–0.4

96

Figure S10. Images of SRFs for station TJN as a function of the epicentral distance of 60°–85° with following six data selection criteria; (a) 25% lowest LQR, (b) 25% highest LQR, (c) 25% lowest AMP, (d) 25% highest AMP, (e) criterion by Wilson *et al*. (2006), and (f) 25% random data selection. The parent waveforms are windowed 10 s before and 35 s after the *S*-wave arrival and tapered with a 15% Hanning taper at both ends of the signal window. Time domain wiener deconvolution is done with minimum regularization of 0.01% white noise. See a caption of Fig. S4 for more detail. See also Fig. 10 for the images of -80–80 s window.

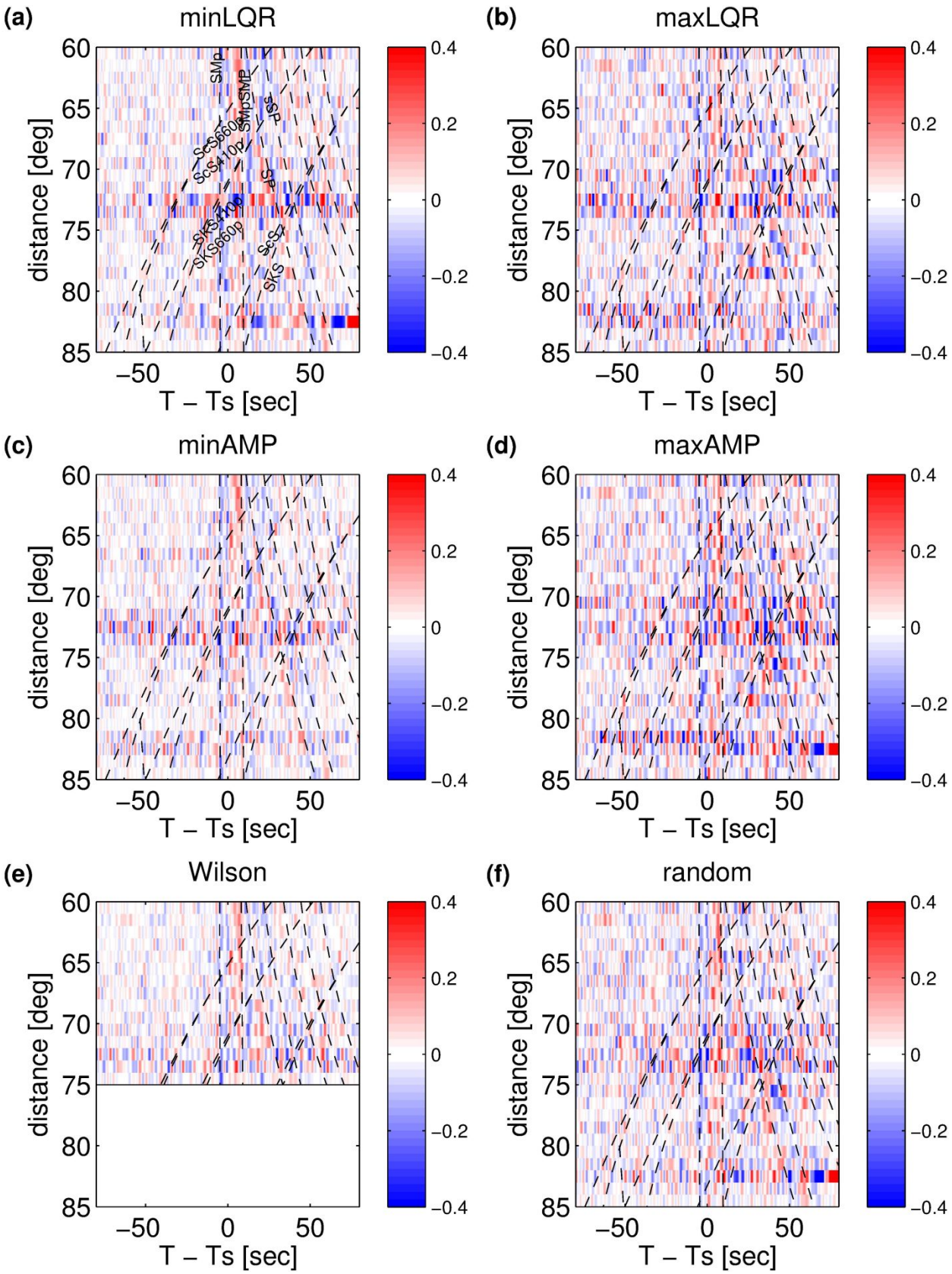
(a)
minLQR
(b)
maxLQR
(c)
minAMP
(d)
maxAMP
(e)
Wilson
(f)
random
distance [deg]
T – Ts [sec]
SMp
SMpSMP
SSP
ScS660p
ScS410p
SP
SKS410p
SKS660p
ScS
SKS
60
65
70
75
80
85
−50
0
50
0.4
0.2
0
−0.2
−0.4

104

Figure S11. Images of SRFs for station TJN as a function of the distance of 60°–85° with following six data selection criteria; (a) 50% lowest LQR, (b) 50% highest LQR, (c) 50% lowest AMP, (d) 50% highest AMP, (e) criterion by Wilson *et al*. (2006), and (f) 50% random data selection. The parent waveforms are windowed 10 s before and 35 s after the *S*-wave arrival and tapered with a 15% Hanning taper at both ends of the signal window. Time domain wiener deconvolution is done with minimum regularization of 0.01% white noise. See a caption of Fig. S4 for more detail. See Fig. S12 for the images plotted for -30–30 s window.

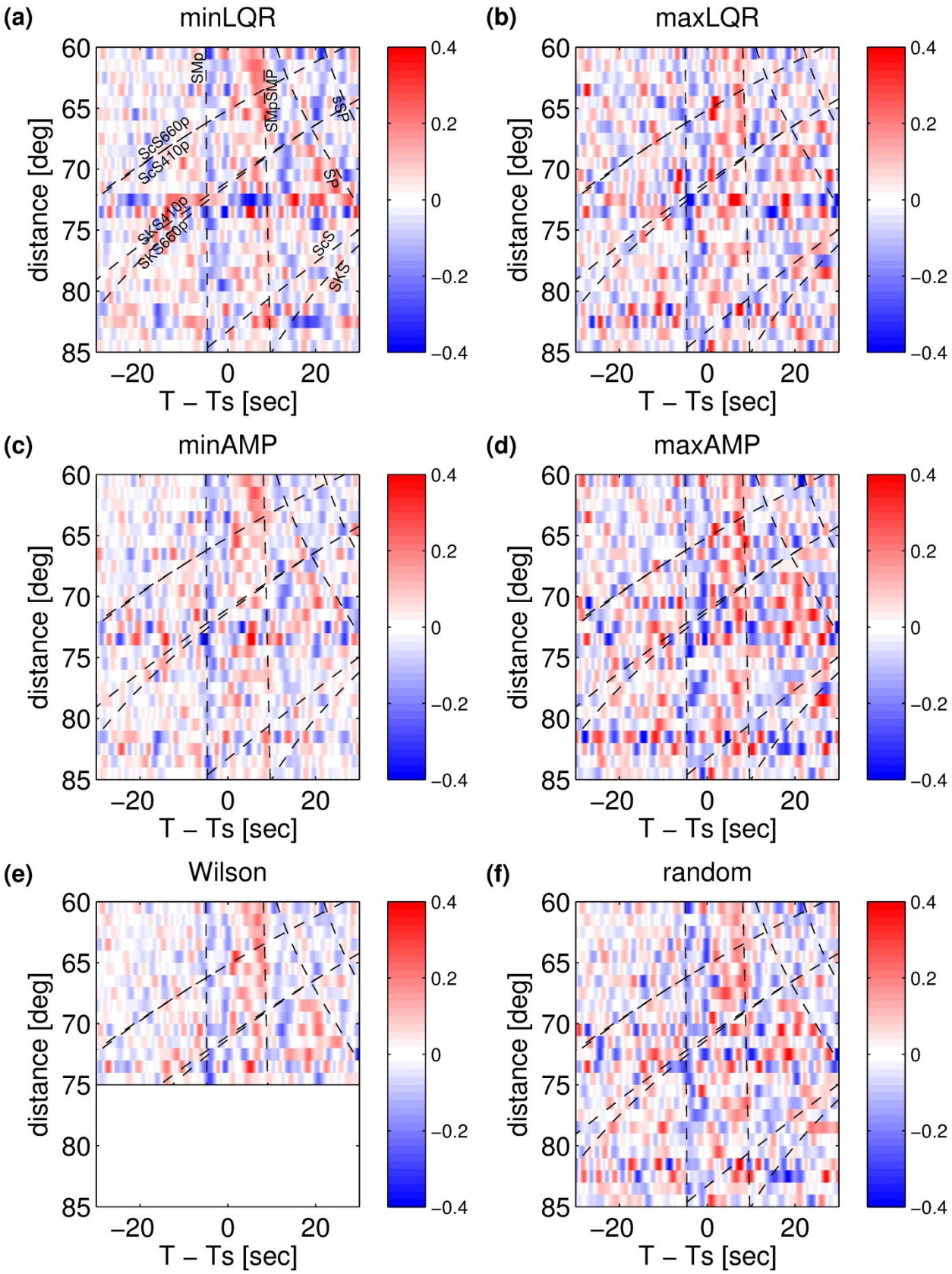
(a)
minLQR
(b)
maxLQR
(c)
minAMP
(d)
maxAMP
(e)
Wilson
(f)
random
distance [deg]
T – Ts [sec]
SMp
SMpSMP
sSP
ScS660p
ScS410p
SP
SKS410p
SKS660p
ScS
SKS
60
65
70
75
80
85
–20
0
20
0.4
0.2
0
–0.2
–0.4

112

Figure S12. Images of SRFs for station TJN as a function of the distance of 60°–85° with following six data selection criteria; (a) 50% lowest LQR, (b) 50% highest LQR, (c) 50% lowest AMP, (d) 50% highest AMP, (e) criterion by Wilson *et al*. (2006), and (f) 50% random data selection. The parent waveforms are windowed 10 s before and 35 s after the *S*-wave arrival and tapered with a 15% Hanning taper at both ends of the signal window. Time domain wiener deconvolution is done with minimum regularization of 0.01% white noise. See a caption of Fig. S4 for more detail.

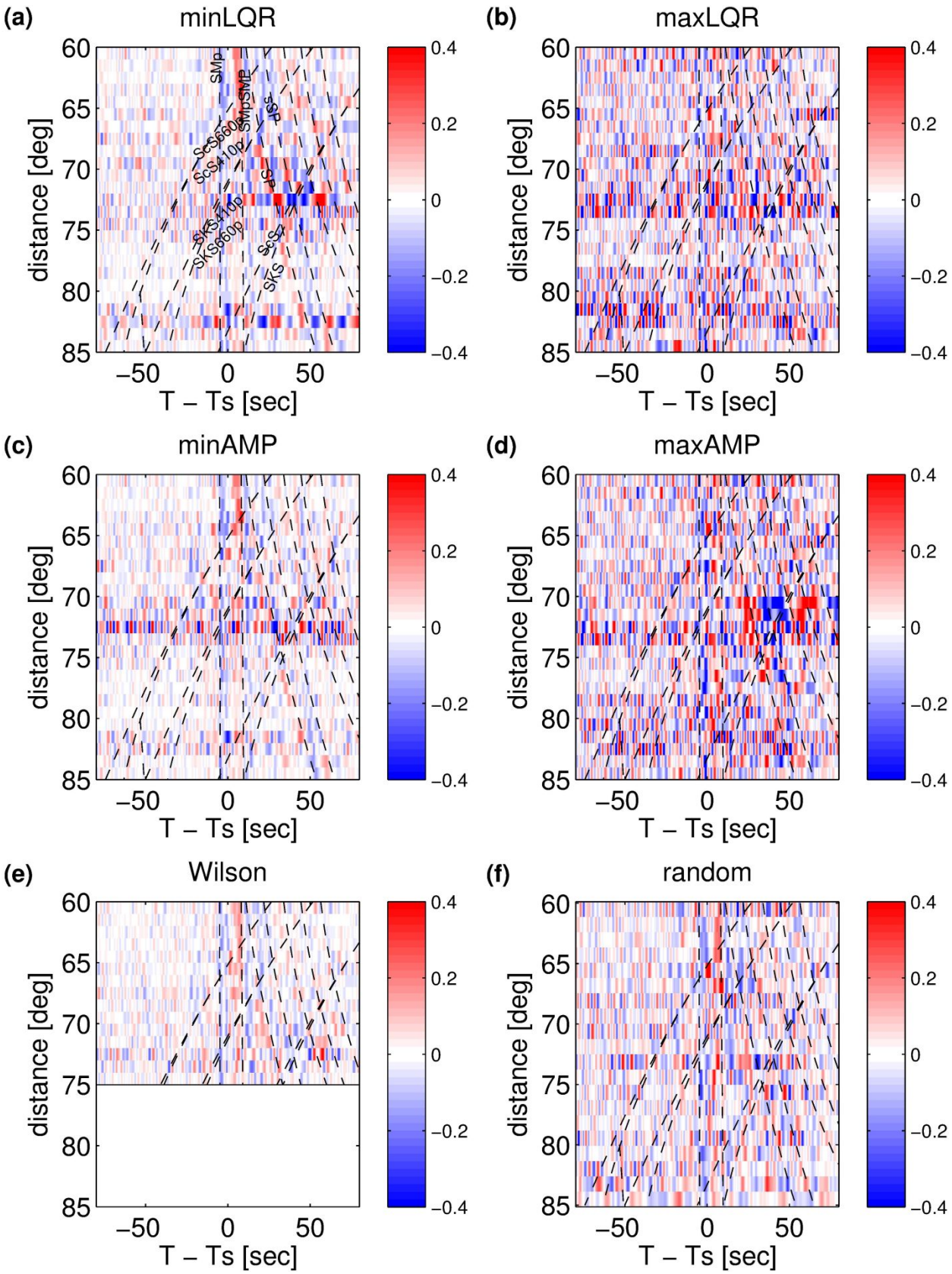
(a)
minLQR
(b)
maxLQR
(c)
minAMP
(d)
maxAMP
(e)
Wilson
(f)
random
distance [deg]
T – Ts [sec]
SMp
SMpSMP
SSP
ScS
ScS660p
ScS410p
SKS410p
SKS660p
SKS
0.4
0.2
0
−0.2
−0.4

Figure S13. Images of SRFs for station TJN as a function of the distance of 60°–85° with following six data selection criteria; (a) 25% lowest LQR, (b) 25% highest LQR, (c) 25% lowest AMP, (d) 25% highest AMP, (e) criterion by Wilson *et al*. (2006), and (f) 25% random data selection. The parent waveforms are windowed 10 s before and 35 s after the *S*-wave arrival and tapered with a 15% Hanning taper at both ends of the signal window. Time domain wiener deconvolution is done with a strong regularization of 1% white noise. See Fig. S14 for the images plotted for -30–30 s window.

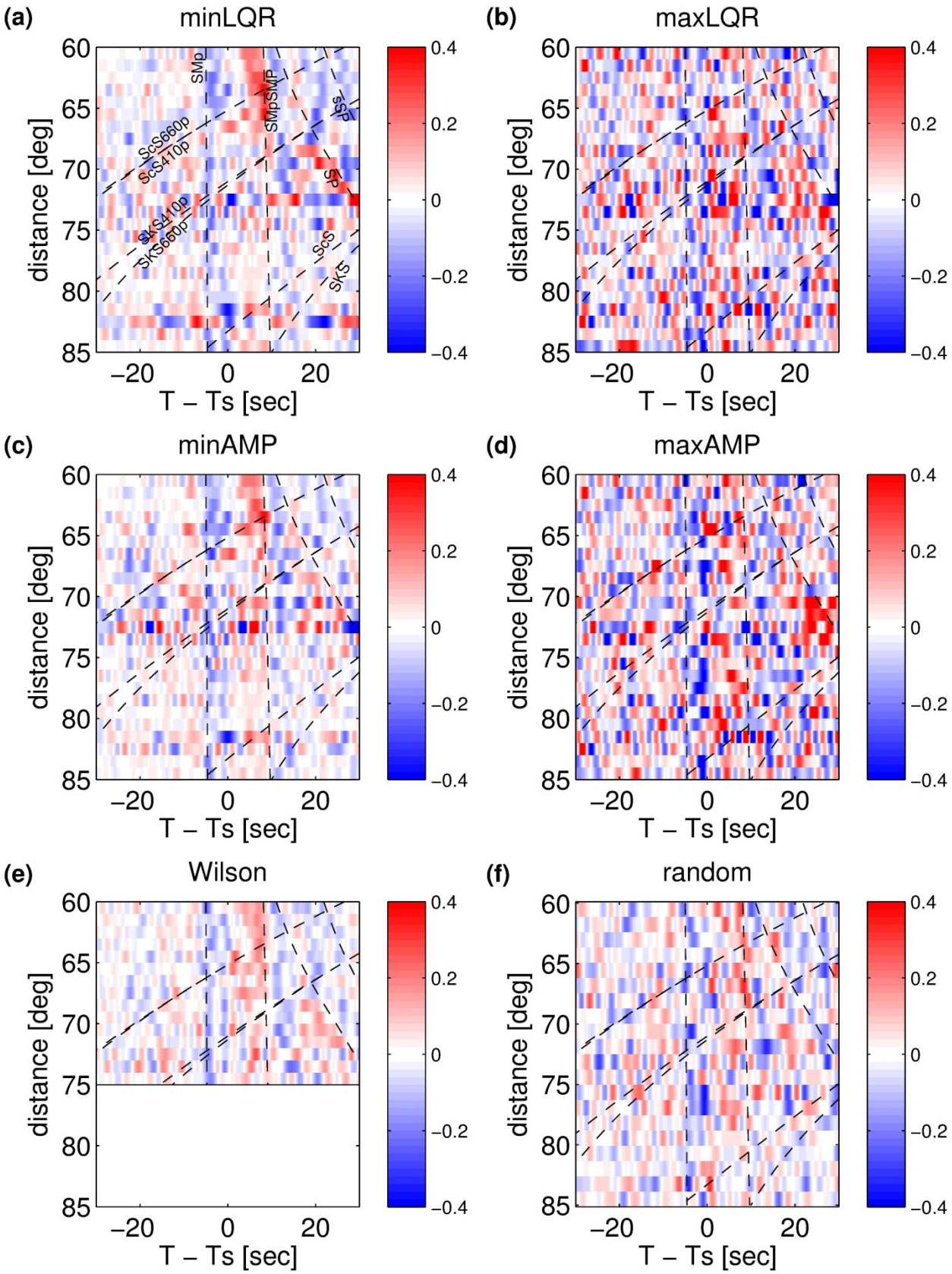
(a)
minLQR
(b)
maxLQR
(c)
minAMP
(d)
maxAMP
(e)
Wilson
(f)
random
distance [deg]
T – Ts [sec]
SMp
SMpSMP
sSP
ScS660p
ScS410p
sP
SKS410p
SKS660p
ScS
SKS
60
65
70
75
80
85
–20
0
20
0.4
0.2
0
–0.2
–0.4

128

Figure S14. Images of SRFs for station TJN as a function of the distance of 60°–85° with following six data selection criteria; (a) 25% lowest LQR, (b) 25% highest LQR, (c) 25% lowest AMP, (d) 25% highest AMP, (e) criterion by Wilson *et al*. (2006), and (f) 25% random data selection. The parent waveforms are windowed 10 s before and 35 s after the *S*-wave arrival and tapered with a 15% Hanning taper at both ends of the signal window. Time domain wiener deconvolution is done with a strong regularization of 1% white noise.

Reference

Kennett, B. & Engdahl, E., 1991. Traveltimes for global earthquake location and phase identification, *Geophysical Journal International*, ***105***(2), 429–465, https://doi.org/10.1111/j.1365-246X.1991.tb06724.x.